

2020

ICG- AND GNP-PHLIP: NOVEL AGENTS FOR IMAGING AND THERAPY

Troy M. Crawford
University of Rhode Island, troy_crawford@uri.edu

Follow this and additional works at: https://digitalcommons.uri.edu/oa_diss

Terms of Use

All rights reserved under copyright.

Recommended Citation

Crawford, Troy M., "ICG- AND GNP-PHLIP: NOVEL AGENTS FOR IMAGING AND THERAPY" (2020). *Open Access Dissertations*. Paper 1150.
https://digitalcommons.uri.edu/oa_diss/1150

This Dissertation is brought to you by the University of Rhode Island. It has been accepted for inclusion in Open Access Dissertations by an authorized administrator of DigitalCommons@URI. For more information, please contact digitalcommons-group@uri.edu. For permission to reuse copyrighted content, contact the author directly.

ICG- AND GNP-PHLIP: NOVEL AGENTS FOR IMAGING AND THERAPY

BY

TROY M. CRAWFORD

A DISSERTATION SUBMITTED IN PARTIAL FULFILLMENT OF THE

REQUIREMENTS FOR THE DEGREE OF

DOCTOR OF PHILOSOPHY

IN

PHYSICS

UNIVERSITY OF RHODE ISLAND

2020

DOCTOR OF PHILOSOPHY DISSERTATION

OF

TROY M. CRAWFORD

APPROVED:

Dissertation Committee:

Major Professor

Yana K. Reshetnyak

Michael Antosh

Geoffrey Bothun

Ying Sun

UNIVERSITY OF RHODE ISLAND

2020

ABSTRACT

After heart disease, cancer is the leading cause of death in the U.S. According to the National Cancer Institute, approximately 38% of the population will be diagnosed with cancer at some point over the course of their life. This number is only expected to increase with the increased age of the general public due to medical progress, leading to an increased importance in finding effective and convenient treatment that can be used across a wide array of cancers.

In theory, any tumor can be destroyed using enough of a cytotoxic method, whether it be heating, radiation, surgery, or chemotherapy. However, because cancer cells are derived from a person's own healthy cells mutating, all of these treatments involve destroying healthy tissue in the process. Because of this, the most important aspect of any treatment modality is its tumor specificity: the ability of the treatment to target cancerous tissue vs. healthy tissue. The higher the ratio of cancer cell death to healthy cell death a treatment contains, the more effectively it can be used in clinical practice.

A common method of targeting cancerous tissues is by targeting biomarkers that are overexpressed in cancer cells. These can include utilizing antibody, receptor, or vitamin bindings. While these methods can increase the specificity of treatment, there are also associated shortcomings with them. They tend to be cell-line specific, so a treatment that may work for one strain of cancer may not have the desired effect across other lines. Even within a single cancer strain, there exists heterogeneity a tumor, resulting in some cells not expressing the biomarkers to the extent needed for adequate targeting. This not only results

in some cells surviving damage, but those cells then go on to reproduce, passing on their traits, and causing the tumor to adapt to become more resistant to that treatment. Within this arises the need to target a more general biomarker presented throughout all cancer cells and strains.

In 1931, the Nobel Prize in Physiology was awarded to Dr. Otto Heinrich Warburg for his discovery of what is known as the Warburg effect. In his research, Dr. Warburg discovered that even in the presence of oxygen, cancerous tissue produces the majority of its energy via anaerobic glycolysis instead of the aerobic oxidative phosphorylation. Glycolysis is a much less efficient, but faster, process, resulting in an excess of positively charged hydrogen ion byproducts. These are pumped outside of the cell membrane to maintain a normal pH within the cell, which results in a low pH environment immediately extracellularly to cancerous tissue. This acidity at the surface of cancer cells is ubiquitous across solid tumors, making it an ideal biomarker to target for cancer treatment.

pH-Low Insertion Peptide (pHLIP) is a pH-dependent peptide, whose pH-dependent action is based on the protonation of the aspartic (Asp) and glutamic (Glu) acid residues at the C-terminal end of the peptide. In the presence of a low pH environment, the normally negatively charged Asp and Glu residues of pHLIP become protonated, increasing the overall hydrophobicity of the polypeptide. In the presence of a lipid bilayer, it triggers the insertion of the peptide across the bilayer to form a transmembrane alpha helix. Because of the Warburg effect described above, the acidity surrounding a cancerous tissue therefore promotes selective insertion of pHLIP across the cell membrane of tumor cells. As a result,

different cargoes can be attached to the peptide, consequently being either tethered or translocated across membrane of cells in acidic diseased tissue at much higher proportions than in healthy tissue.

The main goal of this work was to evaluate the efficacy of different pHLIP variants to target tumors and deliver cargo across the membrane for therapeutic and diagnostic/imaging applications. In therapeutic applications, the attached cargo would directly induce cell death via external radiation enhancement, cell heating, or radioactive emission. For this, gold nanoparticles (GNPs) were studied, as gold is an inert and biocompatible. The focus of this work was to create GNPs coated with pHLIP to allow for enhancement of radiation via Auger electron emission, and to explore the possibility of creating gold-coated bicelles for heating via plasmon resonance. For diagnostic and imaging applications, the attached cargo would be used to visually differentiate the cancerous and healthy tissue, and be used in coordination with therapeutic strategies such as surgery for treatment. For this, the near-infrared dye indocyanine green (ICG) was conjugated to pHLIP to make ICG-pHLIP. ICG is already used in clinics for fluorescence guided surgery for imaging of lymph nodes and blood flow, making ICG-pHLIPs transition to clinics more straightforward and efficient. The focus of this study was to find the ICG-pHLIPs selectivity to cancerous tissue in vivo in balb-c and nude mice, exploring proof of concept for its continuation into human trials.

ACKNOWLEDGMENTS

I'd like to begin by expressing my utterly deepest gratitude to Dr. Yana Reshetnyak, who has helped me through countless mental breakdowns, rushed timelines, and some moments of crippling self-doubt. I applied to URI in engineering, and before I even began my college career, Yana had convinced me to join the physics department. The care and dedication she puts into her work and students was obvious even before I was lucky enough to have her advising me. She is responsible for both my decision to begin the doctorate path, and singlehandedly talked me into continuing it during some of my more stressful periods. I could not have gotten to this point without her, and I'll never be able to convey the amount of appreciation I have for everything she has done for me.

Secondly, I would be remiss if I spoke any less fondly of Dr. Anna Moshnikova. Without Anna, I truly believe my flaws would have come to light much quicker, and I don't think my finishing would be possible without her. She has helped me through too many experiments to count, but to limit myself to talking about her direct help in the lab would be to do her a disservice. She has gone from being the mentor I'm terrified of disappointing, to a trusted colleague I can go to whenever I had questions, to a close friend I can come to whenever I have a problem of any kind, and somehow she'd always have the answer. During our countless hours working side by side, she has taught me how to become the best scientist I can be, and while I still have a lot to learn, at least I've learned some Russian to show for it (Mysh' spit. I can (could?) also count to 10. After reconsidering, my Russian is not very good). Spasibo, Anna.

In this physics department, I'd like to thank Dr. Leonard Kahn and Dr. Oleg Andreev specifically. Dr. Kahn has been someone who has guided me for nine years whenever I was uncertain about how to continue, and has always had my best interests at heart. It is rare to find someone as a freshman who not only pushes and believes in you, but that you can always share a laugh with on the side. Dr. Kahn has been all of that for me, and I will forever appreciate his understanding at my inability to navigate the red tape of grad school. Dr. Andreev has been a constant pressure to strive in my lab. Always pushing to get the best out of his students, his challenging and straightforward nature has always demanded the acquisition of more knowledge and understanding, as has stimulated me to be the inquisitive and confident person I've become.

Within my lab, there are two people I'd like to single out. Dr. Jenn Daniels, my mentor for my first two years of my grad school career, who helped me discover my general love of the lab work and research. I could not have asked for a better person to show me the ropes, and I swear, she did everything she could to teach me about the importance of organization and timeliness, my ineptitude in those areas are my own failure. It then flows into the next person, soon-to-be-Dr. Chip Slaybaugh, who has helped cover me through when that failure flared up. Every time I have forgotten to do something, left a machine on, or just had a problem too silly to explain to Anna, he has been there to help. It's been great having someone to go through everything together with, and he's been an irreplaceable presence in the lab.

Beyond them, everyone in the lab has helped me through such an unbelievable amount of things. Anuradha, who has been a constant and helpful presence; Sean, who was incredibly fantastic to work with, teach, and learn from (and showed me how weird it is mentoring

someone 3 inches taller than me); Ramona, who taught me the delicacies of mice work; Mike, who has been great at dealing with my inadequacies in teaching; Hannah, who's always happy to have a scientific conversation where she shows me how little I really know; Linden, for showing me the professionalism we can express while still enjoying life beyond work; and Da, who showed me just how much I have to learn at guitar. Everyone in this list has been integral to my success at multiple points in my career.

I'd like to thank my committee, Drs. Michael Anotsh, Geofferey Bothun, and Ying Sun. Quick and efficient communication has never been my strong suit, and they have worked with me through this entire process, and somehow despite all my shortcomings, I'm (planning on) graduating on time. I can only thank them earnestly for helping me schedule (with what must have seemed like supreme naïve incompetence) the impossible hour when four college professors are all free at the same time.

Lastly, I'd like to thank my friends and family. Sean, Rob, and Wes, who have brought me through so many points in my life, and dealt with me every time I should have been intolerable. Elliott, Gus, and Ben, for distracting me with poker, football, and all things ridiculous. My parents, who have become more akin to incredibly close friends who just happen to have unwavering support of me despite all my failings. Gina and Tim, who have unintentionally worked together to teach me everything that's important in life. Every single one of my friends who I couldn't name because I honestly just don't have enough room, I couldn't have done this without all of you.

Long, but unquestionably necessary. Thank you all.

PREFACE

This dissertation is written in “Manuscript” format, using the Thesis/Dissertation template of the University of Rhode Island. There are three manuscripts included in this dissertation, each of which comprises a chapter. The tables and figures of each manuscript are listed under the corresponding chapter in the list of tables and figures.

The results of our studies presented in the first two chapters were published in the following papers:

1. Wyatt L, Moshnikova A, **Crawford TM**, Engelman DM, Andreev OA, Reshetnyak YK. New pHLIPs for the Targeted Intracellular Delivery of Cargo Molecules to Tumors. *PNAS* (2018)
2. Daniels JL, **Crawford TM**, Andreev OA, and Reshetnyak YK. Synthesis and Characterization of pHLIP® Coated Gold Nanoparticles. *Biochem Biophys Rep* (2017)

The final chapter is composed of research that has been submitted for publication:

3. **Crawford TM**, Moshnikova A, Roles S, Weerakkody D, DuPont M, Carter LM, Shen J, Engelman D, Lewis JS, Andreev OA, Rehestnyak YK. ICG pHLIP: A Novel Agent for Fluorescence-Guided Surgery. *Manuscript submitted for publication.*

TABLE OF CONTENTS

ABSTRACT	ii
ACKNOWLEDGMENTS	v
PREFACE	viii
TABLE OF CONTENTS.....	ix
LIST OF TABLES	x
LIST OF FIGURES.....	xi
CHAPTER 1	1
New pHLIPs for the Targeted Intracellular Delivery of Cargo Molecules to Tumors.....	1
CHAPTER 2	36
Synthesis and Characterization of pHLIP Coated Gold Nanoparticles.....	36
CHAPTER 3	72
ICG pHLIP: A Novel Agent for Fluorescence Guided Surgery.....	72

LIST OF TABLES

CHAPTER 1

Table 1. List of peptide sequences.....	30
Table 2. Biophysical and cytotoxicity parameters of pHLIP variants.....	31

CHAPTER 2

There are no tables in Chapter 2

CHAPTER 3

Table S1. Qualification of GLP ICG-pHLIP batch #1912127.....	139
Table S2. Bound and unbound fractions of ICG-pHLIP.....	141
Table S3. Concentration of ICG-pHLIP in blood of mice and dogs.....	142
Table S4. Fluorescence intensity in <i>ex vivo</i> imaging of organs.....	143
Table S5. Mean fluorescence intensity of <i>ex vivo</i> imaging.....	147

LIST OF FIGURES

CHAPTER 1

Figure 1. Chemical structures and results of biophysical experiments with pHLIP bundles.....	32
Figure 2. Ellipticity ratios of CD signals for all pHLIP variants and therapeutic indices of pHLIP amanitin constructs	33
Figure 3. pH-dependent potency observed in <i>in vitro</i> experiments.....	34
Figure 4. Tumor fluorescence intensity and tumor-to-tissue intensity ratios from <i>in vivo</i> experiments.....	35

CHAPTER 2

Figure 1. Characterization of spherical gold nanoparticles.....	68
Figure 2. Structure of bicelles	69
Figure 3. Characterization of multispiked gold nanoparticles	70
Figure 4. Tumor imaging of spherical gold nanoparticle uptake	71

CHAPTER 3

Figure 1. Characterization of ICG-pHLIP and blood clearance in mice and dogs	96
Figure 2. Imaging of blood vessels in mice.....	97
Figure 3. Imaging of blood vessels in pigs.....	98
Figure 4. Biodistribution and Kinetics.....	99
Figure 5. Tumor targeting.....	100
Figure 6. <i>Ex vivo</i> imaging of tumors with surrounding muscle	101

Figure 7. <i>Ex vivo</i> imaging and imaging of section.....	102
Figure 8. Surgical removal of tumors under fluorescence guidance	103
Figure S1. HPLC and MS of ICG-pHLIP.....	148
Figure S2. ICG-pHLIP and Isosulfan Blue	149
Figure S3. Inhibition response curves.....	150
Figure S4. Fluorescence angiography in mice.....	151
Figure S5. Imaging of blood vessels in pigs.....	152
Figure S6. ICG-pHLIP fluorescence in mice	153
Figure S7. Tissue/Organ mean fluorescence values.....	154
Figure S8. ICG-pHLIP fluorescence in human and murine tumors in mice	155
Figure S9. Comparison of H&E and ICG signal	156

CHAPTER 1

Published in PNAS in March, 2018

New pHLIPs for the Targeted Intracellular Delivery of Cargo Molecules to Tumors

Linden C. Wyatt^a, Anna Moshnikova^a, Troy Crawford^a,
Donald M. Engelman^{b,1}, Oleg A. Andreev^{a,1}, Yana K. Reshetnyak^{a,1}

^a Physics Department, University of Rhode Island, Kingston, RI 02881;

^b Department of Molecular Biophysics and Biochemistry, Yale, New Haven, CT 06511

¹To whom correspondence may be addressed. Emails: reshetnyak@uri.edu or
andreev@uri.edu or donald.engelman@yale.edu

Keywords: membrane-associated folding, tumor acidity, cytoplasmic drug delivery, polar
drugs, targeted chemotherapy

Conflict of Interest Statement: D.M.E., O.A.A., and Y.K.R. are founders of pHLIP, Inc. They have shares in the company, but the company did not fund any part of the work reported in the paper, which was done in their academic laboratories.

Abstract

The pH (low) insertion peptides (pHLIPs) target acidity at the surfaces of cancer cells and show utility in a wide range of applications, including tumor imaging and intracellular delivery of therapeutic agents. Here we report pHLIP constructs that significantly improve the targeted delivery of agents into tumor cells. The investigated constructs include pHLIP bundles (conjugates consisting of two or four pHLIP peptides linked by polyethylene glycol) and Var3 pHLIPs containing either the nonstandard amino acid, γ -carboxyglutamic acid, or a glycine–leucine–leucine motif. The performance of the constructs in vitro and in vivo was compared with previous pHLIP variants. A wide range of experiments was performed on nine constructs including (i) biophysical measurements using steady-state and kinetic fluorescence, circular dichroism, and oriented circular dichroism to study the pH-dependent insertion of pHLIP variants across the membrane lipid bilayer; (ii) cell viability assays to gauge the pH-dependent potency of peptide-toxin constructs by assessing the intracellular delivery of the polar, cell-impermeable cargo molecule amanitin at physiological and low pH (pH 7.4 and 6.0, respectively); and (iii) tumor targeting and biodistribution measurements using fluorophore-peptide conjugates in a breast cancer mouse model. The main principles of the design of pHLIP variants for a range of medical applications are discussed.

Introduction

The targeted delivery of drugs to cancer cells promises to maximize their therapeutic effects while reducing side effects. Although many biomarkers exist that can be exploited to improve tumor targeting and treatment outcomes, such as various receptors overexpressed at the surfaces of some cancer cells, useful markers are not present in all tumors. Further, the heterogeneity of the cancer cell population in an individual tumor and between tumors of various patients limits the effective use of biomarker targeting technologies, and rapid mutation increases the likelihood of the selection of cancer cell phenotypes that do not express high levels of the targeted biomarker. Thus, biomarker targeting can act as a selection method that may lead to the development of drug resistance and poor patient outcomes (1–3).

It is well known that acidosis is ubiquitous in tumors, including both primary tumors and metastases, as a consequence of their rapid metabolism (4). The acidic microenvironment is generated by the increased use of glycolysis by cancer cells, and by the abundance of carbonic anhydrase proteins on the cancer cell surfaces. Tumor cells stabilize their cytoplasmic pH by exporting the acidity to the extracellular environment. As a result of the flux and the membrane potential, the extracellular pH is lowest at the surfaces of cancer cells, where it is significantly lower than normal physiological pH and the bulk extracellular pH in tumors (5–7). The low pH region persists at the cancer cell surface even in well-perfused tumor areas. The acidity on the surfaces of cancer cells is a targetable characteristic that is not subject to clonal selection, and the level of acidity is a predictor of tumor invasion and aggression, since more rapidly growing tumor cells are more acidic.

The emerging technology based on pH (low) insertion peptides (pHLIPs) comprises a variety of acidity-targeting peptides, each possessing different tumor-targeting characteristics. The pHLIPs can be used in a wide variety of applications, so it is desirable

to have a range of options for specific applications. Some examples of these applications include (i) fluorescence imaging (8–10) and fluorescence image-guided surgery (11); (ii) nuclear imaging including PET and SPECT (single-photon emission computed tomography) (12, 13); (iii) therapeutic applications such as the targeted delivery of polar toxins that cannot cross cell membranes (14, 15), drug-like molecules that inherently diffuse across cell membranes (16, 17), and gene therapy (18); and (iv) nanotechnology for enhancing the delivery of gold nanoparticles (19, 20) or liposome-encapsulated payloads to cancer cells (21).

The pHLIPs are triggered to insert across the membranes of cancer cells by the acidity at the cancer cell surface. The behavior of peptides in the pHLIP family is typically described in terms of three states: at physiological pH (pH 7.4), peptides exist in equilibrium between a solvated state (state I) and a membrane-adsorbed state (state II); a decrease in pH shifts the equilibrium toward a membrane-inserted state (state III) (22). The mechanism

Results

pHLIP constructs. We investigated nine pHLIP variants; among them are Var3/Gla (with nonstandard amino acid Gla), Var3/GLL (with glycine–leucine–leucine motif), and pHLIP bundles (Table 1). The pHLIP bundles consist of two- or four-armed polyethylene glycol (PEG) 2-kDa spacers conjugated to the cysteine residue at the N terminus of WT: PEG-2WT and PEG-4WT, respectively (Fig. 1 A and B). Our motivation is to increase both the membrane affinity and the cooperativity of the transition from the membrane-surface state to the membrane-inserted state. Enhancement of affinity is expected to improve targeting, and higher cooperativity should narrow the window of pH that produces TM drug delivery. The information about all pHLIP variants used in the study with additional variations from the addition of single N- or C-terminal cysteine or lysine residues for conjugation purposes is provided in Tables S1 and S2. Nine pHLIP variants can be grouped together in various

ways by shared characteristics. A WT-like group contains peptides with two protonatable residues (shown in bold in Table 1) in the putative TM region, multiple protonatable residues in the membrane-inserting C-terminal region, and two tryptophan residues (residue W) both located at the beginning of the helix-forming TM region; this group includes WT, PEG-2WT and PEG-4WT, WT/Gla, and WT/Gla/Aad. A Var3-like group is based on Var3 from the first pHLIP series (25). This group includes Var3, Var3/Gla, and Var3/GLL, each of which have three protonatable residues in the TM region and tryptophan residues located at the beginning and end of the TM region. Considering this scheme, ATRAM, with its multiple glycine and leucine residues and single tryptophan located about two-thirds to the end of its TM part, is in a group of its own. Other subgroups can be considered as well: a subgroup of peptides that incorporate the nonstandard Gla residue, shown in italics in Table 1 (i.e., WT/Gla, WT/Gla/Aad, and Var3/Gla), and another subgroup that includes peptides containing the GLL motif (Var3/GLL and ATRAM). When performing analysis of biophysical measurements, analyzing variants with respect to their group mates becomes important: The very different characteristics of peptides from various groups make it difficult to accurately compare the behavior of all peptides at the same time.

Biophysical steady-state and kinetics studies. A variety of spectroscopic techniques were employed to probe the interaction between pHLIP variants and 1-palmitoyl-2-oleoyl-sn-glycero-3-phosphocholine (POPC) phospholipid bilayers in liposomes; these techniques included steady-state fluorescence spectroscopy, circular dichroism (CD), oriented circular dichroism (OCD), and stopped-flow fluorescence measurements. Steady-state fluorescence and CD experiments were conducted in phosphate buffer titrated with hydrochloric acid to drop the pH from pH 8 to pH 4 to ensure consistency with previously

published data (25, 29, 30). Steady-state and kinetics fluorescence experiments measuring the pH-dependent transition from state II to state III were carried out in phosphate buffer containing the physiological concentrations of free calcium (1.25 mM) and magnesium (0.65 mM) ions found in blood, since we expected that some of the constructs might bind these ions.

We established that, in solution, PEG-2WT and PEG-4WT most probably exist in compact coil conformations, where tryptophan and other aromatic residues can form stacking structures. The resulting exciton formation was seen as a minimum around 230 nm in the CD spectra of these pHLIP bundles (Fig. 1 E and F). At pH 8, changes in the tryptophan fluorescence show that both constructs interact with the lipid bilayer, and it appears that PEG-4WT exhibits stronger binding than PEG-2WT in state II. With a reduction of pH, both pHLIP bundles inserted into the bilayer to form helices, and the TM orientations of these helices were confirmed by OCD measurements (Fig. 1 G and H). It is important to note that, in state III, the membrane-inserted state, the exciton signal generated by π - π stacking is no longer present, suggesting that the insertion of each pHLIP renders it independent of the other(s). The pK of the transition from state II to state III was shifted to pH 6.6, and, as might be expected, the cooperativity of the transition was increased for PEG-4WT compared with PEG-2WT (Fig. 1 I and J).

We compared the groups consisting of WT, Var3, and ATRAM pHLIP variants to the newly designed Var3/Gla and Var3/GLL pHLIP variants. The HPLC retention times of the peptides indicate increasing hydrophobicity within the groups in the following order, from less to more hydrophobic: WT, WT/Gla, WT/Gla/Aad and Var3, Var/Gla, Var3/GLL, and ATRAM, with ATRAM being the most hydrophobic (Table S2). Both new pHLIP variants, Var3/Gla and Var3/GLL, demonstrated a pH-dependent interaction with the membrane (Fig. S1). Var3/GLL showed a higher percentage of membrane-inserted population at pH

8, which reflects a higher affinity of the peptide for the lipid bilayer both at physiological and high pH due to the increased hydrophobicity of the peptide.

As seen for previous pHLIP designs, a blue shift (or decrease in Stokes shift) resulting from the environmental changes from state I to state II and state III was observed for all peptides (Table S3), indicating partitioning of the peptides into the lipid bilayer. However, we cannot directly compare the positions of fluorescence spectra maxima for peptides belonging to the different groups, since the locations of the tryptophan residues within the peptides varies greatly. With this fact in mind, we can conclude that the peptides had very different conformations in state II at pH 8, and that the highest membrane affinity was exhibited by the PEG-pHLIPs and by the WT/Gla/Aad, Var3/GLL, and ATRAM peptides. The PEG-pHLIPs have multiple binding sites due to the linking of multiple WT peptides within a single construct, which is expected to enhance binding affinity. The WT/Gla/Aad, Var3/GLL, and ATRAM have the most hydrophobic sequences, and thus exhibit strong binding/insertion. We also found that some peptides were especially sensitive to the presence of calcium and magnesium ions, namely WT, variants containing the Gla residue (WT/Gla, WT/Gla/Aad, and Var3/Gla), and ATRAM. This sensitivity was most obviously seen as a decreased Stokes shift (usually 2 nm to 3 nm) in state I and/or state II, and might reflect slight increases in the hydrophobicity of the peptides caused by the coordination of divalent cations resulting from the presence of closely spaced protonatable residues, such as those found in the C-terminal region of WT and, to some degree, in ATRAM, or to the presence of the Gla residue, with its two protonatable carboxyl groups, in the WT/Gla, WT/Gla/Aad, and Var3/Gla peptides. It is known that a Gla residue can form a complex with a calcium ion (31–33). The decrease in Stokes shift in state II is likely due to the location of membrane-adsorbed peptides deeper in the lipid membrane (especially for the more

hydrophobic pHLIPs: WT/Gla/Aad, Var3/GLL, and ATRAM) and/or a shift in peptide population from the solvated to the membrane-adsorbed state.

In contrast to tryptophan fluorescence changes, which are dependent on the location of tryptophan residues within the peptide sequence, the appearance of helicity is a more general parameter which can be compared among all peptides. In Fig. 2A (and Table S3), we give the ratio of ellipticity at 205 nm to 222 nm, an indicator of the degree of helicity (lower ratios indicate higher helicity), obtained for different peptides in different states. In state I, the lowest ratios were observed for pHLIP bundles, which correlate with the appearance of the exciton signal at 230 nm. In state II, the most structured peptides (ratios < 1.5) were PEG-4WT, WT/Gla/Aad, Var3/GLL, ATRAM, and PEG-2WT, which exhibited a higher affinity to the membrane and an increase in the peptide-inserted population at pH 8. At low pH, all peptides exhibited similar helical content, as expected from the formation of TM helices.

The transitions from state II to state III seen in steady-state and kinetics modes exhibited pK values in the range of pH 5.7 to 6.6 in the presence of physiological concentrations of calcium and magnesium ions, with the highest cooperativity observed for PEG-4WT, and transition times varying from 0.1 s to 37.5 s (Table 2). There are subtleties that affect the comparison and interpretation of the data such as: (i) The peptides are in different starting conditions in state II at pH 8 due to greatly differing overall peptide hydrophobicity; (ii) difference in peptides pK values, which reflect equilibrium between peptides' membrane-adsorbed and membrane-inserted populations; (iii) characteristic times, which report the movement of tryptophan residues into environments inside the membrane; however, since the tryptophan residues are located in different regions of each pHLIP, their movement into the membrane, as measured via changes in fluorescence parameters, should be expected to be different; and (iv) the cooperativity of the transition is a some-

what unstable parameter in the fitting of experimental pH- dependence data using the Henderson–Hasselbalch equation, especially if slopes are introduced at the initiation and completion of the transition (34). Lower values of cooperativity ($n < 1$) were observed for the peptides with tryptophan residues located at (Var3 group) or close (ATRAM) to the C terminus, which must be translocated across the cell membrane. ATRAM and Var3/GLL, which are the most hydrophobic pHLIPs and are therefore likely to be located more deeply than others in the membrane at pH 8, demonstrated the fastest times of insertion. As we showed previously, the removal of protonatable residues from the inserting C terminus increases the rate of the transition from state II to state III (24, 25). Thus, the group of Var3-like peptides exhibited fast insertion times ($t < 1$ s), a characteristic most attributable to the presence of less protonatable residues in the Var3-like peptides as well as a decrease in the number of these residues located at the C-terminal ends of the peptides. In the group of WT peptides, the time of insertion decreased as the hydrophobicity of the peptide increased, with insertion times listed in the following order (from longest to shortest time of insertion): WT, WT/Gla, WT/Gla/Aad, PEG-2WT, and PEG-4WT.

Intracellular delivery of polar cargo. We asked whether the pHLIP bundles could cause any acute cytotoxicity by themselves. HeLa cells were treated with either PEG-2WT or PEG-4WT at physiological pH (pH 7.4) and low pH (pH 6.0) for 2 h. We did not observe any cytotoxic effect at either pH, even when treating with concentrations up to 10 μ M (construct concentration is presented as concentration of WT pHLIP).

A proliferation assay was employed to evaluate the ability of pHLIPs to deliver the amanitin toxin, a relatively cell-impermeable, polar cargo molecule (35, 36). For amanitin to induce cytotoxicity, it must be translocated across the cell membrane, be released from the peptide carrier, and reach its target in the nucleus (RNA polymerase II). Amanitin was conjugated via a cleavable disulfide link to the inserting, C termini of the peptides. The

translocation capabilities of the pHLIP-amanitin conjugates were measured as the inhibition of proliferation of HeLa cells treated with increasing concentrations (up to 2 μM) of pHLIP-amanitin at either physiological pH (pH 7.4) or low pH (pH 6.0) for 2 h, followed by removal of the constructs, transfer of cells to normal cell culture media, and assessment of cell death at 48 h.

Each of the conjugates demonstrated pH-dependent cytotoxicity (Fig. S2). The calculated EC20, EC50, and EC80 at physiological and low pH are shown in Table 2. At low pH, the most potent constructs were the pHLIP bundles, which exhibited the highest cooperativity of transition from membrane-adsorbed to membrane-inserted states. The least toxic at normal pH among all constructs was Var3. Fig. 2B lists the therapeutic indexes (TIs), defined as the ratio of EC50 at pH 7.4 to EC50 at pH 6.0 for each case. A TI of about 9 was obtained for WT/Gla and Var3, and the TI was around 5.5 for PEG-2WT, Var3/Gla, and ATRAM. It is desirable to have high potency, which is defined as a difference between cell viability at low and physiological pHs at different concentrations of the construct (Fig. 3). All constructs had high potency (60 to 70%) at particular concentrations; however, just a few constructs, namely Var3, Var3/Gla, and WT/Gla, had a high, stable potency over a wide range of concentrations. The pHLIP bundles displayed the highest potency at the lowest concentrations (0.1 μM to 0.2 μM). The potency of ATRAM peaked at concentrations around 0.5 μM and declined sharply at higher concentrations; this decline is most likely associated with the increased hydrophobicity of ATRAM, which results in a high affinity for the cell membrane at normal and high pH and promotes the shift in equilibrium toward the membrane-inserted form that is associated with the translocation of cargo across the cell membrane.

Tumor targeting. To evaluate the tumor targeting and bio- distribution characteristics of the pHLIP variants, we conjugated the fluorescent dye Alexa Fluor 546 (AF546) to the noninserting, N termini of seven of the peptides. Our previous data indicate excellent tumor targeting by AF546-pHLIPs (9, 27). In the case of pHLIP bundles, AF546 was conjugated to the inserting, C termini of the PEG-2WT and PEG-4WT pHLIPs, as the N termini were occupied by PEG polymers. A well-established mouse model, using implanted cells of acidic 4T1 murine breast tumors, was used in the study; this model is targeted well by pHLIPs (9, 27). Following the development of breast tumors in the mouse flank, each fluorescent construct was introduced by a single tail vein injection. Animals were killed 4 h after the injection of the fluorescent conjugates, and the tumor and major organs (kidney, liver, lungs, spleen, and muscle) were collected and imaged. We selected the 4-h postinjection time point based on previous pharmacokinetics data which show that the highest tumor targeting with pHLIPs is observed 4 h after the injection of construct (9, 27). The mean values of the surface fluorescence intensity of tumors, muscle, and organs are given in Table S4. The normalized tumor fluorescence intensity (normalized by tumor uptake of AF546-WT) for all constructs is shown in Fig. 4A. The highest tumor targeting was observed for the Var3 construct, as well as for Var3/Gla and ATRAM. The tumor uptakes of the WT and Var3/GLL constructs were significantly reduced, by 1.6- and 2.6-fold, respectively, compared with the uptake of Var3. The uptakes of WT/Gla, WT/Gla/Aad, and the pHLIP bundles were reduced even further compared with the uptake of the WT construct. It is possible that the decreased tumor targeting observed in the PEG-pHLIP bundles might be attributed to the fact that the AF546 dye was conjugated to the C terminus, which is translocated into the cytosol. At the same time, the tumor-to-muscle ratio of the WT-like group was in the range of 5.4 to 7.5. The highest tumor-to-muscle ratios were observed for Var3 (T/M = 8.9) and PEG-2WT (T/ M = 7.5), and the lowest

ratio was observed in Var3/GLL (T/ M = 4.0) (Fig. 4B and Table S5). Among all constructs, only Var3/GLL demonstrated a tumor-to-kidney ratio less than 1 (Fig. 4C and Table S5). The highest tumor-to-liver ratio was found in Var3 and Var3/Gla (Fig. 4D and Table S5).

Because PEG-2WT-AF546 and PEG-4WT-AF546 are several times larger than the other pHLIP variants, we expected that they might have slower pharmacokinetics. Therefore, we also performed imaging at the 24-h postinjection time point for the two PEG-pHLIP conjugates; however, we did not observe any significant signal increase in tumors at 24 h postinjection compared with 4 h postinjection (Table S4).

Discussion

To advance cancer therapy using a range of agents with different properties, we have developed new versions of pHLIP variants and pHLIP bundles, and compared their performance to the performance of recently introduced variants with nonstandard amino acids (Gla and Aad) and the hydrophobic GLL motif. Our goal was to correlate the biophysical properties of the membrane interactions of different pHLIPs, including physiological concentrations of free calcium and magnesium ions, to the ability of these pHLIPs to move polar cargo across the cell membrane and to target acidic tumors.

The thermodynamic parameters of pK and cooperativity of pH-dependent transition from State II at pH 8 to State III at pH < 5 can be taken as predictors of the performance of a pHLIP for drug delivery and tumor targeting (17, 28, 29). While pK is a rather stable fitting parameter, the cooperativity parameter (Hill coefficient) might vary over a wide range resulting from different fittings which are within the level of accuracy of the experimental measurements. Moreover, if different binding affinities are assumed, the Hill formulation

loses validity. In general, highly cooperative transitions are hard to measure in biological systems with noise, especially when examining relatively short peptides like the class of pHLIP peptides (28). Only if the biological system is approximated to be infinite can a phase transition occur (37). Moreover, transition parameters for different peptides can only be truly compared when both peptides have precisely the same starting and ending states; although this condition is met for the membrane-inserted state (state III) of the peptides, which appears very similar among pHLIP variants, the condition that the initial state (state II) of the peptides be identical is not met. As hydrophobicity varies widely among peptides of the pHLIP family due to the difference in numbers of protonatable, polar, and hydrophobic residues and their location within the peptide sequences, the characteristics of the peptide population in the initial state of the transition also varies as these peptides position themselves at different interaction levels with the hydrophobic/hydrophilic boundary region of a bilayer.

The population percentages of inserted peptide presented in Table S6 were calculated from the pH-dependent transitions of pHLIP variants. The numbers represent the percentage of membrane-inserted peptides at varying pH assuming that, at the beginning of the transition (state II) (i.e., at physiological pH and higher), the population of inserted peptides is close to zero. In reality, close consideration of the interaction between a pHLIP variant and the membrane at pH 8, in conditions more alkaline than physiological conditions where the inserted peptide population should be even less than at physiological conditions, indicates that the most hydrophobic sequences, such as ATRAM and Var3/GLL, and bundled pHLIPs with multiple binding sites within a single construct, exhibit a significant inserted peptide population, as shown by the loss of pH-dependent differences in the translocation of the polar, cell-impermeable cargo amanitin with an increase in construct concentration (i.e., a decrease in potency at higher concentrations). Additionally, as previously shown

using the pore-forming peptide melittin, helix formation, membrane binding, and insertion properties are very sensitive to primary structure changes involving glycine and leucine residues (38). Ultimately, due to patient variability, it is highly desirable that potential therapeutic pHLIP constructs are able to discriminate between healthy and tumor tissue over a wide concentration range, meaning that a constant potency is necessary to avoid targeting normal tissue and the resulting significant side effects, suggesting that the properties of these variants may not be well suited for clinical development using agents that require tight targeting.

In addition to the steady-state experiments, it is important to probe tumor targeting and to examine the biodistribution of the constructs when injected into the high-flow-rate blood stream, since targeted delivery is always opposed by clearance from the blood. The best tumor targeting was shown by faster-inserting pHLIP constructs. Thus, in the design of new pHLIP variants, the biophysical kinetics parameters need to be considered in addition to the more traditionally prioritized steady-state properties. These kinetics parameters might be especially critical for the delivery and translocation of a cargo across a membrane, since we have shown that charges and the presence of cargo at the inserting end of a pHLIP can slow the process of insertion (24). Different cargoes linked to a pHLIP alter biodistribution and tumor targeting (27). Less polar pHLIP variants conjugated with hydrophobic cargoes might have a higher tendency toward targeting normal tissue and hepatic clearance. On the other hand, the size of links in pHLIP bundles could be used to tune biodistribution and redirect clearance from renal to hepatic.

Among the pHLIP variants we investigated, Var3 demonstrated excellent performance in vitro (the most stable potency over a wide range of concentrations) and high tumor targeting. Variants containing the Gla residue, especially the WT/Gla construct, showed an increase in the cooperativity of the membrane insertion transition as previously reported

(28), and showed an improved TI. However, the tumor targeting of WT/Gla was lower compared with the tumor targeting of WT.

The γ -carboxyglutamic acid is not naturally encoded in the human genome, but is introduced into proteins through the posttranslational carboxylation modification of glutamic acid, resulting in an amino acid with two carboxyl groups. Several proteins are known to have Gla-rich domains, including many coagulation factors, which coordinate calcium ions, inducing conformational changes in the proteins that enhance the hydrophobicity and affinity of the proteins to the cell membrane bilayer (39). Calcium complex formation by a pHLIP increases the hydrophobicity of the peptide and alters the interaction between peptide and membrane; this fact, along with the fact that the cost of synthesizing a Gla-containing peptide is very high (Gla is one of the most expensive amino acids) might somewhat reduce enthusiasm in using the Gla residue, but, if there were sufficient advantages in a specific case, the cost might be justified. While considering peptide synthesis, it is worthwhile to note that very hydrophobic pHLIP sequences (like ATRAM), especially when coupled with even moderately hydrophobic cargoes, might be challenging to produce in the large quantities needed for clinical translation.

There is no single recipe for the best pHLIP: The peptide will need to be tailored to each specific medical application. For example, kidney clearance might be preferred to liver clearance for PET-pHLIP imaging constructs (13). High tumor-to-normal tissue fluorescence intensity ratios will be the key in fluorescence-guided surgical applications (11). Delivery of highly toxic molecules, such as amanitin, would require minimal off-targeting; thus high potency and TI will be critical. However, for the delivery of polar peptide nucleic acids or other highly specific inhibitors of particular pathways in cancer cells, neither of which are associated with toxicity in normal cells, the requirement to reduce off-targeting might be much lower, and the emphasis would be shifted toward the

efficiency of delivery, the goal being to translocate as much cargo as possible (18, 40). The pHLIP bundles might yield excellent results in these types of applications, supported by the observation that PEG-4WT is the most efficient at delivering the polar molecule amanitin to the intracellular space. We believe that bundling multiple Var3 pHLIPs, in the same fashion that we linked two or four WT pHLIPs, might be more advantageous. Var3 demonstrates membrane insertion rates orders of magnitude faster than the insertion rates of WT; with the knowledge that faster insertion rates observed in biophysical experiments correlate to better tumor targeting in vivo, it stands to reason that potential PEG-Var3 constructs might demonstrate better tumor targeting still.

In drug delivery applications, pHLIP peptides are best designed for the delivery of polar, cell-impermeable molecules (14, 35, 41, 42). The intracellular delivery of a polar cargo could be further tuned by altering the link connecting the cargo to pHLIP and/or by attaching modulator molecules to the inserting end of the peptide (14, 15, 18, 35). Additionally, pHLIP could be used for the targeted delivery of cell-permeable, drug-like molecules since it can significantly increase the time of retention in blood, positively alter the biodistribution of drugs that typically rely on passive diffusion, and enhance tumor targeting, all of which would lead to an increase in TI (16). More polar pHLIP variants are expected to be better suited to applications involving the intracellular delivery of cell-permeable cargoes.

We have now established a set of properties for a number of pHLIPs, which can be selected as starting points for clinical development in different circumstances. This body of work, with the prior studies, opens pathways for targeted delivery using a range of imaging and therapeutic agents in the fight against cancer.

Materials and Methods

pHLIP characterization and pHLIP bundle synthesis. All peptides were purchased from CS Bio Co. Peptides were characterized by reversed phase high-performance liquid chromatography (RP-HPLC) using Zorbax SB-C18 and Zorbax SB-C8, 4.6×250 mm, 5 μm columns (Agilent Technology). For biophysical measurements, PEG-2WT and PEG-4WT were made by conjugating either 2 kDa bifunctional maleimide-PEG-maleimide or 2 kDa 4-arm PEG-maleimide (Creative PEGWorks) to Cys-WT via an N-terminal cysteine residue. Purification of the PEG-pHLIP constructs was conducted using RP-HPLC. Peptide concentration was calculated by absorbance at 280 nm, where, for WT, WT/Gla, and WT/Gla/Aad, $\epsilon_{280} = 13,940 \text{ M}^{-1} \text{ cm}^{-1}$; for Var3, Var3/Gla, and Var3/GLL, $\epsilon_{280} = 12,660 \text{ M}^{-1} \text{ cm}^{-1}$; and for ATRAM, $\epsilon_{280} = 5,690 \text{ M}^{-1} \text{ cm}^{-1}$. PEG construct concentration was presented in terms of peptide concentration, not molecular concentration.

Liposome preparation. Small unilamellar vesicles were used as model membranes and were prepared by extrusion. 1-palmitoyl-2-oleoyl-*sn*-glycero-3-phosphocholine (POPC; Avanti Polar Lipids) was dissolved in chloroform at a concentration of 12.5 mg/mL, then desolvated by rotary evaporation for two hours under vacuum. The resulting POPC film was rehydrated in 10 mM phosphate buffer at pH 8, either with additional calcium and magnesium ions (1.25 mM calcium and 0.65 mM magnesium), or without additional ions, vortexed, and extruded fifteen times through a membrane with a pore size of 50 nm.

Steady-state fluorescence measurements. Steady-state fluorescence spectra were measured using a PC1 spectrofluorometer (ISS) with temperature control set to 25.0 °C. The tryptophan fluorescence was excited using an excitation wavelength of 295 nm. Excitation and emission slits were set to 8 nm, and excitation and emission polarizers were set to 54.7° and 0.0°, respectively. Sample preparation was conducted 24 hours prior to

experiments to allow for State II equilibration. A buffer-only sample was used as a baseline for State I, and a buffer-with-POPC-only sample was used as a baseline for States II and III.

pH dependence measurements. Measurements of pH dependence were taken with the PC1 spectrofluorometer by using the shift in the position of maximum of peptide fluorescence as an indication of changes of the peptide environment at varying pH. All pH dependence measurements were conducted using blood physiological concentrations of free calcium and magnesium ions (1.25 and 0.65 mM, respectively). After the addition of hydrochloric acid, the pH of solutions containing 5 μ M peptide and 1 mM POPC were measured using an Orion PerHecTROSS Combination pH Micro Electrode and an Orion Dual Star pH and ISE Benchtop Meter (Thermo Fisher Scientific) before and after spectrum measurement to ensure equilibration. The tryptophan fluorescence spectrum at each pH was recorded, and the spectra were analyzed using the Protein Fluorescence and Structural Toolkit (PFAST) (42) to determine the positions of spectral maxima (λ_{\max}). The position of λ_{\max} was plotted as a function of pH and normalized, such that $\lambda_{\max}^{\text{initial}}$ – position of spectral maximum in State II was set to 1 and $\lambda_{\max}^{\text{final}}$ – position of spectral maximum in State III, was set to 0. The normalized pH-dependence was fit with the Henderson-Hasselbachequation (using OriginLab software) to determine the cooperativity (n) and transition mid-point (pK) of transition of the peptide population from State II to State III:

$$\text{Normalized pH dependence} = \frac{1}{1+10^{n(\text{pH}-pK)}} \quad (1)$$

Steady-state circular dichroism and oriented CD measurements. Steady-state CD was measured using an MOS-450 spectrometer (Bio-Logic Science Instruments) in the range of 190 to 260 nm with a step size of 1 nm, and with temperature control set to 25.0 °C. Samples were prepared 24 hours prior to experiments to allow for State II equilibration. A buffer-only sample was used as baseline for State I, and a buffer-with-POPC-only sample was used as baseline for States II and III.

OCD was measured using supported planar POPC bilayers prepared using a Langmuir-Blodgett system (KSV Nima). Fourteen quartz slides with 0.2 mm spacers were used; after sonicating the slides in 5% cuvette cleaner (Contrad 70; Decon Labs) in deionized water (≥ 18.2 M Ω cm at 25 °C; Milli-Q Type 1 Ultrapure Water System, EMD Millipore) for fifteen minutes and rinsing with deionized water, the slides were immersed and sonicated for ten minutes in 2-propanol, sonicated again for ten minutes in acetone, sonicated a final time in 2-propanol for ten minutes, and rinsed thoroughly with deionized water. Lastly, the slides were immersed in a 3:1 solution of sulfuric acid to hydrogen peroxide for five minutes and rinsed three times in deionized water. The slides were stored in deionized water until they were used. POPC bilayers were deposited on the fourteen slides using a Langmuir-Blodgett minitrough: a 2.5 mg/mL solution of POPC in chloroform was spread on the subphase (deionized water) and the chloroform was allowed to evaporate for fifteen minutes, after which the POPC monolayer was compressed to 32 mN/m. A lipid monolayer was deposited on the slides by retrieving them from the subphase, after which a solution of 10 μ M peptide and 500 μ M of 50 nm POPC liposomes at pH 4 was added to the slides, resulting in the creation of the supported bilayer by fusion between the monolayer on the slides and the peptide-laden lipid vesicles. After incubation for six hours at 100% humidity, the slides were rinsed with buffer solution to remove excess liposomes, and the spaces between the cuvettes were filled with buffer at pH 4.

Measurements were taken at three points during the experiment: immediately after the addition of the peptide/lipid solution (0 h), after the slides were rinsed to remove excess liposomes following the six-hour incubation time (6 h), and after an additional twelve-hour incubation time and rinse with buffer (18 h); these measurements were recorded on the MOS-450 spectrometer with sampling times of two seconds at each wavelength. Control measurements were conducted using a peptide solution between slides without supported bilayers and in the presence of POPC liposomes.

Kinetics measurements. Stopped-flow fluorescence measurements were made using an SFM-300 mixing system (Bio-Logic Science Instruments) in conjunction with the MOS-450 spectrometer. All solutions were degassed for fifteen minutes prior to loading into the stopped-flow system. pHLIP variants were incubated with POPC for 24 hours prior to the experiment to reach State II equilibrium, and insertion was induced by mixing equal volumes of pHLIP/POPC solutions with hydrochloric acid diluted to ensure a pH drop from pH 8 to pH 4. Kinetics data were fit by one-, two-, three-, or four-state exponential models in OriginLab.

Amanitin pHLIP conjugates. α -amanitin (Sigma-Aldrich) was conjugated to succinimidyl 3-(2-pyridyldithio)propionate (SPDP; Thermo Fisher Scientific), followed by purification and conjugation of the SPDP-amanitin to the C-terminal cysteine residues of pHLIP peptides. For synthesis of PEG-2WT-amanitin and PEG-4WT-amanitin, Lys-WT-Cys with N-terminal lysine and C-terminal cysteine residues was used, and the Lys-WT-SPDP-amanitin was conjugated to dibenzocyclooctyne-sulfo-N-hydroxysuccinimidyl ester (DBCO-NHS ester; Sigma-Aldrich), resulting in DBCO-WT-SPDP-amanitin. Finally, 2-arm or 4-arm PEG-azide (Creative PEGWorks) was conjugated to DBCO-WT-

SPDP-amanitin, resulting in PEG-DBCO-WT-SPDP-amanitin, with a cleavable disulfide bond present in SPDP, between the peptide and amanitin cargo. Construct concentration was calculated by absorbance at 310 nm, where, for α -amanitin, $\epsilon_{310} = 13,000 \text{ M}^{-1} \text{ cm}^{-1}$. Construct concentration was presented in terms of peptide/amanitin concentration. Purification was conducted using RP-HPLC. Zorbax SB-C18 columns ($9.4 \times 250 \text{ mm}$, $5 \mu\text{m}$; Agilent Technologies) were used for all peptide-amanitin conjugates other than ATRAM-amanitin, PEG-2WT-amanitin, and PEG-4WT-amanitin, for which Zorbax SB-C8 columns ($9.4 \times 250 \text{ mm}$, $5 \mu\text{m}$; Agilent Technologies) were used.

Cell proliferation assay. Human cervix adenocarcinoma cells (HeLa; American Type Culture Collection) were authenticated, stored according to the instructions of the supplier, and used within three months of frozen aliquot resuscitation. Cells were cultured in Dulbecco's modified Eagle's medium (DMEM; Sigma-Aldrich) at pH 7.4 with 4.5 g/L D-glucose, supplemented with 10% heat-inactivated fetal bovine serum (FBS; Sigma-Aldrich) and 10 $\mu\text{g/mL}$ ciprofloxacin (Sigma-Aldrich), in a humidified atmosphere of 5% CO_2 and 95% air at 37 $^\circ\text{C}$. The pH 6.0 medium was prepared by mixing 13.3 g of dry DMEM in 1 L of deionized water. HeLa cells were loaded in the wells of 96-well plates (5,000 cells/well) and incubated overnight. The standard growth medium was replaced with medium without FBS, at pH 6.0 or 7.4, containing increasing amounts of pHLIP-amanitin conjugates (from 0 to 2.0 μM). Treatment with amanitin alone for two hours and at concentrations up to 2 μM does not induce cell death (35). After two-hour incubation with the pHLIP-amanitin conjugates, the constructs were removed and replaced with standard growth medium. Cell viability was assessed after 48 hours using the CellTiter 96 AQueous One Solution Cell Proliferation Assay (Promega); the colorimetric reagent was added to cells for one hour, followed by absorption measurement at 490 nm. All samples were

prepared in triplicate, and each experiment was repeated between 3 and 6 times. All obtained cell proliferation data were normalized by corresponding controls (non-treated cells). There was no difference in the viability of cells incubated with media, without construct, at pH 7.4 and pH 6.0; therefore, the role of pH was excluded from the consideration. Normalized cell viability data obtained in different experiments were averaged and presented in terms of the logarithm of dose of pHLIP-amanitin constructs. The dose-response function was used for fitting the obtained data (Figure S2) (OriginLab):

$$Cell\ Viability = A_b + \frac{A_t - A_b}{1 + 10^{p(\log x_0 - x)}} \quad (2)$$

where A_b and A_t are the bottom and the top asymptotes, respectively. The top asymptote was set as constant (100%) while for the bottom asymptote we allowed small variations in the range of 0 to 10%. p is the slope (cooperativity parameter) and $\log x_0$ is the center of the transition (i.e., the concentration for half response) which is used to calculate the EC_{20} , EC_{50} , EC_{80} values:

$$EC_{20} = 10^{(\log x_0 + \log 0.25/p)} \quad (3)$$

$$EC_{50} = 10^{\log x_0} \quad (4)$$

$$EC_{80} = 10^{(\log x_0 + \log 4/p)} \quad (5)$$

Therapeutic index (TI) was calculated according to the equation:

$$TI = \frac{EC_{50}^{pH\ 7.4}}{EC_{50}^{pH\ 6.0}} \quad (6)$$

Additionally, the cytotoxicity of the PEG-2WT and PEG-4WT constructs without amanitin was tested: these experiments demonstrated no cytotoxicity at physiological or low pH at treatment concentrations up to 10 μ M.

Fluorescent pHLIP conjugates. Alexa Fluor 546 (AF546) C₅ maleimide (Thermo Fisher Scientific) was conjugated to the N-terminal cysteine residues of WT, Var3, Var3/Gla, and ATRAM. AF546 NHS Ester (Thermo Fisher Scientific) was conjugated to the N-terminal lysine residues of WT/Gla, WT/Gla/Aad, and Var3/GLL. For PEG-2WT and PEG-4WT, Cys-WT-Lys, with N-terminal cysteine and C-terminal lysine residues, was used, and was first conjugated to 2-arm maleimide-PEG-maleimide or 4-arm PEG-maleimide resulting in PEG-WT-Lys. Then, AF546 NHS Ester was conjugated to the C-terminal lysine residue, resulting in 2-arm and 4-arm PEG-pHLIP constructs with C-terminal AF546 fluorophores. Construct concentration was calculated by absorbance at 554 nm, where, for AF546, $\epsilon_{554} = 93,000\ \text{M}^{-1}\ \text{cm}^{-1}$. Construct concentration was presented in terms of AF546/peptide concentration, not molecular concentration. Purification was conducted using RP-HPLC for all peptides other than PEG-4WT-AF546, which was purified via Amicon Ultra MWCO 10 kDa centrifugal filter (Sigma-Aldrich). Zorbax SB-C18 columns (9.4 \times 250 mm, 5 μ m; Agilent Technologies) were used for all AF546-peptide conjugates except AF546-ATRAM and PEG-2WT-AF546, for which Zorbax SB-C8 columns (9.4 \times 250 mm, 5 μ m; Agilent Technologies) were used.

Ex vivo imaging. All animal studies were conducted according to the animal protocol AN04-12-011 approved by the Institutional Animal Care and Use Committee at the

University of Rhode Island, in compliance with the principles and procedures outlined by the National Institutes of Health for the care and use of animals. Mouse mammary cells (4T1; American Type Culture Collection) were subcutaneously implanted in the right flank (8×10^5 cells/0.1 mL/flank) of adult female BALB/cAnNHsd mice (Envigo). When tumors reached approximately 5-6 mm in diameter, single tail vein injections of 100 μ L, 40 μ M fluorophore-pHLIP solutions in PBS were performed. Mice were euthanized 4 or 24 hours after injection, and necropsy was immediately performed. Tumors and major organs were cut in half and imaged using an FX Kodak in-vivo image station connected to an Andor CCD camera. Mean surface fluorescence intensity of tumor, tissue and organs was obtained via analysis of fluorescence images in ImageJ (NIH) (43). The corresponding autofluorescence signal was subtracted to obtain the net fluorescence intensities used in the study. Autofluorescence was calculated after imaging tumors, tissue, and organs collected from mice with no injection of fluorescent pHLIP constructs.

Acknowledgements

We are grateful to Dr. Dhammika Weerakkody for his assistance and helpful discussions. The research reported in this publication was supported in part by the National Institute of General Medical Sciences of the National Institutes of Health under award number R01GM073857 to OAA, YKR, and DME, and in part by the Institutional Development Award (IDeA) Network for Biomedical Research Excellence from the National Institute of General Medical Sciences of the National Institutes of Health under grant number P20GM103430.

References

1. Marusyk A & Polyak K (2010) Tumor heterogeneity: causes and consequences. *Biochim Biophys Acta* 1805(1):105.
2. Gillies RJ, Verduzco D, & Gatenby RA (2012) Evolutionary dynamics of carcinogenesis and why targeted therapy does not work. *Nat Rev Cancer* 12(7):487-493.
3. Lloyd MC, *et al.* (2016) Darwinian Dynamics of Intratumoral Heterogeneity: Not Solely Random Mutations but Also Variable Environmental Selection Forces. *Cancer Res* 76(11):3136-3144.
4. Estrella V, *et al.* (2013) Acidity generated by the tumor microenvironment drives local invasion. *Cancer Res* 73(5):1524-1535.
5. Zhang X, Lin Y, & Gillies RJ (2010) Tumor pH and its measurement. *J Nucl Med* 51(8):1167-1170.
6. Hashim AI, Zhang X, Wojtkowiak JW, Martinez GV, & Gillies RJ (2011) Imaging pH and metastasis. *NMR Biomed* 24(6):582-591.
7. Anderson M, Moshnikova A, Engelman DM, Reshetnyak YK, & Andreev OA (2016) Probe for the measurement of cell surface pH in vivo and ex vivo. *Proc Natl Acad Sci USA* 113(29):8177-8181.
8. Reshetnyak YK, *et al.* (2011) Measuring tumor aggressiveness and targeting metastatic lesions with fluorescent pHLIP. *Mol Imaging Biol* 13(6):1146-1156.
9. Adochite RC, *et al.* (2014) Targeting breast tumors with pH (low) insertion peptides. *Mol Pharm* 11(8):2896-2905.
10. Tapmeier TT, *et al.* (2015) The pH low insertion peptide pHLIP Variant 3 as a novel marker of acidic malignant lesions. *Proc Natl Acad Sci USA* 112(31):9710-9715.

11. Golijanin J, *et al.* (2016) Targeted imaging of urothelium carcinoma in human bladders by an ICG pHLIP peptide ex vivo. *Proc Natl Acad Sci USA* 113(42):11829-11834.
12. Macholl S, *et al.* (2012) In vivo pH imaging with (99m)Tc-pHLIP. *Mol Imaging Biol* 14(6):725-734.
13. Demoin DW, *et al.* (2016) PET imaging of extracellular pH in tumors with ⁶⁴Cu- and ¹⁸F-labeled pHLIP peptides: A structure-activity optimization study. *Bioconjugate Chem* 27(9):2014-2023.
14. Andreev OA, *et al.* (2010) pH (low) insertion peptide (pHLIP) inserts across a lipid bilayer as a helix and exits by a different path. *Proceedings of the National Academy of Sciences* 107(9):4081-4086.
15. Wijesinghe D, Engelman DM, Andreev OA, & Reshetnyak YK (2011) Tuning a polar molecule for selective cytoplasmic delivery by a pH (Low) Insertion Peptide. *Biochemistry* 50(47):10215-10222.
16. Burns KE, Robinson MK, & Thévenin D (2015) Inhibition of cancer cell proliferation and breast tumor targeting of pHLIP-monomethyl auristatin E conjugates. *Mol Pharm* 12(4):1250-1258.
17. Burns KE, Hensley H, Robinson MK, & Thevenin D (2017) Therapeutic efficacy of a family of pHLIP-MMAF conjugates in cancer cells and mouse models. *Mol Pharm* 14(2):415-422.
18. Cheng CJ, *et al.* (2015) MicroRNA silencing for cancer therapy targeted to the tumor microenvironment. *Nature* 518(7537):107-110.
19. Yao L, *et al.* (2013) pHLIP peptide targets nanogold particles to tumors. *Proc Natl Acad Sci USA* 110(2):465-470.

20. Daniels JL, Crawford TM, Andreev OA, & Reshetnyak YK (2017) Synthesis and characterization of pHLIP® coated gold nanoparticles. *Biochem Biophys Rep* 10:62-69.
21. Yao L, Daniels J, Wijesinghe D, Andreev OA, & Reshetnyak YK (2013) pHLIP(®)-Mediated Delivery of PEGylated Liposomes to Cancer Cells. *J Control Release* 167(3):228-237.
22. Reshetnyak YK, Segala M, Andreev OA, & Engelman DM (2007) A Monomeric Membrane Peptide that Lives in Three Worlds: In Solution, Attached to, and Inserted across Lipid Bilayers. *Biophys J* 93(7):2363-2372.
23. Reshetnyak YK, Andreev OA, Segala M, Markin VS, & Engelman DM (2008) Energetics of peptide (pHLIP) binding to and folding across a lipid bilayer membrane. *Proc Natl Acad Sci USA* 105(40):15340-15345.
24. Karabadzhak AG, *et al.* (2012) Modulation of the pHLIP transmembrane helix insertion pathway. *Biophys J* 102(8):1846-1855.
25. Weerakkody D, *et al.* (2013) Family of pH (low) insertion peptides for tumor targeting. *Proc Natl Acad Sci USA* 110(15):5834-5839.
26. Cruz-Monserrate Z, *et al.* (2014) Targeting Pancreatic Ductal Adenocarcinoma Acidic Microenvironment. *Sci Rep* 4:4410.
27. Adochite RC, *et al.* (2016) Comparative study of tumor targeting and biodistribution of pH (low) insertion peptides (pHLIP peptides) conjugated with different fluorescent dyes. *Mol Imaging Biol* 113(42):11829-11834.
28. Onyango JO, *et al.* (2015) Noncanonical amino acids to improve the pH response of pHLIP insertion at tumor acidity. *Angew Chem Int Edit* 54(12):3658-3663.
29. Nguyen VP, Alves DS, Scott HL, Davis FL, & Barrera FN (2015) A novel soluble peptide with pH-responsive membrane insertion. *Biochemistry* 54(43):6567-6575.

30. Hunt JF, Rath P, Rothschild KJ, & Engelman DM (1997) Spontaneous, pH-dependent membrane insertion of a transbilayer alpha-helix. *Biochemistry* 36(49):15177-15192.
31. Cabaniss SE, Pugh KC, Pedersen LG, & Hiskey RG (1991) Proton, calcium, and magnesium binding by peptides containing gamma-carboxyglutamic acid. *Int J Pept Prot Res* 37(1):33-38.
32. Shikamoto Y, Morita T, Fujimoto Z, & Mizuno H (2003) Crystal structure of Mg²⁺- and Ca²⁺-bound Gla domain of factor IX complexed with binding protein. *J Biol Chem* 278(26):24090-24094.
33. Huang M, Furie BC, & Furie B (2004) Crystal structure of the calcium-stabilized human factor IX Gla domain bound to a conformation-specific anti-factor IX antibody. *J Biol Chem* 279(14):14338-14346.
34. Barrera FN, *et al.* (2011) Roles of carboxyl groups in the transmembrane insertion of peptides. *J Mol Biol* 413(2):359-371.
35. Moshnikova A, Moshnikova V, Andreev OA, & Reshetnyak YK (2013) Anti-proliferative effect of pHLIP-amanitin. *Biochemistry* 52(7):1171-1178.
36. Weerakkody D, *et al.* (2016) Novel pH-sensitive cyclic peptides. *Sci Rep* 6:31322.
37. Sharma GP, Reshetnyak YK, Andreev OA, Karbach M, & Müller G (2015) Coil-helix transition of polypeptide at water-lipid interface. *J Stat Mech-Theory E* P01034.
38. Krauson AJ, *et al.* (2015) Conformational fine-tuning of pore-forming peptide potency and selectivity. *J Am Chem Soc* 137:16144–16152.

39. Kalafatis M, Egan JO, van't Veer C, & Mann KG (1996) Regulation and regulatory role of gamma-carboxyglutamic acid containing clotting factors. *Crit Rev Eukaryot Gene Expr* 6(1):87-101.
40. Reshetnyak YK, Andreev OA, Lehnert U, & Engelman DM (2006) Translocation of molecules into cells by pH-dependent insertion of a transmembrane helix. *Proc Natl Acad Sci USA* 103(17):6460-6465.
41. Burns KE & Thévenin D (2015) Down-regulation of PAR1 activity with a pHLIP-based allosteric antagonist induces cancer cell death. *Biochem J* 472(3):287-295.
42. Burns KE, McCleerey TP, & Thévenin D (2016) pH-selective cytotoxicity of pHLIP-antimicrobial peptide conjugates. *Sci Rep* 6:28465.

TABLES

Table 1. List of pHILIP sequences used in the study.

Peptide	Sequence
Cys-WT	ACEQNPIYWAR YADWLFTTPLL LLDLALLVDADEGT
WT-Cys	AEQNPIYWAR YADWLFTTPLL LLDLALLVDADEGCT
Lys-WT-Cys	Ac-AKEQNPIYWAR YADWLFTTPLL LLDLALLVDADECT
Lys-WT/Gla-Cys	Ac-AKEQNPIYWAR YAGlaWLFTTPLL LLDLALLVDADECT
Lys-WT/Gla/Aad-Cys	Ac-AKEQNPIYWAR YAGlaWLFTTPLL LLAadLALLVDADECT
Cys-Var3	ACDDQNPWRAYLDLLFPTDTLLLDLLWA
Var3-Cys	ADDQNPWRAYLDLLFPTDTLLLDLLWCA
Cys-Var3/Gla	ACDDQNPWRAYLGlaLLFPTDTLLLDLLWG
Var3/Gla-Cys	ADDQNPWRAYLGlaLLFPTDTLLLDLLWCG
Lys-Var3/GLL-Cys	Ac-GKEEQNPWLGAYLDLLFPLELLG LLELGLWCG
Cys-ATRAM	ACGLAGLAGLLGLEGLLGLPLGLEGLWLGLELEGN
ATRAM-Cys	GLAGLAGLLGLEGLLGLPLGLEGLWLGLELEGNCA

Table 2. The midpoint (pK), cooperativity (n), and time (t) parameters characterizing the pH-dependent transition of pHLIP variants in the presence of POPC liposomes are presented. EC_{20} , EC_{50} , and EC_{80} values were calculated for each pHLIP-amanitin construct at physiological and low pH by analyzing the pH- and concentration-dependent cell viability data (Figure S2).

Peptide	pK	n	t (s)	EC_{20} (μM)		EC_{50} (μM)		EC_{80} (μM)	
				pH 7.4	pH 6.0	pH 7.4	pH 6.0	pH 7.4	pH 6.0
WT	6.5	1.8	36.8	1.95	1.22	1.37	0.56	0.96	0.26
WT/Gla	6.2	1.5	37.5	6.20	0.93	2.73	0.30	1.20	0.10
WT/Gla/Aad	6.6	1.4	34.8	3.01	0.66	1.39	0.37	0.64	0.21
PEG-2WT	6.6	1.8	18.8	1.98	0.54	1.03	0.19	0.53	0.07
PEG-4WT	6.6	2.2	13.1	0.473	0.19	0.33	0.11	0.23	0.06
Var3	5.7	0.9	0.9	10.63	1.30	3.95	0.43	1.47	0.14
Var3/Gla	6.3	0.7	0.7	5.12	1.34	2.76	0.50	1.48	0.19
Var3/GLL	6.6	0.4	0.1	1.75	0.47	0.91	0.23	0.47	0.11
ATRAM	6.4	0.9	0.1	2.06	0.40	1.23	0.22	0.74	0.12

FIGURES

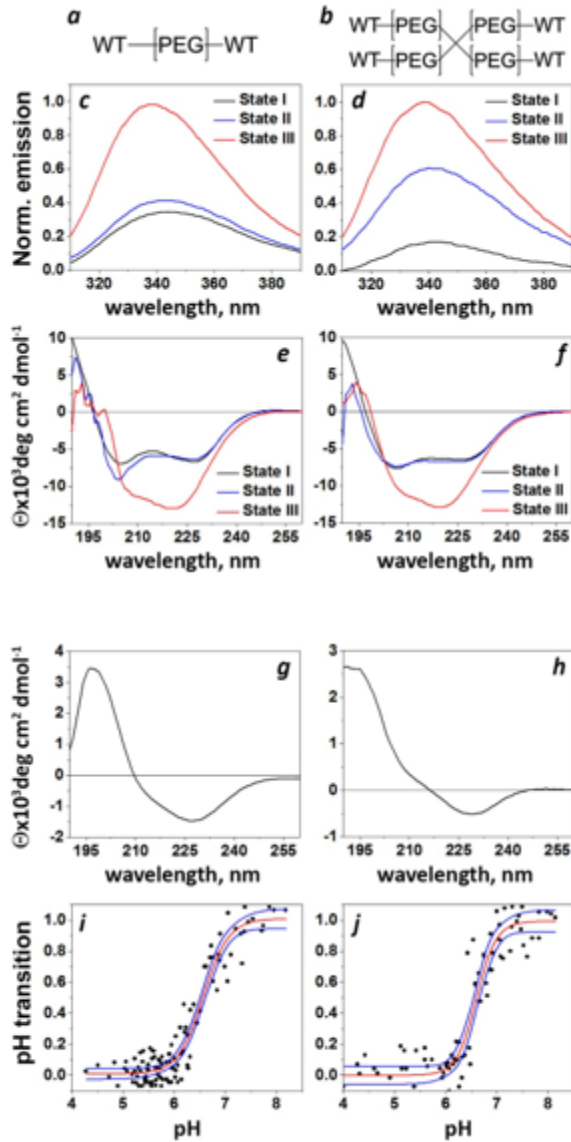


Figure 1. Schematic organization of pHLIP bundles: *(a)* PEG-2WT with 2 kDa 2-arm PEG and two WT pHLIPs, and *(b)* PEG-4WT with 2 kDa 4-arm PEG and four WT pHLIPs. Transitions between the three states of PEG-2WT and PEG-4WT in phosphate buffer at pH 8 (State I), in the presence of POPC liposomes at pH 8 (State II), and in the presence of liposomes at pH 4 (State III) were monitored by changes of tryptophan fluorescence (*c* and *d*), circular dichroism (*e* and *f*), and oriented circular dichroism (OCD) (*g* and *h*) signals. Normalized pH-dependent steady-state transitions from State II to State III were examined by analyzing the shift in position of fluorescence spectrum maximum of PEG-2WT (*i*) and PEG-4WT (*j*) in the presence of physiological concentrations of calcium and

magnesium ions. The data were fitted using the Henderson-Hasselbalch equation; the fitting curves and 95% confidence interval are shown by red and blue lines, respectively.

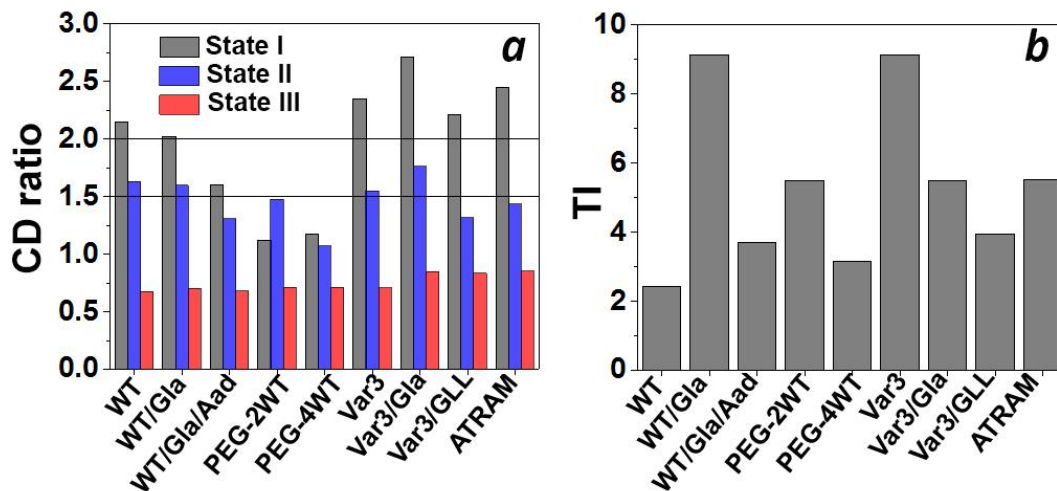


Figure 2. Ellipticity ratios of CD signals at 205 nm to 222 nm are shown for pHLIP variants in State I, II, and III (*a*). The values of ellipticity ratios are given in Table S3. The therapeutic index (TI) was calculated for different pHLIP-amanitin constructs as the ratio of EC_{50} at pH 7.4 to EC_{50} at pH 6.0 (*b*).

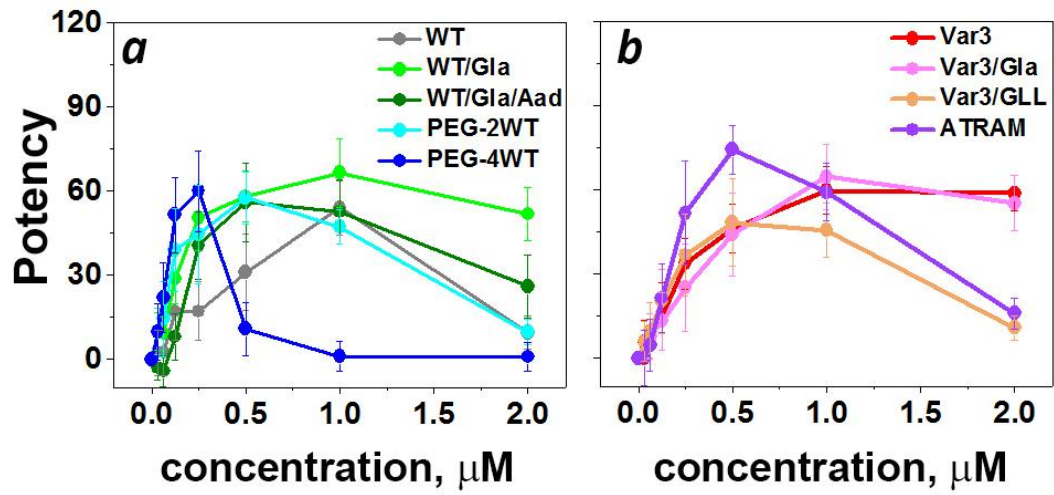


Figure 3. pH-dependent potency was defined as the difference between cancer cell viability when cells were incubated at pH 7.4 and pH 6.0 at varying concentrations of different pHLIP-amanitin constructs. The WT-like group is shown in (a); the Var3-like group and ATRAM are shown in (b).

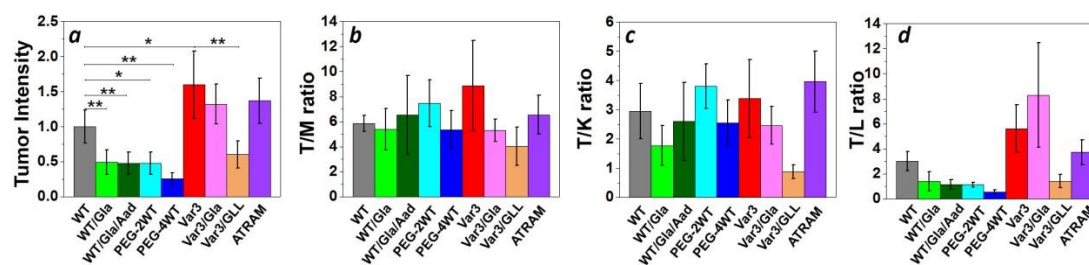


Figure 4. Normalized tumor fluorescence intensities of the AF546-pHLIP constructs are shown; the signals were normalized by the tumor intensity of AF546-WT (**a**). Tumor-to-muscle (T/M) (**b**), tumor-to-kidney (T/K) (**c**), and tumor-to-liver (T/L) (**d**) fluorescence intensity ratios are shown. Statistically significant differences were determined by two-tailed unpaired Student's t-test, where * denotes $p \leq 0.05$ and ** denotes $p \leq 0.005$.

CHAPTER 2

Published in Trends in Biochem Biophys reports in July 2017

Synthesis and Characterization of pHLIP[®] Coated Gold Nanoparticles

Jennifer L. Daniels, Troy M. Crawford, Oleg A. Andreev, Yana K. Reshetnyak*

**Physics Department, University of Rhode Island, 2 Lippitt Rd., Kingston, RI 02881, USA*

Abstract

Novel approaches in synthesis of spherical and multispiked gold nanoparticles coated with polyethylene glycol (PEG) and pH Low Insertion Peptide (pHLIP®) were introduced. The presence of a tumor-targeting pHLIP® peptide in the nanoparticle coating enhances the stability of particles in solution and promotes a pH-dependent cellular uptake. The spherical particles were prepared with sodium citrate as a gold reducing agent to form particles of 7.0 ± 2.5 nm in mean metallic core diameter and ~ 43 nm in mean hydrodynamic diameter. The particles that were injected into tumors in mice (21 μ g of gold) were homogeneously distributed within a tumor mass with no staining of the muscle tissue adjacent to the tumor. Up to 30% of the injected gold dose remained within the tumor one hour post-injection. The multispiked gold nanoparticles with a mean metallic core diameter of 146.0 ± 50.4 nm and a mean hydrodynamic size of ~ 161 nm were prepared using ascorbic acid as a reducing agent and disk-like bicelles as a template. Only the presence of a soft template, like bicelles, ensured the appearance of spiked nanoparticles with resonance in the near infrared region. The irradiation of spiked gold nanoparticles by an 805 nm laser led to the time- and concentration-dependent increase of temperature. Both pHLIP® and PEG coated gold spherical and multispiked nanoparticles might find application in radiation and thermal therapies of tumors.

Introduction

Gold nanoparticles (ranging in size from 1 to 200 nm) might find various applications in medicine including the enhancement of x-ray radiation damage to tumor tissues [1–4] and the induction of localized heating in photothermal therapy [5–7]. The latter is achieved when gold nanoparticles are exposed to light and impart heat energy to their

local environment due to the temporary existence and decay of localized surface plasmon polaritons. In addition of use of gold nanoparticles, also supermagnetic nanoparticles are developed for magnetic resonance imaging and hyperthermia to induce cancer cells death or promote drug release [8–13]. In all cases of nanoparticle use, not only should the particles be stable, but they should preferentially target diseased tissue, such as a cancerous tumor.

Many contemporary therapeutic and imaging approaches to cancer treatment rely on tumor-targeting biomarkers such as antibody technologies or vitamin binding [14–18]. Although there are significant successes, the inter- and intra-heterogeneity of tumors, their complexity, and their ability to adapt to new conditions often create parts of a tumor that may not express enough of the biomarker to be targeted. This results in the regrowth of resistant tumors and poor therapeutic outcomes, where the average improvements in survival are measured in months. At the same time, there is an emerging body of evidence indicating that the acidity of the tumor tissue plays a key role in determining cancer cell invasiveness and resistance to therapies. Tumors exhibit marked heterogeneity due to genetic alterations, which lead to the modification of biochemical pathways. The modifications that result from metabolic alterations, lead to a surge in extracellular acidity. Tumor cells adapt to this acid-induced toxic environment by stimulating proteins that regulate intracellular homeostasis [19,20].

Among pH-targeting agents, the family of pH Low Insertion Peptides (pHLIP®) find a broad range of applications in biomedical sciences. pHLIP® peptides insert across cellular membranes in a pH-dependent manner, with one terminus exposed to the extracellular space and the other terminus to the cytoplasm [21–24]. The molecular mechanism of a pHLIP® peptide's action is based on the protonation of Asp/Glu residues, which enhances the peptide's hydrophobicity and promotes membrane-

associated folding with the insertion of a transmembrane helix [25,26]. It was shown that pHLIP® peptides are excellent at targeting acidic tumors, which allows for the specific delivery of imaging and therapeutic agents to cancer cells within tumors [22,27–29]. The number and variety of pHLIP® based nanomedicines is growing. For example, the coating of lipid-based, polymeric, and metallic nanoparticles with pHLIP® peptides enhances the targeting of acidic tumors and the number of particles internalization within cancer cells [30–36].

We have shown specific tumor accumulation of gold nanoclusters of 1.4 nm in diameter conjugated to the pHLIP® peptide [37], and an enhancement of radiation effect observed for cancer cells treated with pHLIP® gold nanoclusters [38]. As well, novel photo-induced pHLIP® coated hollow gold nanospheres containing chlorine 6 were introduced recently [33,34]. The nanospheres experience hyperthermia within 5 min of laser exposure, which leads to the release of photosensitizers due to the reduction of electrostatic interaction. While the obtained results are very interesting and promising, there are aspects which require improvement and justify further work: i) the coating of gold nanoclusters conjugated with pHLIP® peptide should be improved to avoid particles aggregation; and ii) a greater amount of gold might be needed in tumors to observe a significant radiation enhancement effect. Therefore, here we introduce novel approaches for synthesis of pHLIP® and PEG coated spherical and spiked gold nanoparticles for the enhancement of radiation damage and near infrared (NIR) thermal therapy.

Materials and Methods

2.1. Materials for synthesis of pHLIP® and PEG coated gold nanoparticles

Gold III chloride, 5% solution, was purchased from Salt Lake Metals (Salt Lake City, UT). Sodium citrate tribasic, L-ascorbic acid, and urea dehydrate were purchased from Sigma-Aldrich Co. (St. Louis, MO). The wild type (WT) pHLIP® peptide:

ACEQNPIYWARYADWLFTTPLLALLVDADET

was synthesized and purified by C.S. Bio Co. (Menlo Park, CA), and the concentration of the peptide was determined by absorbance at 280 nm ($\epsilon=13,940 \text{ M}^{-1} \text{ cm}^{-1}$). The m-polyethylene glycol-SH (mPEG-SH), about 5 kDa in mass, was purchased from Creative PEGworks (Chapel Hill, NC). The lipids, 1,2-dihexanoyl-sn-glycero-3-phosphocholine, D6PC; 1,2-diheptanoyl-sn-glycero-3-phosphocholine, D7PC/DHPC and 1,2-dimyristoyl-sn-glycero-3-phosphocholine, DMPC were purchased from Avanti Polar Lipids, Inc (Alabaster, AL). Tris-(2-carboxyethyl) phosphine hydrochloride (TCEP) was purchased from Thermo Fisher Scientific (Waltham, MA). The procedures for synthesis of the spherical and multispiked pHLIP® and PEG coated gold nanoparticle are described in the Results section.

2.2. Bicelle preparation

Bicelles were prepared by thin-film method: a chloroform solution of DMPC and D7PC (DHPC) lipids were dried using a rotary evaporator producing an even thin film, followed by the additional overnight evaporation under a high vacuum to remove traces of organic solvents. The lipid layer was re-suspended in 10 mM phosphate buffer pH 6.5 and underwent ten freeze-thaw-vortex cycles using liquid nitrogen and a warm bath (40 °C).

2.3. Purification of gold nanoparticles

To remove large particles (in the case of spherical gold nanoparticles) and excess reducing agents, the final solution of particles underwent two forms of filtration. Large particles were removed using centrifugation (5 min at 10,000 relative centrifugal force, RCF). Excess reducing agents were removed by size-exclusion chromatography using sephadex G25 fast spin columns. 500 μ L of particles were added to 5 mL of sephadex G25 gel filtration beads (Sigma-Aldrich Co.) (the beads were hydrated in the desired buffer) and centrifuged for 0.5 min increments at roughly 36 RCF. The final nanoparticle solutions were passed through a 0.2 μ m sterile Acrodisc® syringe filter with HT Tuffryn® membrane (Pall Life Sciences) for sterilization when experiments on cultured cells and mice were carried out, as well as for stability studies and heating experiments.

2.4. UV–visible absorption spectroscopy

The absorbance of gold nanoparticles was recorded on a Genesys 10S UV–Vis Spectrophotometer to establish the wavelength range of resonance.

2.5. Measurements of particles size

The size of bicelles and gold nanoparticles in solution was measured by dynamic light scattering (DLS) using a Zetasizer Nano ZS (Malvern) instrument and a nanoparticle tracking system, Nanosight (NS300, Malvern), respectively. Transmission electron microscopy (TEM) (JEOL 2100) with an accelerating voltage of 200 kV at

magnifications in the range of 10,000 \times to 150,000 \times was used to image gold nanoparticles to establish the shape, size, and homogeneity of the particles. Samples were prepared for TEM by drying 5 μ L of the nanoparticle solution on a carbon type-B, 300 mesh, copper grid (Ted Pella, Inc). Size histograms were averaged and fitted with a Gaussian function.

2.6. ICP-MS analysis

The investigated samples (cells, tumor tissue, or nanoparticles in solution) were dissolved in a concentrated solution of aqua regia (1:3 volume ratio of nitric acid and hydrochloric acid) and sonicated. The final solutions were diluted to 2% (wt/vol) nitric acid with distilled water and centrifuged to remove organic tissue. The gold content was quantified using inductively coupled plasma mass spectrometry (ICP- MS) (Thermo scientific X7 series and Thermo X-Series 2 quadrupole) by using calibration standards IMS 103 (UltraScientific).

2.7. Heating

In a poly(methyl methacrylate) (PMMA) cuvette (with a 4.5 mm window width and 12.5 mm depth), 300 μ L of solution was illuminated by an 805 nm temperature controlled laser diode with 500 mW output (TCLDM9, Thorlabs). The solution temperature was measured every minute with an immobilized FLIR E6 thermal imager (FLIR Systems, Inc.) from above to avoid obstruction by the cuvette walls. A sample of phosphate-buffered saline (PBS), pH 7.4, was illuminated and used as a baseline.

2.8. Cancer cells

JC murine mammary-gland adenocarcinoma cells were obtained from the American Type Culture Collection (ATCC). The cells were cultured in Roswell Park Memorial Institute (RPMI) medium supplemented with 10% fetal bovine serum (FBS) and 10 µg/mL ciprofloxacin in a humidified atmosphere of 5% CO₂ and 95% air at 37 °C.

2.9. Cytotoxicity assay

JC cancer cells were seeded in a 96-well plate (3000–3500 cells per well in 100 µL RPMI medium) and incubated overnight. The next day, 100 µL of gold nanoparticles in PBS pH 7.4 supplemented with 10 mM D-glucose were added to the cells at two concentrations and incubated for 48 h. Final gold concentrations after addition to cells were 0.025 g/L and 0.013 g/L (spherical particles) 0.010 g/L and 0.005 g/L (multi-spiked particles). Cell viability was assessed by a colorimetric reagent (CellTiter 96 AQueous One Solution Assay, Promega), which was added to cells for one hour followed by the measurement of absorbance at 490 nm by an iMark Microplate Absorbance Reader (Bio-Rad Laboratories, Inc.). The absorbance readings were corrected for the absorbance of gold nanoparticles at 490 nm. All samples were prepared in triplicate.

2.10. Cellular uptake of gold nanoparticles

Various amounts of JC cancer cells (from 100,000 to 1 million cells in different experiments) were treated in suspension with purified spherical gold nanoparticles (0.83% citrate and 10% pHLIP-90% PEG) (typically the final concentration of gold with cells was 0.06 g/L) for three hours at 37 °C in serum-free Leibovitz's L-15 medium of pH 6.0 or pH 7.4 (final treatment volume was 500 µL). In another experiment, JC cells were pre-treated with gold nanoparticles in serum-free L-15 medium at pH 7.4 for 20 min, and then media (with different pHs) were added to set a total volume of 500 µL and a final solution pH of 7.4 or 6.0–6.2. After treatment, samples were pelleted (5 min at 600 RCF) and washed with PBS, pH 7.4, three times. The amount of gold in each pellet was then quantified using ICP-MS. The amount of gold not taken up by cells was quantified in the supernatant by absorbance measurements. Control samples of gold nanoparticles without cells and cells without particles were investigated at both high and low pH as well. All samples were prepared in triplicate.

2.11. Uptake and distribution of gold in tumors

All animal studies were conducted according to the animal protocol AN07-01-015 approved by the Institutional Animal Care and Use Committee at the University of Rhode Island, in compliance with the principles and procedures outlined in the National Institutes of Health Guide for the Care and Use of Animals. Female Balb/C mice ranging in age from 4 to 6 weeks and weighing from 18 to 22 g were obtained from Envigo RMS, Inc; 16 mice were used in the study. Tumors were established in the right flank by subcutaneous injection of JC cancer cells (10⁶ cells in 100 µL). After about two weeks, 50 µL of 0.11 g/L of purified spherical gold nanoparticles

(0.83% citrate and 10% pHLIP-90% PEG) (5.5 μ g of gold), or 0.42 g/L gold particles (21 μ g of gold) in PBS, pH 7.4, supplemented with 10 mM D-glucose were injected intratumorally. An hour after injection, mice were euthanized and the tumors were immediately collected for histological and gold-quantification analysis. The amount of gold in each tumor was quantified using ICP-MS. A non-injected mouse with a similar-sized tumor was used as a negative control. The distribution of gold within the tumor was assessed by white light imaging of the tumor center.

2.12. Histological staining and imaging of tumor sections

Immediately after tumors were collected from the mice, they were frozen in tissue-tek OCT compound using liquid nitrogen and stored at -80 °C until sectioned at a thickness of 20 μ m using a cryostat at -25 °C (Vibratome UltraPro5000, GMI). Tumor sections were then fixed in a 4% paraformaldehyde solution (Sigma-Aldrich Co.), washed three times with deionized water, permeated with 0.3% Triton X-100 (Sigma-Aldrich, Co.) in PBS, pH 7.4, for one hour, washed two times with deionized water, and stained with HQ Silver™ silver enhancement solution (Nanoprobes, Inc) for 15 min followed by a final washing. The tumor sections were finally stained with 3 μ M 4',6-diamidino-2-phenyl-indole (DAPI) (Molecular Probes, Thermo Fisher Scientific) for two and a half hours to mark cell nuclei. Adjacent tumor slides were fixed in 4% formaldehyde and stained with hematoxylin and eosin (H & E) (Thermo Fisher Scientific and Poly Scientific R & D Corp). The stained section was covered with a drop of mounting medium (Permount®, Fisher Scientific) and then a cover slide was placed over the medium. The slides were examined under an inverted fluorescence microscope (IX71 Olympus).

Results

We have synthesized and investigated pHLIP® and PEG coated gold nanoparticles. In our study we used WT pHLIP® peptide (4.1 kDa) with a single Cys residue at the N-terminus and similar size of PEG polymer (about 5 kDa) with a single SH group. The pHLIP® and PEG were used in a mixture with reducing agents, tri-sodium citrate or ascorbic acid, to prepare spherical or spiked gold nanoparticles, respectively. The pHLIP® peptide was dissolved in a solution of 2.7 M urea and mixed (in equal parts) with degassed, deionized water containing a ten times molar-excess of TCEP, which prevents the formation of disulfide bonds. The PEG polymer was dissolved in degassed, deionized water containing a ten times molar-excess of TCEP.

3.1. Synthesis and characterization of spherical pHLIP® and PEG coated gold nanoparticles

To obtain pHLIP® and PEG coated spherical gold nanoparticles, the solution of gold III chloride was reduced using tri-sodium citrate mixed with pHLIP® peptide and PEG polymer. The solution containing gold III chloride, citrate, pHLIP®, and PEG was blown with argon and sealed for incubation at room temperature. Within 15–20 min a change in color of the solution was observed (Supplementary Fig. S1) and particles were left overnight at room temperature to ensure the complete reduction of the gold and coating of nanoparticles by pHLIP® and PEG. Interesting to note that presence of pHLIP® slows down time of gold reduction.

In the course of this study we varied the amount of citrate, pHLIP®, and PEG, and monitored the changes of nanoparticles size and absorbance of the nanoparticles solution for the appearance of a resonance peak at 525 nm (Fig. 1). The absence of pHLIP® and PEG leads to the aggregation of particles and precipitation within a couple of hours after their preparation (Supplementary Fig. S1 and Fig. 1a). The higher amount of citrate is expected to promote better stability of nanoparticles. However, our goal was an investigation of formation of gold nanoparticles in the presence of pHLIP® and PEG, which were found to enhance stability and solubility of nanoparticles. The best resonance was observed when gold nanoparticles were coated with both pHLIP® and PEG. The amount of sodium citrate was varied from 0.42% to 2.8% wt/vol in the presence of 10% pHLIP® and 90% PEG in solution, where the concentration of citrate is reported as a final concentration in the nanoparticle solution (Fig. 1b). A low amount of citrate (0.42% wt/vol) in solution results in the shift and broadening of the resonance peak, as well as the appearance of large particles, which was confirmed by the nanoparticle tracking system (data not shown). At the same time, particle sizes did not change when the amount of citrate was varied from 0.83% wt/vol to 2.8% wt/vol. The best results (narrow resonance) were obtained for citrate concentrations in the range between 0.83% wt/vol and 1.7% wt/vol. There is a possibility that at high amount of citrate (2.8% wt/vol) in the presence of pHLIP® and PEG, the shape of particles might be altered, which leads to the broadening and shift of a resonance.

The amount of pHLIP® peptide and PEG polymer was altered as well. An increased percentage of negatively charged pHLIP®, which slows down process of gold reduction, and decreased percentage of neutral PEG polymer leads to the broadening of resonance and shift (by 6–8 nm) of resonance to longer wavelengths (Fig. 1c). The

minimum amount of citrate (0.83% wt/vol), 10% pHLIP® and 90% PEG were chosen as an optimal, when resonance is narrow and there are enough pHLIP® peptides deposited to the surface of nanoparticles to preserve pH-dependent interaction of the coated nanoparticles with the lipid bilayer of a membrane. The final selected composition of reagents (0.83% citrate and 10% pHLIP-90% PEG) comprised the following molar parts: 0.5 parts of 10 mM gold III chloride; 0.075 parts of tri- sodium citrate (10% wt/vol); 0.1125 parts of 0.5 mM PEG with 5 mM T CEP; 0.0125 parts 0.5 mM pHLIP® peptide with 5 mM TCEP and 1.35 M urea, and 0.3 parts of degassed deionized water.

After synthesis, the solution of nanoparticles was purified to remove large particles and excess reducing agents. The large particles were removed by centrifugation. The excess reducing agents were removed when the nanoparticles were transferred to PBS, pH 7.4 solution by size-exclusion chromatography. TEM imaging was employed to analyze nanoparticle size and shape distributions (Fig. 1e). The nanoparticles were homogeneous and round. The metallic core was about 7.0 ± 2.5 nm in diameter (Supplementary Fig. S2a). The mean hydrodynamic size (diameter), determined by nanoparticle tracking system, was about 43 nm.

Purified spherical gold nanoparticles coated with pHLIP® and PEG (0.83% citrate and 10% pHLIP-90% PEG) were stable for at least 36 days at 4 °C in PBS, pH 7.4. The stability of gold nanoparticles in solution was assessed by visual appearance of precipitate, measurements of nanoparticle size and resonance peak by absorbance recording. The stability study was carried out on the particles at two different concentrations with gold amount of 0.10 g/L and 0.02 g/L. A high stability profile was obtained for both concentrations (Fig. 1d). At the same time, when particles were synthesized using a citrate reducing agent (low amount of citrate) containing only

PEG, or without both PEG and pHLIP®, the stability was seriously compromised; particles settled over time forming large visible aggregates and the resonance peak was shifted and broadened (data not shown). Thus, the presence of pHLIP® peptide in gold nanoparticles coating is essential to maintain colloidal stability over time when using the methods described here.

3.2. Templated synthesis and characterization of pHLIP® and PEG coated multispiked gold nanoparticles

Another approach we explored in the preparation of pHLIP® and PEG coated gold nanoparticles was based on use of bicelles as a soft template, to obtain irregularly shaped nanoparticles. Bicelles are disk-like micelles, which consist of long-chain and short-chain phospholipids or surfactants (Fig. 2a). The limitation in experiments using bicelles is typically the high critical micelle concentration (CMC) of lipids and detergents, which restricts the degree of bicelle dilution without the lipid phase transforming to vesicles. For example, the CMC of the widely used short-chain D6PC lipid is 14 mM. Thus, when the best characterized system of D6PC–DMPC bicelles are diluted below CMC, they are expected to be converted into a mixture of free D6PC lipids and DMPC lipid bilayer liposomes. It is known that D7PC lipids have a 10 times lower CMC (1.4 mM), and D7PC–DMPC mixtures retain bicelle properties at concentrations even as low as 0.1% wt/vol [39]. Therefore, we selected the DMPC–D7PC lipid system and ensured that the addition of gold and reducing solutions does not lead to the dilution of lipids below 0.1% wt/vol. Assuming the DMPC and DHPC head groups occupy the same areas, the molar ratio of long-chain to short-chain lipids

is expressed via q -values, which reflects different aspect ratios of disk-like bicelles [40,41]:

$$q = \frac{[\text{DMPC}]}{[\text{DHPC}]} = q = \frac{2\pi R^2}{\pi h (\pi R + h)}$$

where R is the radius and h is the height of the bicelle (Fig. 2a). The height of the bicelles in our study was 4.2 nm and the radius varied depending upon the ratio of DMPC to DHPC lipids. The diameters of the bicelles of different asymmetry, $d(q)$, calculated according to the above equation (without accounting for the DHPC capping) are the following: $d(0.2)=4.2$ nm; $d(0.3)=6.0$ nm; $d(0.5)=8.6$ nm; $d(0.75)=12$ nm; and $d(1.0)=15$ nm. To investigate the integrity of the D7PC-DMPC bicelle structures of various aspect ratios, we monitored their change in size at concentrations of 1.0%, 0.5% and 0.1% wt/vol (Fig. 2b). Because we were only concerned with the change in size upon dilution, no attempts were made to account for asymmetric particle sizes in DLS measurements. A slight increase in size was observed at low concentrations (0.1% wt/vol) for bicelles with q -values less than 0.75. On the other hand, highly asymmetric bicelles with a q -value equal to 1 lose their structural integrity as a result of dilution. Therefore, all experiments were performed with bicelles of q -values of 0.75 and lower.

Templated synthesis of pHLIP® and PEG coated multispiked gold nanoparticles was always initiated shortly after bicelle preparation. We ensured that the addition of gold solution and reducing agents does not lead to the dilution of the bicelle solution to lipid concentrations less than 0.1% wt/vol. The following steps were performed in synthesis of multispiked gold nanoparticles: i) a solution of gold III chloride was added to the solution of bicelles and mixed; ii) next, the reducing agent, ascorbic acid, was added very carefully; and iii) upon color change (~30s) the solution containing pHLIP® and PEG was immediately added to complete the coating process. The appearance of NIR

absorbance (Fig. 3a) along with TEM imaging (Fig. 3b) was indicative of the formation of multispiked gold nanoparticles. In the absence of bicelles, the resonance shifted to 525 nm (Fig. 3a), reflecting the formation of solid spherical gold nanoparticles, which was also confirmed by TEM. Interestingly, the use of citrate as a reducer instead of ascorbic acid shifts the equilibrium towards the formation of solid spherical gold particles rather than the templated synthesis of spiked gold nanoparticles (data not shown). The change of bicelle asymmetry (increase of q-values from 0.3 to 0.75) does not affect appearance of NIR resonance (Fig. 3a). Variation in the amount of gold in the range from 1:0.5 to 1:3 lipid:gold ratios did not significantly affect the appearance of the resonance peak. The normalized absorbance of nanoparticles does not change upon dilution or the addition of a detergent that disrupts lipid structures, Triton X-100, indicating nanoparticle stability and integrity after synthesis (data not shown). The presence of pHLIP® and PEG resulted in the formation of particles that were more stable in aqueous solution compared to the particles without coating, which were precipitated shortly after their preparation. The final composition of the reagents was the following molar parts: 0.05 part of 15 mM of lipids arranged into bicelles (> 0.1% wt/ vol), 0.15 parts of 5 mM gold III chloride; 0.0225 parts of 250 mM ascorbic acid; 0.414 parts of 0.5 mM PEG with 5 mM TCEP; 0.046 parts 0.5 mM pHLIP® peptide with 5 mM TCEP and 1.35 M urea; and 0.3175 parts of degassed, deionized water. TEM imaging performed on filtered pHLIP® and PEG coated gold nanoparticles demonstrated the presence of irregular, multispiked gold nanoparticles (Fig. 3b). The structures were the same for bicelles with different q-values. Conversely, multispiked structures were not observed in absence of bicelles. The mean core size (diameter) of multispiked nanoparticles established by TEM was 146.0 ± 50.4 nm (Supplementary

Fig. S2b). The mean hydrodynamic diameter, determined by nanoparticle tracking system, was about 161 nm.

Different concentrations of pHLIP® and PEG coated multispiked gold nanoparticles were illuminated in solution by an 805 nm laser diode with 500 mW output. The laser radiant exposure was ~400 J/cm². For particles at a concentration of 0.021 g/L gold, a temperature increase of 14 degree units (from 26 °C to 40 °C) was observed within 5 min (Fig. 3c), which is ~18 J imparted to water or ~12% energy converted to heat. More concentrated particles showed greater temperature changes at all time points compared to less concentrated particles.

3.3. Interaction of pHLIP® and PEG coated gold nanoparticles with cancer cells

First, we have tested the cytotoxicity of pHLIP® and PEG coated spherical and multispiked gold nanoparticles. JC murine mammary-gland adenocarcinoma cells were treated with gold nanoparticles (0.025 and 0.013 g/L of spherical; and 0.010 g/L and 0.005 g/L of multispiked) for 48 h. The obtained results indicate that these gold nanoparticles do not exhibit any cellular toxicity.

Next, we evaluated the pH-dependent cellular uptake of spherical gold nanoparticles coated with pHLIP® and PEG. The experiment was performed several times and in different ways, such that the treatment of cells with gold nanoparticles was done at neutral and low pH, or the pre-treatment of cells with gold nanoparticles was done at neutral pH followed by the change of pH with media to low pH. All obtained data indicate that the uptake of spherical gold nanoparticles coated with pHLIP® and PEG by JC cancer cells at pH 6.0 was about 3 times higher than the uptake at neutral pH.

The results confirm the pH-dependent cellular uptake of gold nanoparticles coated with pHLIP® and PEG.

3.4. Distribution of pHLIP® and PEG coated gold nanoparticles within tumors

JC cancer cells were inoculated into the right flank of mice by subcutaneous injection. Spherical gold nanoparticles coated with pHLIP® and PEG were administered as a single intra-tumoral injection at quantities of 5.5 and 21 µg gold. One hour after injection, animals were sacrificed so that tumors could be collected and processed to establish the amount of gold within and the distribution throughout a tumor. Among all of the mice, there were animals with different tumor masses that were separated into 3 groups: 0.1, 0.3 and 0.4 g. The percentage of injected dose accumulated within the tumors increased with the increase of tumor mass: 16.2% for 0.1 g tumor; 18.0% for 0.3 g, and 29.1% for 0.4 g of tumor (Supplementary Fig. S3). The mean tumor uptake of gold (calculated for 8 animals) was 6.8 µg of gold per gram of tumor (with standard error of 1.6) when a total of 5.5 µg of gold was injected. The mean tumor uptake of gold (calculated for 6 animals) was 24.5 µg/g (with standard error of 8.5) when 21 µg of gold was injected. The highest accumulation of gold ~47 µg/g was found in the smallest tumors (85.0 ± 2.3 mg) injected with 21 µg of gold.

We also investigated the distribution of gold within the tumor mass. The white light images were taken from the center of the tumor mass (Fig. 4a). Then, the frozen tumor samples were sectioned and stained with H & E (Fig. 4b). The gold was distributed nearly homogeneously within tumor mass except the right edge of the tumor with no gold accumulation in the surrounding muscle. The muscle tissue adjacent to the tumor is indicated by arrows on Fig. 4a and b, and a magnified image of the border of the

section containing both cancer cells and muscle is shown on Fig 4c. Adjacent sections were treated with Triton to permeabilize the cellular membranes and then stained with both a silver enhancement solution and DAPI. The representative images of the gold enhanced by silver and stained nuclei are shown on Fig 4d-f.

Discussion

The motivation for our work was based on a desire to introduce stable pH-sensitive pHLIP® and PEG coated gold nanoparticles with a potential translation to the clinic. We developed methods for the preparation of spherical and multispiked gold nanoparticles coated with pHLIP® and PEG, which might find application in radiation and NIR thermal therapies. The approach for the synthesis of spherical gold nanoparticles coated with pHLIP® and PEG is very robust and can be implemented in applied studies. The protocol for the preparation of multispiked gold nanoparticles coated with pHLIP® and PEG could be further optimized, however the proof of principle is established in our work. In both cases, pHLIP® peptide and PEG polymer were used as components of the reducing solution (sodium citrate as a reducer in the case of spherical nanoparticles and ascorbic acid in the case of multi- spiked nanoparticles). The optimal combination of pHLIP® and PEG was selected to be 10% and 90%, respectively. A decreased percentage of pHLIP® in the nanoparticle coating might lead to the reduction of particle stability (resulting from the reduction of the overall negative charge due to the presence of pHLIP® peptide on particle surfaces) and the loss of pH-dependent properties. Previously, we investigated and showed the utility of liposomes coated with different quantities of pHLIP® and PEG [30,35]. It is also possible to further optimize particles by employing a pHLIP® PEG conjugate

instead of directly coating the surface with pHLIP®. Spherical gold nanoparticles coated with pHLIP® and PEG exhibited high stability in solution over a one month time period, as opposed to the particles with no coating or just PEG coating. The PEG coating was widely utilized in coating of various nanoparticles [42–46]. The size of the pHLIP® PEG coated particles' metallic core was in the range of 5–8 nm in diameter and the hydrodynamic size (diameter) of coated particles was in the range of 40–50 nm. The nanoparticles showed a pH-dependent uptake by cancer cells with no signs of cytotoxicity. We performed intratumoral injections of spherical gold nanoparticle solutions and investigated gold uptake and distribution within tumors at one hour post-injection. It does not seem that there is any clinical utility to perform a systemic administration of particles, since radiation therapy is typically delivered locally and the location of the tumor is known from prior diagnostic imaging. Also, there is a requirement to have as much gold as possible within a tumor (which could be achieved only by local administration of the particles) to induce a radiation enhancement effect. The radiation delivered within a one hour time frame of particle administration is expected to be in line with clinical practice. Our results indicate that gold nanoparticles (21 µg of injected gold) were distributed within the tumor mass very well and with an overall uptake of 24.5 µg of gold per gram of tumor mass, reaching values of 47 µg/g in tumors with masses of 1 g and less. This is a higher uptake compared to that of pHLIP® gold nanoclusters [37]. We believe, the presence of pHLIP® peptide in the coating of gold nanoparticles was crucial. The peptide allowed particles to stay within the tumor and promoted the uptake of particles by cancer cells at low extracellular pH, as we have shown previously [37,38]. At the same time, particles were able to diffuse within a tumor as opposed to the direct injection of micron-sized gold particles, that hinder tumor coverage by staying only at the injection

site [3]. We also would like to outline that systemic administration of nanoparticles or antibodies conjugated with gold nanoparticles results in staining of only the peripheral tumor regions with limited penetration inside the tumor mass [47]. We did not observe an accumulation of gold within the muscle tissue adjacent to the tumors. The amount of injected gold in our study was much less than the amount of gold used in previous radiation therapy studies on mice (see review and references within it) [48]. However, we believe that the targeting of gold nanoparticles directed by pHLIP® peptide to the vital cellular structures such as plasma and nuclear membranes could lead to the enhancement of radiation effects even at lower gold concentrations [38].

The spherical particles have the smallest surface to volume ratio for a given size of a particle. The appearance of multiple sharp spikes or tips on the surface of nanoparticle is known to give rise to the strong spatial confinement of the electromagnetic field, since the core of a particle serves as a nanoscale antenna, increasing the excitation cross section and the enhancement of the tip plasmon polaritons [49,50]. Various approaches were introduced in the synthesis of star-like and multispiked gold nanoparticles [50–53]. We used a soft template material of phospholipid bicelles to synthesize pHLIP® and PEG coated multispiked gold nanoparticles. Bicelles, which possess both low- and high- curvature regions within a bilayer disks, represent a class of model membranes used in nuclear magnetic resonance (NMR) structural studies of membrane biomolecules [41,54–56], but they have found additional applications in biomedical sciences [57–59]. The bicellar templates were utilized previously to control the growth of platinum with ascorbic acid as a reducer, producing metal nanodisks and nanowheels [60,61]. Other phospholipid structures, like spherical liposomes, were also used for gold deposition to assemble biodegradable plasmon resonant nanoshells, which were used for the laser-induced release of molecules encapsulated into these

liposomes [62–64]. Another approach was based on the assembly of liposomes and micelles, called metallosomes, by using lipids conjugated with gold nanoclusters [65]. The presence of a soft template, like bicelles, in our reduction mixture induced the formation of multispiked gold nanoparticles with plasmon resonance in the NIR range. The absence of bicelles leads to the formation of spherical gold nanoparticles with absorbance at 525–560 nm. The size of gold multispiked nanoparticles established by TEM imaging and nanoparticle tracking system was in the range of 100–170 nm and 130–200 nm, respectively. The heating of pHLIP® and PEG coated multispiked gold nanoparticles in solution by an 805 nm laser diode led to the increase of the solution temperature by 14 degrees within 5 min. Multispiked particles could be used in combination with NIR laser treatment for photo-induced hyperthermia. It would be very advantageous to employ lower power NIR laser radiation systems, which are currently available for indocyanine green (ICG) imaging in clinical endoscopy and laparoscopy (see table 4 for the description of ICG clinical imaging systems in the review article) [66]. Also, due to the very high surface area of multispiked gold nanoparticles, we envision their potential successful application for the enhancement of x-ray radiation effects. A number of binary radiation therapies are under consideration [2,67–69]. At low photon energies, the most promising approach is based on dose enhancement through Auger electron emission. Auger electron emission generates a cascade of low energy electrons that travel short distances and deposit their energy locally [70]. Thus, it is very important to deliver gold nanoparticles to vital cellular structures, which pHLIP® helps achieve. Also, it was proposed that a potential advantage of the use of small gold nanoparticles (with an enhanced surface/volume ratio) is the minimization of the energy of the Auger electrons deposited (lost) inside

the gold nanoparticle [38,70]. Therefore, it could be very attractive to test multispiked gold nanoparticles with large surface/volume ratios as radiation enhancers.

Author contributions

JL Daniels, OA Andreev, and YK Reshetnyak designed the research; JL Daniels and TM Crawford performed the research; JL Daniels, TM Crawford, and YK Reshetnyak analyzed the data; JL Daniels and YK Reshetnyak wrote the paper.

Conflict of interest

OA Andreev and YK Reshetnyak have founded and have a financial interest in a company, pHLIP, Inc., with the aim of bringing pHLIP® technology to the clinic. The company has had no involvement in funding the studies reported here.

Acknowledgment

We are grateful to Renato Guerrieri for his assistance in preliminary experiments in the preparation of multispiked gold nanoparticles. We would like to thank Dr. Al Bach and Kim Andrews, Rhode Island IDeA Network for Excellence in Biomedical Research (INBRE), as well as Dr. Katherine Kelley, University of Rhode Island, the Graduate School of Oceanography, for their assistance in ICP-MS analysis of samples; Dr. Richard Kingsley and Dr. Iftheker Khan, University of Rhode Island, for performing TEM imaging; Dr. Anna Moshnikova, University of Rhode Island, for her assistance with studies on cultured cells; and Dr. Michael Anderson, University of

Massachusetts Boston, for his discussions concerning heating experiments. This work was supported by the General Medical Sciences of the National Institutes of Health grant R01GM073857 to OAA and YKR. Also, this research was supported in part by an Institutional Development Award (IDeA) Network for Biomedical Research Excellence from the National Institute of General Medical Sciences of the National Institutes of Health under grant number P20GM103430.

Appendix A. Transparency document

Transparency document associated with this article can be found in the online version at doi:10.1016/j.bbrep.2017.02.008.

References

- [1] J.F. Hainfeld, F.A. Dilmanian, D.N. Slatkin, H.M. Smilowitz, Radiotherapy enhancement with gold nanoparticles, *J. Pharm. Pharm.* 60 (8) (2008) 977–985.
- [2] J.F. Hainfeld, D.N. Slatkin, H.M. Smilowitz, The use of gold nanoparticles to enhance radiotherapy in mice, *Phys. Med. Biol.* 49 (18) (2004) N309–315.
- [3] D.M. Herold, I.J. Das, C.C. Stobbe, R.V. Iyer, J.D. Chapman, Gold microspheres: a selective technique for producing biologically effective dose enhancement, *Int. J. Radiat. Biol.* 76 (10) (2000) 1357–1364.
- [4] P. Retif, S. Pinel, M. Toussaint, et al., Nanoparticles for radiation therapy enhancement: the key parameters, *Theranostics* 5 (9) (2015) 1030–1044.

- [5] D.P. O'Neal, L.R. Hirsch, N.J. Halas, J.D. Payne, J.L. West, Photo-thermal tumor ablation in mice using near infrared-absorbing nanoparticles, *Cancer Lett.* 209 (2) (2004) 171–176.
- [6] G. von Maltzahn, J.H. Park, A. Agrawal, et al., Computationally guided photo-thermal tumor therapy using long-circulating gold nanorod antennas, *Cancer Res.* 69 (9) (2009) 3892–3900.
- [7] E.B. Dickerson, E.C. Dreaden, X. Huang, et al., Gold nanorod assisted near-infrared plasmonic photothermal therapy (PPTT) of squamous cell carcinoma in mice, *Cancer Lett.* 269 (1) (2008) 57–66.
- [8] C. Xu, S. Sun, Superparamagnetic nanoparticles as targeted probes for diagnostic and therapeutic applications, *Dalton Trans.* 29 (2009) 5583–5591.
- [9] R.A. Bohara, N.D. Thorat, S.H. Pawar, Role of functionalization: strategies to explore potential nano-bio applications of magnetic nanoparticles, *RSC Adv.* 6 (2016) 43989–44012.
- [10] N.D. Thorat, R.A. Bohara, S.A. Tofail, et al., Superparamagnetic gadolinium ferrite nanoparticles with controllable curie temperature—cancer theranostics for mr- imaging-guided magneto-chemotherapy, *Eur. J. Inorg. Chem.* (2016) 4586–4597.
- [11] R.A. Bohara, N.D. Thorat, H.M. Yadav, S.H. Pawar, One-step synthesis of uniform and biocompatible amine functionalized cobalt ferrite nanoparticles: a potential carrier for biomedical applications, *New J. Chem.* 38 (2014) 2979–2986.
- [12] D. Ho, X. Sun, S. Sun, Monodisperse magnetic nanoparticles for theranostic applications, *Acc. Chem. Res.* 44 (10) (2011) 875–882.
- [13] L.M. Lacroix, D. Ho, S. Sun, Magnetic nanoparticles as both imaging probes and therapeutic agents, *Curr. Top. Med Chem.* 10 (12) (2010) 1184–1197.

- [14] P.R. Srinivas, B.S. Kramer, S. Srivastava, Trends in biomarker research for cancer detection, *Lancet Oncol.* 2 (11) (2001) 698–704.
- [15] J.P. Janssens, I. Verlinden, N. Gungor, J. Raus, L. Michiels, Protein biomarkers for breast cancer prevention, *Eur. J. Cancer Prev.* 13 (4) (2004) 307–317.
- [16] J.H. Hanke, K.R. Webster, L.V. Ronco, Protein biomarkers and drug design for cancer treatments, *Eur. J. Cancer Prev.* 13 (4) (2004) 297–305.
- [17] S.J. Goldsmith, Receptor imaging: competitive or complementary to antibody imaging? *Semin Nucl. Med.* 27 (2) (1997) 85–93.
- [18] B. Freemark, D. Clark, F. Pernasetti, et al., Targeting of humanized antibody D93 to sites of angiogenesis and tumor growth by binding to multiple epitopes on denatured collagens, *Mol. Immunol.* 44 (15) (2007) 3741–3750.
- [19] L.E. Gerweck, K. Seetharaman, Cellular pH gradient in tumor versus normal tissue: potential exploitation for the treatment of cancer, *Cancer Res.* 56 (6) (1996) 1194–1198.
- [20] N. Raghunand, M.I. Altbach, R. van Sluis, et al., Plasmalemmal pH-gradients in drug-sensitive and drug-resistant MCF-7 human breast carcinoma xenografts measured by ³¹P magnetic resonance spectroscopy, *Biochem. Pharmacol.* 57 (3) (1999) 309–312.
- [21] D. Weerakkody, A. Moshnikova, M.S. Thakur, et al., Family of pH (low) insertion peptides for tumor targeting, *Proc. Natl. Acad. Sci. USA* 110 (15) (2013) 5834–5839.
- [22] O.A. Andreev, D.M. Engelman, Y.K. Reshetnyak, Targeting diseased tissues by pHLIP insertion at low cell surface pH, *Front. Physiol.* 5 (2014) 97.

- [23] Y.K. Reshetnyak, O.A. Andreev, U. Lehnert, D.M. Engelman, Translocation of molecules into cells by pH-dependent insertion of a transmembrane helix, *Proc. Natl. Acad. Sci. USA* 103 (17) (2006) 6460–6465.
- [24] Y.K. Reshetnyak, M. Segala, O.A. Andreev, D.M. Engelman, A monomeric membrane peptide that lives in three worlds: in solution, attached to, and inserted across lipid bilayers, *Biophys. J.* 93 (7) (2007) 2363–2372.
- [25] O.A. Andreev, A.D. Dupuy, M. Segala, et al., Mechanism and uses of a membrane peptide that targets tumors and other acidic tissues in vivo, *Proc. Natl. Acad. Sci. USA* 104 (19) (2007) 7893–7898.
- [26] A.G. Karabadzak, D. Weerakkody, D. Wijesinghe, et al., Modulation of the pHLIP transmembrane helix insertion pathway, *Biophys. J.* 102 (8) (2012) 1846–1855.
- [27] R.C. Adochite, A. Moshnikova, S.D. Carlin, et al., Targeting breast tumors with pH (low) insertion peptides, *Mol. Pharm.* 11 (8) (2014) 2896–2905.
- [28] Z. Cruz-Monserrate, C.L. Roland, D. Deng, et al., Targeting pancreatic ductal adenocarcinoma acidic microenvironment, *Sci. Rep.* 4 (2014) 4410.
- [29] A.G. Karabadzak, M. An, L. Yao, et al., pHLIP-FIRE, a cell insertion-triggered fluorescent probe for imaging tumors demonstrates targeted cargo delivery in vivo, *ACS Chem. Biol.* 9 (11) (2014) 2545–2553.
- [30] L. Yao, J. Daniels, D. Wijesinghe, O.A. Andreev, Y.K. Reshetnyak, pHLIP(R)-mediated delivery of PEGylated liposomes to cancer cells, *J. Control Release* 167 (3) (2013) 228–237.
- [31] F. Emmetiere, C. Irwin, N.T. Viola-Villegas, et al., (18)F-labeled-bioorthogonal liposomes for in vivo targeting, *Bioconjug. Chem.* 24 (11) (2013) 1784–1789.

- [32] L. Han, H. Ma, Y. Guo, Y. Kuang, X. He, C. Jiang, pH-controlled delivery of nanoparticles into tumor cells, *Adv. Health. Mater.* (2013).
- [33] M. Yu, F. Guo, J. Wang, F. Tan, N. Li, A pH-Driven and photoresponsive nanocarrier: remotely-controlled by near-infrared light for stepwise antitumor treatment, *Biomaterials* 79 (2016) 25–35.
- [34] M. Yu, F. Guo, J. Wang, F. Tan, N. Li, Photosensitizer-loaded pH-responsive hollow gold nanospheres for single light-induced photothermal/photodynamic therapy, *ACS Appl Mater. Interfaces* 7 (32) (2015) 17592–17597.
- [35] D. Wijesinghe, M.C. Arachchige, A. Lu, Y.K. Reshetnyak, O.A. Andreev, pH dependent transfer of nano-pores into membrane of cancer cells to induce apoptosis, *Sci. Rep.* 3 (2013) 3560.
- [36] B. Janic, M.P. Bhuiyan, J.R. Ewing, M.M. Ali, pH-dependent cellular internalization of paramagnetic nanoparticle, *ACS Sens.* 1 (8) (2016) 975–978.
- [37] L. Yao, J. Daniels, A. Moshnikova, et al., pHLIP peptide targets nanogold particles to tumors, *Proc. Natl. Acad. Sci. USA* 110 (2) (2013) 465–470.
- [38] M.P. Antosh, D.D. Wijesinghe, S. Shrestha, et al., Enhancement of radiation effect on cancer cells by gold-pHLIP, *Proc. Natl. Acad. Sci. USA* 112 (17) (2015) 5372–5376.
- [39] Z. Lu, W.D. Van Horn, J. Chen, S. Mathew, R. Zent, C.R. Sanders, Bicelles at low concentrations, *Mol. Pharm.* 9 (4) (2012) 752–761.
- [40] P.A. Luchette, T.N. Vetman, R.S. Prosser, et al., Morphology of fast-tumbling bicelles: a small angle neutron scattering and NMR study, *Biochim Biophys. Acta* 1513 (2) (2001) 83–94.
- [41] R.S. Prosser, J.S. Hwang, R.R. Vold, Magnetically aligned phospholipid bilayers

with positive ordering: a new model membrane system, *Biophys. J.* 74 (5) (1998) 2405–2418.

[42] N.D. Thorat, O.M. Lemine, R.A. Bohara, K. Omri, L. El Mir, S.A. Tofail, Superparamagnetic iron oxide nanocargoes for combined cancer thermotherapy and MRI applications, *Phys. Chem. Chem. Phys.* 18 (31) (2016) 21331–21339.

[43] N.D. Thorat, R.A. Bohara, V. Malgras, et al., Multimodal superparamagnetic nanoparticles with unusually enhanced specific absorption rate for synergetic cancer therapeutics and magnetic resonance imaging, *ACS Appl. Mater. Interfaces* 8 (23) (2016) 14656–14664.

[44] J.V. Jokerst, T. Lobovkina, R.N. Zare, S.S. Gambhir, Nanoparticle PEGylation for imaging and therapy, *Nanomed. (Lond.)* 6 (4) (2011) 715–728.

[45] K. Leung, Poly(ethylene glycol)-coated gold nanocages. *Molecular Imaging and Contrast Agent Database (MICAD)*. Bethesda (MD), 2004.

[46] L. Shan, Polyethylene glycol-coated (PEG5000) gold nanoparticles. *Molecular Imaging and Contrast Agent Database (MICAD)*. Bethesda (MD), 2004.

[47] J.F. Hainfeld, M.J. O'Connor, F.A. Dilmanian, D.N. Slatkin, D.J. Adams, H.M. Smilowitz, Micro-CT enables microlocalisation and quantification of Her2-targeted gold nanoparticles within tumour regions, *Br. J. Radiol.* 84 (1002) (2011) 526–533.

[48] S. Shrestha, L.N. Cooper, O.A. Andreev, Y.K. Reshetnyak, M.P. Antosh, Gold nanoparticles for radiation enhancement in vivo, *J. J. Rad. Oncol.* 3 (1) (2016) 026.

[49] F. Hao, C.L. Nehl, J.H. Hafner, P. Nordlander, Plasmon resonances of a gold nanostar, *Nano Lett.* 7 (3) (2007) 729–732.

- [50] D. Melnikau, D. Savateeva, A. Susha, A.L. Rogach, Y.P. Rakovich, Strong plasmon- exciton coupling in a hybrid system of gold nanostars and J-aggregates, *Nanoscale Res Lett.* 8 (1) (2013) 134.
- [51] C.L. Nehl, H. Liao, J.H. Hafner, Optical properties of star-shaped gold nanoparticles, *Nano Lett.* 6 (4) (2006) 683–688.
- [52] T.K. Sau, A.L. Rogach, M. Doblinger, J. Feldmann, One-step high-yield aqueous synthesis of size-tunable multispiked gold nanoparticles, *Small* 7 (15) (2011) 2188–2194.
- [53] L. Shao, A.S. Susha, L.S. Cheung, T.K. Sau, A.L. Rogach, J. Wang, Plasmonic properties of single multispiked gold nanostars: correlating modeling with experiments, *Langmuir* 28 (24) (2012) 8979–8984.
- [54] A.A. De Angelis, S.J. Opella, Bicelle samples for solid-state NMR of membrane proteins, *Nat. Protoc.* 2 (10) (2007) 2332–2338.
- [55] T. Raschle, S. Hiller, M. Etzkorn, G. Wagner, Nonmicellar systems for solution NMR spectroscopy of membrane proteins, *Curr. Opin. Struct. Biol.* 20 (4) (2010) 471–479.
- [56] C.R. Sanders, R.S. Prosser, Bicelles: a model membrane system for all seasons? *Structure* 6 (10) (1998) 1227–1234.
- [57] G. Rodriguez, G. Soria, E. Coll, et al., Bicosomes: bicelles in dilute systems, *Biophys. J.* 99 (2) (2010) 480–488.
- [58] L. Barbosa-Barros, G. Rodriguez, C. Barba, et al., Bicelles: lipid nanostructured platforms with potential dermal applications, *Small* 8 (6) (2012) 807–818.
- [59] L. Barbosa-Barros, A. de la Maza, J. Estelrich, et al., Penetration and growth of DPPC/DHPC bicelles inside the stratum corneum of the skin, *Langmuir* 24 (11) (2008) 5700–5706.

- [60] Y. Song, R.M. Dorin, R.M. Garcia, et al., Synthesis of platinum nanowheels using a bicellar template, *J. Am. Chem. Soc.* 130 (38) (2008) 12602–12603.
- [61] R.M. Garcia, Y. Song, R.M. Dorin, et al., Templated growth of platinum nanowheels using the inhomogeneous reaction environment of bicelles, *Phys. Chem. Chem. Phys.* 13 (11) (2011) 4846–4852.
- [62] T.S. Troutman, J.K. Barton, M. Romanowski, Biodegradable plasmon resonant nanoshells, *Adv. Mater.* 20 (13) (2008) 2604–2608.
- [63] S.J. Leung, M. Romanowski, NIR-activated content release from plasmon resonant liposomes for probing single-cell responses, *ACS Nano* 6 (11) (2012) 9383–9391.
- [64] S.J. Leung, M. Romanowski, Light-activated content release from liposomes, *Theranostics* 2 (10) (2012) 1020–1036.
- [65] J.F. Hainfeld, F.R. Furuya, R.D. Powell, Metallosomes, *J. Struct. Biol.* 127 (2) (1999) 152–160.
- [66] J.T. Alander, I. Kaartinen, A. Laakso, et al., A review of indocyanine green fluorescent imaging in surgery, *Int. J. Biomed. Imaging* 2012 (2012) 940585.
- [67] K.N. Morris, M.D. Weil, R. Malzbender, Radiochromic film dosimetry of contrast-enhanced radiotherapy (CERT), *Phys. Med. Biol.* 51 (22) (2006) 5915–5925.
- [68] A. Norman, M. Ingram, R.G. Skillen, D.B. Freshwater, K.S. Iwamoto, T. Solberg, X-ray phototherapy for canine brain masses, *Radiat. Oncol. Invest.* 5 (1) (1997) 8–14.
- [69] G. Tisljar-Lentulis, L.E. Feinendegen, V.P. Bond, Biological radiation effects of inclusion of moderately heavy nuclei into the tissue and use of soft roentgen rays, *Strahlentherapie* 145 (6) (1973) 656–662.

[70] S.J. McMahon, W.B. Hyland, M.F. Muir, et al., Biological consequences of nanoscale energy deposition near irradiated heavy atom nanoparticles, *Sci. Rep.* 1 (2011) 18.

Figures

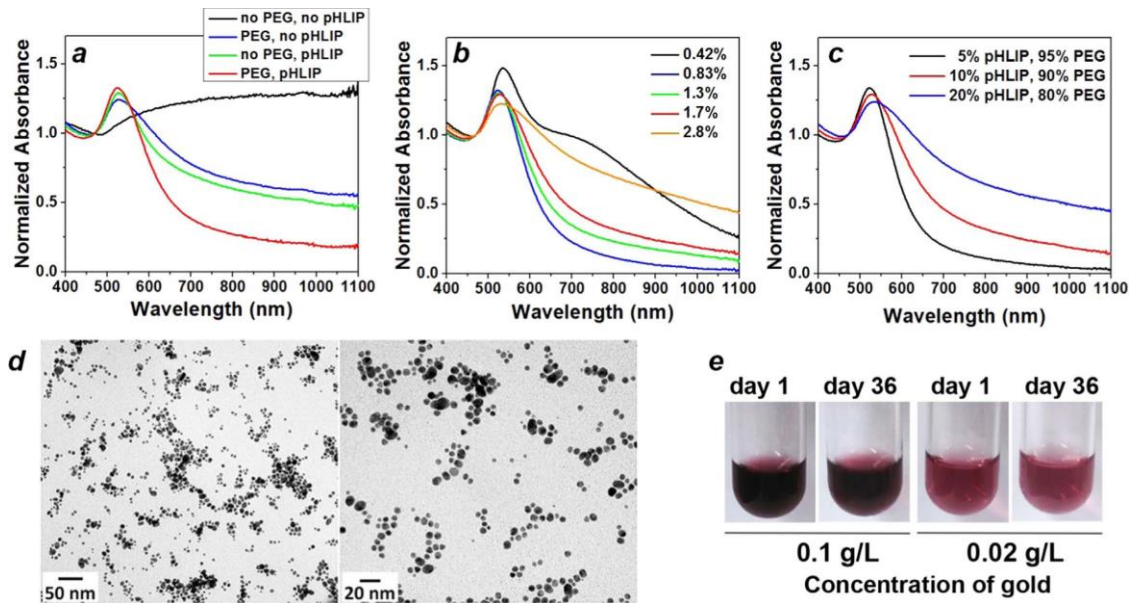


Figure 1. Characterization of Spherical Gold Nanoparticles. The absorbance spectra of the spherical gold nanoparticle solutions synthesized a) in the absence and presence of pHLIP® peptide and/or PEG polymer or mixture of 10% pHLIP® and 90% PEG (1.7% wt/vol citrate); b) with various amounts of sodium citrate, where the percentage of citrate is reported as the final wt/ vol concentration (10% pHLIP® and 90% PEG); c) with various amounts of pHLIP® and PEG (0.83% wt/vol citrate). d) The representative TEM images of pHLIP® and PEG coated spherical gold nanoparticles obtained at 20,000× and 40,000x magnifications (0.83% wt/vol citrate and 10% pHLIP®–90% PEG). The size histograms of the metallic core of pHLIP® and PEG coated nanoparticles is shown in Supplementary Fig. S2a. e) White light images of particles at the beginning and end of stability studies (0.83% wt/vol citrate and 10% pHLIP®–90% PEG, particles were purified and kept at 4 °C in PBS, pH 7.4).

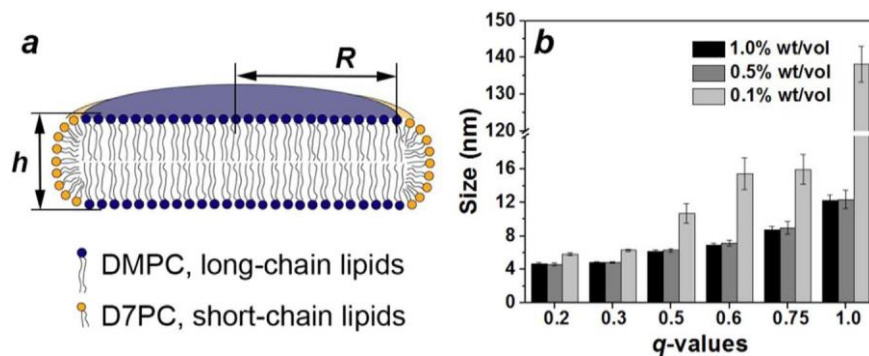


Figure 2. Structure of bicelles. a) The disk-like shape of a bicelle with height, h , and radius, R , composed of DMPC and DHPC lipids. b) Dependence of bicelle size, established by DLS, on its q -value, which is a ratio of long- to short-chain lipids (reflecting the asymmetry of a bicelle).

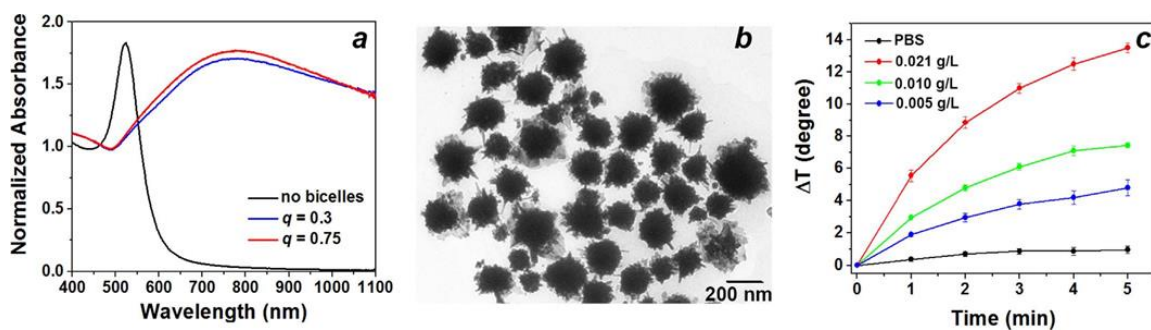


Figure 3. Characterization of Multispiked Gold Nanoparticles. a) The absorbance spectra of gold nanoparticles obtained by gold reduced with ascorbic acid, pHLIP®, and PEG in the absence and presence of bicelles of different asymmetries. b) The representative TEM image of pHLIP® and PEG coated multispiked gold nanoparticles obtained at 12,000× magnification. The size histograms of the metallic core of pHLIP® and PEG coated nanoparticles is shown in Supplementary Fig. S2b. c) The change in temperature over time measured in solutions containing pHLIP® and PEG coated spiked gold nanoparticles of different concentrations irradiated by an 805 nm laser.

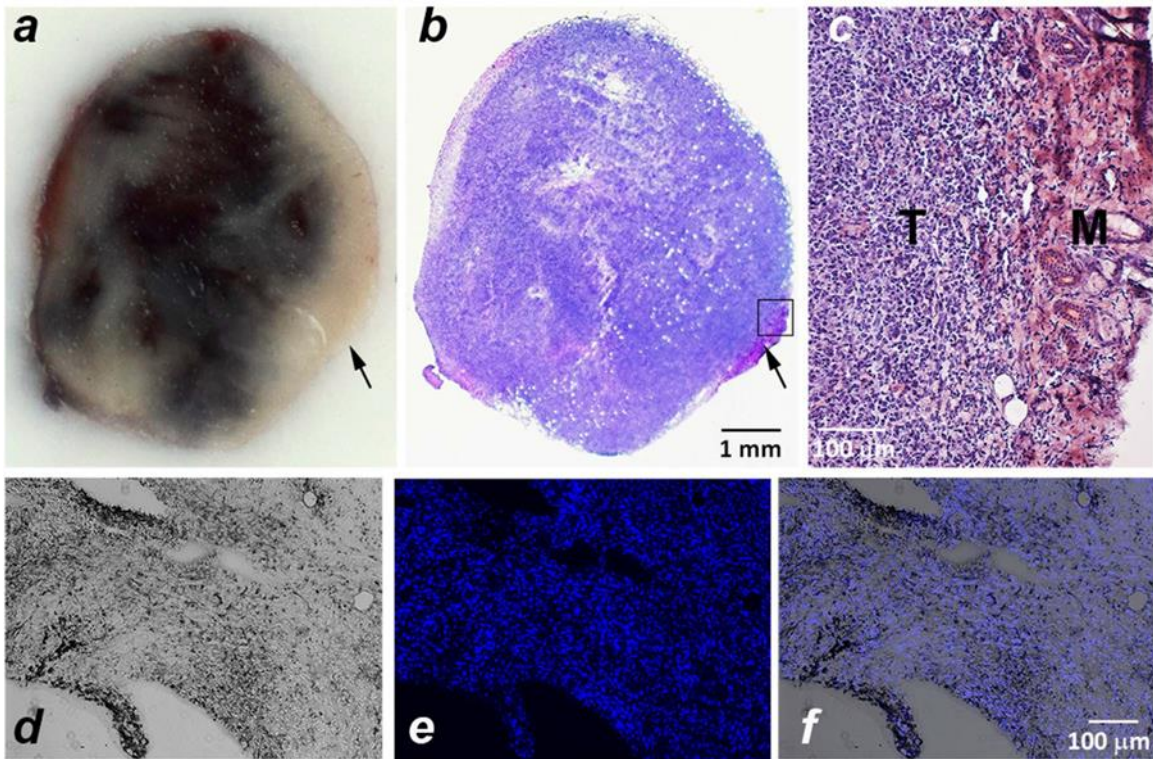


Figure 4. Tumor Imaging of Spherical Gold Nanoparticle Uptake. a) The white light image of a tumor center showing the gold distribution (after a 21 μg intratumoral injection of pHLIP[®] and PEG coated spherical gold nanoparticles in PBS, pH7.4); b) the section from the tumor center stained with H & E; and c) the magnified image of the tumor section outlined by a square in panel b, which shows tumor (T) and muscle (M). The arrows on panels a and b indicate muscle tissue. d) The bright field image of tumor sections stained with silver enhancement solution and e) the fluorescent image of the same tumor section stained with DAPI to visualize cell nuclei; and f) an overlay of the bright filed and fluorescent images. The percentage of injected dose of gold accumulated within tumors of different masses is given in the text and in Supplementary Fig. S3.

CHAPTER 3

ICG-pHLIP for delineation of tumors and blood flow during fluorescence-guided surgery

Prepared for Publication in Nature Biomedical Engineering

Troy Crawford^{1,*}, Anna Moshnikova^{1,*}, Sean Roles¹, Dhammika Weerakkody¹, Michael DuPont¹, Lukas M. Carter², John Shen³, Donald M. Engelman⁴, Jason S. Lewis², Oleg A. Andreev¹, Yana K. Reshetnyak¹

¹Physics Department, University of Rhode Island, Kingston, RI

²Department of Radiology and Program in Molecular Pharmacology, Memorial Sloan Kettering Cancer Center, New York, NY

³Stryker Endoscopy Corp., 5900 Optical Ct, San Jose, CA 95138

⁴Department of Molecular Biophysics and Biochemistry, Yale, New Haven, CT

*Authors contributed equally.

ABSTRACT

Fluorescence imaging has seen enduring use in imaging blood flow and is now finding a new range of applications in image-guided surgery. In this paper, we report our studies of a new fluorescent agent for use in surgery, ICG-pHLIP. Intravenously administered ICG-pHLIP exhibits a multi-hour circulation half-life, offering protracted delineation of vasculature. Concomitant with blood clearance, ICG-pHLIP binds to cells in acidic tissues, such as tumors, by sensing cell surface acidity. Accumulation in tumors marks them for surgical removal or other treatments. We present the results of preclinical studies, including *in vitro* and *in vivo* efficacy, pharmacology and toxicology investigations. It is found that ICG-pHLIP is non-toxic, marks blood flow for hours after injection, and effectively marks tumors for improved resection one day after administration.

In this paper, we explore applications of a new fluorescent agent for use in surgery, ICG-pHLIP. Fluorescence imaging has long had applications in imaging blood flow and is now finding a new range of applications in image-guided surgery. For decades, fluorescence angiography has been applied to assess blood flow and tissue perfusion in preoperative, intraoperative and postoperative settings¹⁻⁸. Emerging uses in fluorescence-guided surgery promise to improve surgical outcomes by revealing tumor margins and, even more importantly, by marking flat lesions and micro-metastases adjacent to primary tumors, which are difficult to identify even by a very skilled surgeon⁹⁻¹².

Several FDA approved fluorescent dyes and compounds are now in clinical use. 5-Aminolevulinic acid (5-ALA) and its derivatives are heme precursors that induce production and intracellular accumulation of a fluorescent protoporphyrin. These dyes are used intraoperatively to identify brain tumors such as malignant gliomas^{13,14} and

for fluorescent visualization of cancerous lesions in the bladder using blue light cystoscopy after topical application of the agent by intravesical instillation¹⁵⁻¹⁸. The most widely used dye is the near infrared (NIR) emitting indocyanine green (ICG), first approved for angiography and subsequently used in ophthalmology and elsewhere for imaging blood vessels¹⁹⁻²⁴. In addition to clinically approved fluorescent molecules, several approaches are under development (in preclinical and clinical trial stages) for targeting and visualization of cancerous lesions intra- or post-operatively. We have introduced a novel imaging agent, ICG-pHLIP, for the visualization of cancerous lesions and blood flow during fluorescence-guided surgical procedures. A pH-Low Insertion Peptide (pHLIPs^{®1}) senses elevated acidity at the surfaces of tumor cells (or low surface pH, pH_{surf})²⁵⁻²⁷. Low pH promotes protonation of Asp/Glu residues within pHLIP, increasing the peptide's hydrophobicity and triggering the peptide to form a stable helix across the membrane. By attachment to the N terminal end of the peptide, which remains outside the cell, imaging probes can be tethered to the surfaces of cells to mark tumors. Examples include PET or SPECT nuclear probes, MR agents and fluorescence emitters. pHLIP offers a unique approach in the targeting of a spectrum of tumor subtypes, as acidosis is a fundamental feature of the tumor microenvironment^{28,29}, and it has been found that pHLIP peptides conjugated with various fluorescent dyes target tumors with high precision³⁰. ICG coupled to pHLIP was chosen as a clinical candidate for two main reasons. The fluorescence of ICG-pHLIP is enhanced about 20 times when pHLIP tethers ICG to the membrane compared to the emission of ICG-pHLIP in aqueous solution, thus significantly enhancing the tumor-to-background ratio³¹. Also, many clinical instruments for imaging of ICG fluorescence have already been developed and are clinically available,

¹ pHLIP[®] is a registered trademark owned by the Rhode Island Board of Education

which potentially makes the adoption of ICG-pHLIP in the clinic a straightforward process. Here we present the results of preclinical studies, including *in vitro* and *in vivo* efficacy, pharmacology and toxicology investigations.

RESULTS

ICG-pHLIP Synthesis and Characterization

The 28-amino acid pHLIP Var3 peptide with free N- and C-terminus was synthesized on solid support followed by purification and conjugation of a single Cys residue with ICG-maleimide to obtain the ICG-pHLIP imaging agent (Figure 1a, Supplementary Figure S1a). Further optimization of the ICG-pHLIP manufacturing protocol has been completed by CordenPharma, and GMP manufacturing is in progress. ICG-pHLIP reconstituted in PBS was found to be stable in solution for 4 days at room temperature. The molar attenuation coefficient (i.e. extinction coefficient) of ICG-pHLIP at 810 nm measured in methanol (Supplementary Figure S2a) was determined as $152,533 \text{ M}^{-1}\text{cm}^{-1}$ and used to calculate the concentration of ICG-pHLIP. The absorption and emission spectra of ICG-pHLIP in DMF (to mimic the hydrophobic environment of the membrane) are shown in Figure 1b. It is important to note that spectral signals of ICG-pHLIP do not overlap with the absorption or emission of Methylene Blue and Isosulfan Blue, dyes which are widely used for tissue staining during surgery and for histological analysis (Supplementary Figure S2b-f). The interaction of ICG-pHLIP with membrane lipid bilayers was studied using POPC liposomes. ICG-pHLIP exhibits pHLIP-like pH-dependent interactions with cell membranes monitored by changes of the peptide circular dichroism and the fluorescence emission of tryptophan residues (Figure 1c-e). The midpoint of the transition for ICG-pHLIP insertion in liposomes is at pH 6.3, meaning ~70% of ICG-pHLIP is expected to be inserted across cancer cell

membranes with a cell surface pH_{surf} of 6.0 at equilibrium, while at the normal cell surfaces (pH 7.4) only <1% of ICG-pHLIP molecules might insert into membrane. Since the rate constant of ICG-pHLIP insertion into membrane is high (approximately 5 sec^{-1}) the insertion will occur even under conditions of fast blood flow and limited exposure time of ICG-pHLIP to acidic cancer cells.

Safety Studies In vitro

The cytotoxicity of ICG-pHLIP was assessed by treatment of human mammary epithelial cells (HMEpC) with increasing concentrations of ICG-pHLIP (up to $16 \mu\text{M}$) for 72 hours, followed by assessment of cell viability. ICG-pHLIP did not show any cytotoxic effect at any tested concentration.

ICG-pHLIP interactions with components of the blood were investigated. It was established that >99.9% of ICG-pHLIP is bound at equilibrium in human, mouse, rat, minipig, dog and cynomolgus monkey blood, and that the amount of ICG-pHLIP bound to plasma proteins varies from 95.3% (mouse) to 99.9% (humans) (Supplementary Table S2). Hemolysis of red blood cells (RBCs) was followed with increasing concentrations of ICG-pHLIP (up to 1.2 nmol), and lysis was assessed by the release of hemoglobin. The amount of RBC lysis was less than 2% in all samples. The rate of ICG-pHLIP hepatic clearance monitored using human, rat, dog, minipig and cynomolgus monkey hepatocytes was very similar, and varied from 20-28 $\mu\text{L}/\text{min}/10^6$ cells. The hepatic clearance established in the mouse hepatocytes, which are larger in size, was higher ($42 \mu\text{L}/\text{min}/10^6$ cells). In general, unbound ICG-pHLIP (not bound to serum proteins) exhibits a moderate rate of hepatic clearance.

Safety pharmacology profiling of ICG-pHLIP ($2 \mu\text{M}$) was performed *in vitro* using 86 enzyme and receptor targets. The most significant inhibitory effect of ICG-pHLIP was

observed on progesterone B, a nuclear receptor activated by the steroid hormone progesterone. A subsequent study of ICG-pHLIP's interaction with progesterone B was used to establish IC_{50} and K_i for ICG-pHLIP to be 0.64 μ M and 0.51 μ M, respectively (for comparison, the IC_{50} and K_i for the known R-2050 progesterone agonist are several fold lower, 0.33 nM and 0.26 nM, respectively, Supplementary Figure S3). It is unlikely that a significant amount of ICG-pHLIP would reach the nucleus after a single i.v. administration of the agent, since it binds to cellular membranes.

The genotoxicity of ICG-pHLIP was evaluated using *in vitro* bacterial reverse mutation and mammalian cell micronucleus tests in human peripheral blood lymphocytes (see details in Supplementary Information). ICG-pHLIP did not show any evidence of genotoxic activity in these *in vitro* mutagenicity assays.

Animal Studies

All animal work performed at the University of Rhode Island, the Stryker Corporation, the Memorial Sloan Kettering Cancer Center (MSKCC) Antitumor Assessment Core Facility and the Charles River Labs (CRL) was carried out under approved animal protocols.

Pharmacology

Pharmacokinetic studies were performed on mice and dogs. Blood samples were collected at 5, 15, 30 min and 1, 2, 4, 6, 8, 12 or 16, 24 and 48 h after a single i.v. dose of ICG-pHLIP (12.3 mg/kg to mice and 0.064 mg/kg to dogs). Evidence of systemic exposure to ICG-pHLIP was observed in all animals and was quantifiable up to 8-16 hours post administration (Supplementary Table S3). Single exponential decays were

observed in both cases (Figure 1f, g). The mean clearance (Cl), volume of distribution (V_z) and elimination half-time ($T_{1/2}$) values obtained for mice and dogs were very similar: $Cl = 9.53$ mL/h/kg (mice) and 11.6 mL/h/kg (dogs); $V_z = 53.51$ mL/kg (mice) and 61.6 mL/kg (dogs); and $T_{1/2} = 3.9$ h (mice) and 3.7 h (dogs).

Blood Vessel Imaging

Our data show that ICG-pHLIP has a strong affinity to plasma proteins resulting in a relatively slow blood clearance: the agent remains at significant levels in the blood for several hours. These are essential features of a good blood pool agent for fluorescence angiography. Free ICG is currently used as a contrast agent for imaging blood flow, and it also binds to plasma proteins; however, it is cleared from the blood within a few minutes, allowing only a limited time window for imaging. We carried out a comparative study of blood flow imaging using ICG-Cys (ICG-maleimide conjugated with a Cys residue) and ICG-pHLIP (2.5 nmol of each). As expected, ICG-Cys was cleared from the blood within the first 5 min (Figure 2a), whereas ICG-pHLIP clearly revealed the blood vessels for up to 2 hours (Figure 2b and Supplementary Figures S4). To further investigate the potential utility of ICG-pHLIP in fluorescence angiography, blood perfusion was imaged in pigs, since the blood circulation of pigs is closely related to that of humans. The pig received several doses of ICG-pHLIP: 0.052 mg/kg (dose 1) followed by additional 0.12 mg/kg (dose 2) and then followed by additional 0.24 mg/kg (dose 3). Visualization of ICG-pHLIP NIR fluorescence in blood vessels was performed using two systems: i) for endoscopic/laparoscopic imaging inside the pig body cavity (Figure 3a, Supplementary Figure S5a and Supplementary Video S1), and ii) open field imaging of a pedicle flap (Figure 3b, Supplementary Figure S5b and Supplement Video S2). Illuminated blood vessels were

clearly visible at 2 hours post-injection (Supplement Figure S5), establishing the superiority of ICG-pHLIP use over ICG in fluorescence angiography and other blood flow/perfusion applications.

Biodistribution and Tumor Targeting

Biodistribution and tumor targeting were followed after a single tail vein injection of ICG-pHLIP in mice bearing murine and human tumors. Biodistribution studies were carried out in female and male mice bearing a triple negative 4T1 tumor, which closely mimics stage IV of human breast cancer. Targeting of 4T1 tumors in BALB/c mice by ICG-pHLIP is shown in Supplementary Figure S6. To establish the biodistribution of ICG-pHLIP, animals were euthanized at different time points (5 min, 1, 2, 4, 6, 16, 26 and 48 h), organs were collected and imaged. Representative images of organs are shown in Figure 4a (values of fluorescence intensity are shown in Supplementary Table S4 and mean values are given in Supplementary Table S5, the calculated signal level in each organ at different time points is shown in Supplementary Figure S7). The kinetics of fluorescence signal changes in organs and tissue is shown in Figure 4b-g. Organs and tissues were frozen after imaging and processed to measure the signal in the tissue/organ homogenates. It is challenging to establish precisely the amount of fluorescent compound in the tissue and organs. However, we made rough estimations using a calibration curve, which was obtained by spiking known amounts of ICG-pHLIP with organs and tissue homogenates collected from control animals. According to our estimates the amount of ICG-pHLIP within the tumor reaches about 10-15% ID/g at 4 hours post injection and stays constant up to 24 h, decaying slightly at 48 h. The clearance was observed to be predominantly hepatic, and the level of the signal increases in the liver with time and reaches a maximum level at 1-hour post-

administration, followed by the decay of the signal after 6 hours. Well-perfused organs like the heart, kidney and lungs were imaged as is (no perfusion with buffer), and it is evident that a significant amount of the signal (especially at earlier time points) is coming from the blood associated with these organs, and that the level of the signal decays with blood clearance. Another group of organs, such as spleen, pancreas, stomach and brain have a lower signal level, which also decays with blood clearance. Small and large intestines, bone, skin and muscle (and prostate in male animals, not shown here) have very low signal levels, estimated to be less than 2% ID/g at all time points. At 20-48 h, when the blood is cleared and the fluorescence signal in all organs is minimal, the contrast between tumor and surrounding tissue or healthy organs is very significant.

ICG-pHLIP tumor targeting was observed in several tumor models of breast (MDA-MB-231 human and 4T1 murine), lung (A549 human and LLC murine), epithelial (melanoma) (M4A4 human), cervical (HeLa human), urinary bladder (UM-UC3 human) and prostate (LNCaP human) cancers. NIR fluorescence imaging on live animals using the Stryker clinical imaging system was performed at 24 h after a single i.v. administration of ICG-pHLIP (Supplementary Figure S8). To closely mimic the conditions of intraoperative imaging, during which fluorescence is monitored from exposed tissue, the skin was removed from the tumor side while animals were under anesthesia. Excellent tumor targeting by ICG-pHLIP was seen, and small, medium and large tumors positioned deep in tissue or exposed at the surface, including small nearby micro-metastases, were clearly seen (representative images are shown in Figure 5). To further examine the contrast between tumor and normal tissue, the tumors were removed with surrounding muscle tissue (Figure 6). The border between tumor and

muscle in most cases was evidently visible and was defined with high precision by the fluorescence signal. To correlate the ICG-pHLIP NIRF signal with tumor location, the tumor-muscle pieces were frozen immediately following NIRF imaging, sectioned, fixed and stained with hematoxylin and eosin (HE). An excellent correlation between ICG-pHLIP imaging and HE histopathology in locating the tumors is shown in Figure 7 and Supplementary Figure S9. Fluorescent (non-processed) and HE stained sections were examined via an IR scanner and optical microscope. Tumors (marked as T) and surrounding stroma (marked as S1, S2 and S3) exhibit ICG-pHLIP NIR fluorescent signal, as opposed to the muscles (marked as M1 and M2), which have little signal. Cancer cells infiltrating into surrounding muscles are clearly seen in magnified images of stroma. The ability of ICG-pHLIP to stain a tumor mass as well as surrounding tissues with infiltrating cancer cells is expected to aid improved margin resection during surgery.

Fluorescence-Guided Tumor Resection

Murine breast cancer 4T1 and human cervical HeLa tumors were implanted into athymic female nude mice. ICG-pHLIP was given as a single i.v. injection at doses 0.5, 1.25 and 2.5 mg/kg. Surgeries were performed 24 and 48 h after injection under fluorescence guidance using a Stryker SPY-PHI handheld clinical instrument, which will be used in breast cancer surgical clinical trials for imaging of ICG-pHLIP. The images and video obtained during the procedure are shown in Figure 8 and Supplementary Video S3.

GLP Safety Animal Studies

The animal efficacy studies indicated that a dose of 0.5 mg/kg of ICG-pHLIP gives satisfactory imaging, which corresponds to 0.04 mg/kg human dose (h.d.). Toxicology studies were performed assuming the minimum human dose (h.d.) to be 0.04 mg/kg (the details of these studies can be found in the Section “Pharmacology and Toxicology Studies” Supplementary Information). In summary, the following GLP studies were carried out and no adverse effects were observed:

Single-dose and 7-days repeat i.v. toxicity in beagle dogs: ICG-pHLIP was administered by single i.v. bolus injection at 0.063 mg/kg (0.85× h.d. recalculated for dog dose), 1.08 mg/kg (15× h.d.), 2.16 mg/kg (30× h.d.) or once daily for 7 days at 2.16 mg/kg/day (30× h.d. per day) to dogs, and did not adversely affect the overall health or condition of the animals, any of the measured clinical pathology parameters, organ weights, macroscopic or microscopic pathology. Based on these results, the no-observed-adverse-effect level (NOAEL) was 2.16 mg/kg/day (30× h.d. per day) in males and females.

7-day repeat i.v. toxicity in B6D2F1 mice: ICG-pHLIP was administered once daily for 7 days at 4.92 mg/kg/day (1× h.d. per day), 7.38 mg/kg/day (15× h.d. per day) and 12.3 mg/kg/day (25× h.d. per day). The repeat administration of ICG-pHLIP did not result in any signs of systemic or delayed toxicity in male and female mice.

A cardiovascular telemetry study in unrestrained, conscious non-naïve beagle dogs: A single administration of ICG-pHLIP at dose levels of 0.072 mg/kg (1× h.d.), 0.36 mg/kg (5× h.d.), and 1.44 mg/kg (20× h.d.) to male dogs resulted in no effect on systemic blood pressures, heart rate, body temperature, electrocardiographic intervals, or qualitative ECG parameters up to 24 hours post-dose.

Local tolerance/irritancy in New Zealand white rabbits: A single administration of ICG-pHLIP at dose levels of 0.124 mg/kg (1× h.d.) and 1.86 mg/kg (15× h.d.) through

all routes of administration was well tolerated and did not result in any ICG-pHLIP related changes.

A pharmacological safety assessment on the central nervous system in Sprague Dawley rats: A single administration of ICG-pHLIP at dose levels of 0.218 mg/kg (0.88× h.d.), 0.248 mg/kg (1× h.d.), 3.72 mg/kg (15× h.d.) and 7.44 mg/kg (30× h.d.) had no effect on the central nervous system up to 24 h post-dose.

Micronucleus test in Sprague Dawley rats: A single administration of ICG-pHLIP at dose levels of 6.25 mg/kg (25× h.d.), 12.5 mg/kg (50× h.d.) and 25 mg/kg (100× h.d.) showed no evidence of genotoxic activity.

Discussion

The clinical use of ICG fluorescence imaging is growing and has stimulated the production of a large variety of instruments for open, endoscopic and laparoscopic surgical procedures³². Following intravenous injection, ICG is rapidly bound to plasma proteins, with minimal leakage into the interstitium. The blood half-life is 2.5 min^{33,34}. There are no known metabolites. ICG is rapidly extracted by the liver without modification and nearly exclusively excreted by the liver, appearing unconjugated in the bile approximately 8 min after injection, depending on liver vascularization and function²⁰. When injected outside blood vessels, ICG binds to proteins and is found in the lymph, reaching the nearest draining lymph node usually within 15 min, and after 1–2 h, it binds to the regional lymph nodes, deposited into macrophages^{35,36}. The intravenous injection dose of ICG typically varies in the range from 0.5 mg/mL/kg to 2.0 mg/mL/kg of body weight. No significant acute toxic effects have been observed in humans at a high dose of 5 mg/kg of body weight²⁰, and chronic toxicity has not been reported during many years of clinical experience.

Even though fluorescence-guidance using ICG allowed improvement of surgical procedures there remain several important limitations associated with the use of ICG. ICG (as any non-targeted small molecule including fluorescent dye) has no strong accumulation within tumors except a weak signal from enhanced permeation retention (EPR) in vascularized tumors. ICG may be taken up by some cancerous lesions only if the blood flow uptake is enhanced for the particular lesion. In other cases, ICG has been used to visualize a lesion via a lack of signal, where the uptake/signal of ICG was much lower within the lesion compared to the surrounding tissue³⁷. However, ICG, does not have any inherent tumor-targeting properties based on selective binding. Also, the use of ICG for blood-flow visualization is limited by its very fast blood clearance profile, which requires sometimes multiple injections during the same surgical procedure. ICG-pHLIP resolves these deficiencies.

Tumor targeting by pHLIP has been well-documented in a large variety of animal tumor models and human tissues. ICG-pHLIP was used to image cancerous lesions in human bladders³¹ and the human upper urinary tract³⁸. The agent was applied *ex vivo* after the surgical removal of organs, followed by washing and NIR fluorescent imaging using clinical imaging instruments. Bladder malignant lesions were targeted by ICG-pHLIP, identified by NIR imaging and shown by pathology to have a sensitivity of 97% and specificity of 100%. Carcinoma *in situ* was accurately diagnosed in 11 cases, whereas only four of these cases were seen using white light. All malignant upper tract lesions were targeted by ICG-pHLIP and visualized on NIR imaging with a sensitivity of 100% (compared to 78.9% white light imaging) and a specificity of 100%. Benign collecting systems and ureters did not show uptake of the pHLIP construct. Fluorescent pHLIP peptides were also used in applications to other human tissues for accurate identification of cancerous lesions^{39,40}.

Taken together, the published work on the mechanism of pHLIP action, on tumor targeting and visualization, as well as in the preclinical studies with the ICG-pHLIP presented here, including PoC, pharmacology and toxicology assessments, motivate the clinical translation of ICG-pHLIP for systemic administration for i) real-time blood flow visualization and ii) targeting and identification of cancerous lesions during surgical procedures. The agent will be initially evaluated in a first-in-human trial on breast cancer patients, which will combine advanced pre-operative multiparametric MRI for the comprehensive assessment of tumor microenvironment including tumor acidity with intra- and post-operative NIR fluorescent imaging, standard histopathological and molecular profiling analysis. It is expected that ICG-pHLIP might allow accurate identification of tumor margins, targeting and visualization of flat lesions and the identification of micro-metastasis nearby a primary tumor mass, which are difficult to establish by the naked eye or white light imaging. Further, real time blood flow imaging with ICG-pHLIP is expected to significantly extend the imaging time window from several minutes to several hours, allowing imaging to be performed any time during a surgical procedure after a single injection of the agent. Potentially, multi-color imaging could be developed: ICG-pHLIP could be used to visualize blood vessels, and pHLIP with a fluorescent dye emitting in the range of 600-700 nm could be used for tumor imaging, allowing imaging of cancerous lesions and blood vessels during the same surgical procedure.

Acknowledgements

The authors are grateful for the support of Dr Sonia Sequeira, members of the MSKCC Antitumor Assessment Core Facility and the Radiochemistry and Molecular Imaging Probe Core supported by NIH P30 CA008748, as well as members of the URI

Institutional Development Award (IDeA) Network for Biomedical Research Excellence supported by NIH P20 GM103430. This work was supported by NIH grants RO1 GM073857 (Y.K.R., O.A.A. and D.M.E.), R35 CA232130 (J.S.L.) and F32 EB025050 (L.M.C).

Author Contributions

Y.K.R., O.A.A. and J.S. designed the experiments. T.C., A.M., S.R., D.W., M.DuP., L.M.C., J.S. carried out the experiments. T.C., D.W., L.M.C, J.S., and Y.K.R. analyzed the data. Y.K.R., D.M.E., J.S.L, and O.A.A. interpreted the experiments. All authors read, provided feedback on, and approved the manuscript for publication.

Competing Interests

D.M.E., J.S.L., O.A.A. and Y.K.R. are founders of pHLIP, Inc. They have shares in the company, and the company provided funding for manufacturing of ICG-pHLIP, safety, pharmacology and toxicology studies.

References

- 1 Unno, N. *et al.* Indocyanine green fluorescence angiography for intraoperative assessment of blood flow: a feasibility study. *Eur J Vasc Endovasc Surg* **35**, 205-207, (2008).
- 2 Handa, T., Katare, R. G., Sasaguri, S. & Sato, T. Preliminary experience for the evaluation of the intraoperative graft patency with real color charge-coupled device camera system: an advanced device for simultaneous capturing of color and near-infrared images during coronary artery bypass graft. *Interact Cardiovasc Thorac Surg* **9**, 150-154, (2009).
- 3 Woitzik, J., Horn, P., Vajkoczy, P. & Schmiedek, P. Intraoperative control of extracranial-intracranial bypass patency by near-infrared indocyanine green videoangiography. *J Neurosurg* **102**, 692-698, (2005).
- 4 Murray, J. D., Jones, G. E., Elwood, E. T., Whitty, L. A. & Garcia, C. Fluorescent intraoperative tissue angiography with indocyanine green: evaluation of nipple-areola vascularity during breast reduction surgery. *Plast Reconstr Surg* **126**, 33e-34e, (2010).
- 5 Azuma, R. *et al.* Detection of skin perforators by indocyanine green fluorescence nearly infrared angiography. *Plast Reconstr Surg* **122**, 1062-1067, (2008).
- 6 Lee, B. T. *et al.* Intraoperative near-infrared fluorescence imaging in perforator flap reconstruction: current research and early clinical experience. *J Reconstr Microsurg* **26**, 59-65, (2010).
- 7 Cahill, R. A. *et al.* Near-infrared (NIR) laparoscopy for intraoperative lymphatic road-mapping and sentinel node identification during definitive surgical resection of early-stage colorectal neoplasia. *Surg Endosc* **26**, 197-204, (2012).

- 8 Debie, P. & Hernot, S. Emerging Fluorescent Molecular Tracers to Guide Intra-Operative Surgical Decision-Making. *Front Pharmacol* **10**, 510, (2019).
- 9 Vahrmeijer, A. L., Hutteman, M., van der Vorst, J. R., van de Velde, C. J. & Frangioni, J. V. Image-guided cancer surgery using near-infrared fluorescence. *Nat Rev Clin Oncol* **10**, 507-518, (2013).
- 10 Mondal, S. B. *et al.* Real-time fluorescence image-guided oncologic surgery. *Adv Cancer Res* **124**, 171-211, (2014).
- 11 Jacobs, L. Positive margins: the challenge continues for breast surgeons. *Ann Surg Oncol* **15**, 1271-1272, (2008).
- 12 Burggraaf, J. *et al.* Detection of colorectal polyps in humans using an intravenously administered fluorescent peptide targeted against c-Met. *Nat Med* **21**, 955-961, (2015).
- 13 Stummer, W. *et al.* Fluorescence-guided surgery with 5-aminolevulinic acid for resection of malignant glioma: a randomised controlled multicentre phase III trial. *Lancet Oncol* **7**, 392-401, (2006).
- 14 Roberts, D. W. *et al.* Coregistered fluorescence-enhanced tumor resection of malignant glioma: relationships between delta-aminolevulinic acid-induced protoporphyrin IX fluorescence, magnetic resonance imaging enhancement, and neuropathological parameters. Clinical article. *J Neurosurg* **114**, 595-603, (2011).
- 15 Rink, M. *et al.* Hexyl aminolevulinate-guided fluorescence cystoscopy in the diagnosis and follow-up of patients with non-muscle-invasive bladder cancer: a critical review of the current literature. *Eur Urol* **64**, 624-638, (2013).
- 16 Burger, M. *et al.* Photodynamic diagnosis of non-muscle-invasive bladder cancer with hexaminolevulinate cystoscopy: a meta-analysis of detection and recurrence based on raw data. *Eur Urol* **64**, 846-854, (2013).

- 17 Santos Cortes, J. A., Gahan, J. & Soloway, M. S. Photodynamic diagnosis in urology: state of the art. *Arch Esp Urol* **64**, 18-31 (2011).
- 18 Lerner, S. P., Liu, H., Wu, M. F., Thomas, Y. K. & Witjes, J. A. Fluorescence and white light cystoscopy for detection of carcinoma in situ of the urinary bladder. *Urol Oncol* **30**, 285-289, (2012).
- 19 Marshall, M. V. *et al.* Near-Infrared Fluorescence Imaging in Humans with Indocyanine Green: A Review and Update. *Open Surg Oncol J* **2**, 12-25, (2010).
- 20 Alander, J. T. *et al.* A review of indocyanine green fluorescent imaging in surgery. *Int J Biomed Imaging* **2012**, 940585, (2012).
- 21 Polom, K. *et al.* Current trends and emerging future of indocyanine green usage in surgery and oncology: a literature review. *Cancer* **117**, 4812-4822, (2011).
- 22 Zelken, J. A. & Tufaro, A. P. Current Trends and Emerging Future of Indocyanine Green Usage in Surgery and Oncology: An Update. *Ann Surg Oncol* **22 Suppl 3**, S1271-1283, (2015).
- 23 Griffiths, M., Chae, M. P. & Rozen, W. M. Indocyanine green-based fluorescent angiography in breast reconstruction. *Gland Surg* **5**, 133-149, (2016).
- 24 Flower, R. W. Injection technique for indocyanine green and sodium fluorescein dye angiography of the eye. *Invest Ophthalmol* **12**, 881-895 (1973).
- 25 Wei, D., Engelman, D. M., Reshetnyak, Y. K. & Andreev, O. A. Mapping pH at Cancer Cell Surfaces. *Mol Imaging Biol*, (2019).
- 26 Wyatt, L. C., Lewis, J. S., Andreev, O. A., Reshetnyak, Y. K. & Engelman, D. M. Applications of pHLIP Technology for Cancer Imaging and Therapy: (Trends in Biotechnology 35, 653-664, 2017). *Trends Biotechnol* **36**, 1300, (2018).

- 27 Anderson, M., Moshnikova, A., Engelman, D. M., Reshetnyak, Y. K. & Andreev, O. A. Probe for the measurement of cell surface pH in vivo and ex vivo. *Proc Natl Acad Sci U S A* **113**, 8177-8181, (2016).
- 28 Pillai, S. R. *et al.* Causes, consequences, and therapy of tumors acidosis. *Cancer Metastasis Rev* **38**, 205-222, (2019).
- 29 Damaghi, M., Wojtkowiak, J. W. & Gillies, R. J. pH sensing and regulation in cancer. *Front Physiol* **4**, 370, (2013).
- 30 Adochite, R. C. *et al.* Comparative Study of Tumor Targeting and Biodistribution of pH (Low) Insertion Peptides (pHLIP((R)) Peptides) Conjugated with Different Fluorescent Dyes. *Mol Imaging Biol* **18**, 686-696, (2016).
- 31 Golijanin, J. *et al.* Targeted imaging of urothelium carcinoma in human bladders by an ICG pHLIP peptide ex vivo. *Proc Natl Acad Sci U S A* **113**, 11829-11834, (2016).
- 32 AV, D. S., Lin, H., Henderson, E. R., Samkoe, K. S. & Pogue, B. W. Review of fluorescence guided surgery systems: identification of key performance capabilities beyond indocyanine green imaging. *J Biomed Opt* **21**, 80901, (2016).
- 33 Benson, R. C. & Kues, H. A. Fluorescence properties of indocyanine green as related to angiography. *Phys Med Biol* **23**, 159-163 (1978).
- 34 Desmettre, T., Devoisselle, J. M. & Mordon, S. Fluorescence properties and metabolic features of indocyanine green (ICG) as related to angiography. *Surv Ophthalmol* **45**, 15-27, (2000).
- 35 Tajima, Y. *et al.* Sentinel node mapping guided by indocyanine green fluorescence imaging during laparoscopic surgery in gastric cancer. *Ann Surg Oncol* **17**, 1787-1793, (2010).

- 36 Korn, J. M., Tellez-Diaz, A., Bartz-Kurycki, M. & Gastman, B. Indocyanine green SPY elite-assisted sentinel lymph node biopsy in cutaneous melanoma. *Plast Reconstr Surg* **133**, 914-922, (2014).
- 37 Mitsui, Y. *et al.* Indocyanine green (ICG)-based fluorescence navigation system for discrimination of kidney cancer from normal parenchyma: application during partial nephrectomy. *Int Urol Nephrol* **44**, 753-759, (2012).
- 38 Brito, J. *et al.* Ex-vivo Imaging of Upper Tract Urothelial Carcinoma Using Novel ICG-Var3 pHLIP Imaging Agent. *Urology*, (2019).
- 39 Luo, Z. *et al.* Widefield optical imaging of changes in uptake of glucose and tissue extracellular pH in head and neck cancer. *Cancer Prev Res (Phila)* **7**, 1035-1044, (2014).
- 40 Loja, M. N. *et al.* Optical molecular imaging detects changes in extracellular pH with the development of head and neck cancer. *Int J Cancer* **132**, 1613-1623, (2013).

Figure Legends

Figure 1. Characterization of ICG-pHLIP and blood clearance in mice and dogs.

(a) The Var3 pHLIP sequence is shown with the chemical structure of the ICG dye coupled to a single Cys residue at the N-terminal part of pHLIP. (b) Normalized absorbance (black line) and fluorescence (red line) spectra (the excitation is at 805 nm) of ICG-pHLIP (5 μ M) measured in DMF. (c) Circular dichroism (CD) spectra of ICG-pHLIP measured in phosphate buffer (pH8) in absence (ICG-pHLIP, pH8 – black line) and presence (ICG-pHLIP + PC, pH8 – blue line) of POPC liposomes, and in the presence of POPC liposomes at pH5.2 (ICG-pHLIP + PC, pH5.2 – red line). (d) pH-dependent insertion of ICG-pHLIP into the bilayers of POPC liposomes monitored by changes of the CD spectral signal at 222 nm. The data were fitted with the Henderson-Hasselbach equation (red line with 95% confidence interval) to establish the midpoint of the transition (pK). (e) The kinetics signal (multiplied by -1) of ICG-pHLIP insertion into lipid bilayers of POPC liposomes as a result of a pH drop from pH8 (blue line in insert) to pH5 (red line in insert) was monitored in real-time by the tryptophan fluorescence changes (black line). The gray line is a baseline obtained by mixing ICG-pHLIP with POPC liposomes at pH8 with pH8 buffer. The red line is a bi-exponential fit of the experimental data (85% of the signal changes occur with a rate of 5 sec^{-1} and about 15% of final adjustment is completed at a rate of 0.077 sec^{-1}). (f-g) Blood clearance profile and single exponential fitting curves (red lines) obtained on mice (f) and dogs (g) after a single i.v. injection of 12.3 mg/kg of ICG-pHLIP to mice and 0.064 mg/kg of ICG-pHLIP to dogs are shown.

Figure 2. Imaging of blood vessels in mice. Representative NIR ICG-pHLIP fluorescent images of blood vessels at different time points after a single i.v. injection of ICG-Cys (*a*) or ICG-pHLIP (*b*).

Figure 3. Imaging of blood vessels in pigs. Representative NIR ICG-pHLIP (verification batch #1912127) fluorescent images and overlay of fluorescent and color images of blood vessels at different time points after injection of ICG-pHLIP in PBS (dose 1 - 0.052 mg/kg; dose 2 - additional 0.12 mg/kg; dose 3 - additional 0.24 mg/kg) are shown. (*a*) Imaging inside the pig body cavity was performed using a Stryker 1688 AIM system (808 nm excitation) for endoscopic/laparoscopic imaging (gain 8/10 for dose 2, gain 7/10 for dose 3). (*b*) Imaging of a pedicle flap was performed using a Stryker SPY-PHI handheld device (805 nm excitation) for open field imaging.

Figure 4. Biodistribution and kinetics. (*a*) Representative NIR ICG-pHLIP fluorescent and photo images of tumor, major organs and tissues obtained at different time points are shown after a single i.v. administration of ICG-pHLIP into BALB/c female mice bearing murine 4T1 breast tumors in right flanks. Tissues and organs were imaged immediately after necropsy. The values of the fluorescence signal obtained for all female mice are presented in Supplementary Tables S4 (the NIR fluorescent signals obtained in male mice were similar, data are not shown). (*b-g*) The calculated mean and standard deviation values at different time points post-dose are shown. The values are given in the Supplementary Table S5. The description of %ID/g calculations is presented in the main text and Methods section.

Figure 5. Tumor targeting. Representative photos and overlay of photos and *in vivo* NIR ICG-pHLIP fluorescent images of athymic female nude mice bearing murine and human tumors are shown with skin removed from the tumor site. The imaging was performed at 24 hrs after a single i.v. administration of ICG-pHLIP. Arrows indicate tumor locations.

Figure 6. *Ex vivo* imaging of tumors with surrounding muscle. Representative photos, and overlays of photos and *ex vivo* NIR ICG-pHLIP fluorescent images of tumors resected with surrounding tissue immediately after *in vivo* imaging.

Figure 7. *Ex vivo* imaging and imaging of sections. (a) Representative images of tumors with surrounding tissue: photos, NIR ICG-pHLIP fluorescent images, overlay of photos with NIR ICG-pHLIP fluorescent images, and images of HE-stained sections obtained from the same tumor-muscle pieces are shown. (b) Bright field image of HE-stained section and NIR ICG-pHLIP fluorescent images of the adjacent non-processed section obtained on IR scanner shown in monochrome (green) and 16-color (white and red are the highest intensity, and black and dark blue are the lowest intensity) presentations. T indicates tumor; M indicates muscle, and S indicates stroma. (c) Magnified bright field images (using 20x objective) of tumor (T), muscle (M1 and M2), stroma (S1, S2 and S3) of HE-stained section are presented in panel b.

Figure 8. Surgical removal of tumors under fluorescence guidance. Representative overlay of color and NIR ICG-pHLIP (verification batch #1912127) fluorescent images (a-e) and NIR fluorescent image (f) recorded using a Stryker SPY-PHI

handheld device (805 nm excitation) for open field imaging during surgical removal of tumor.

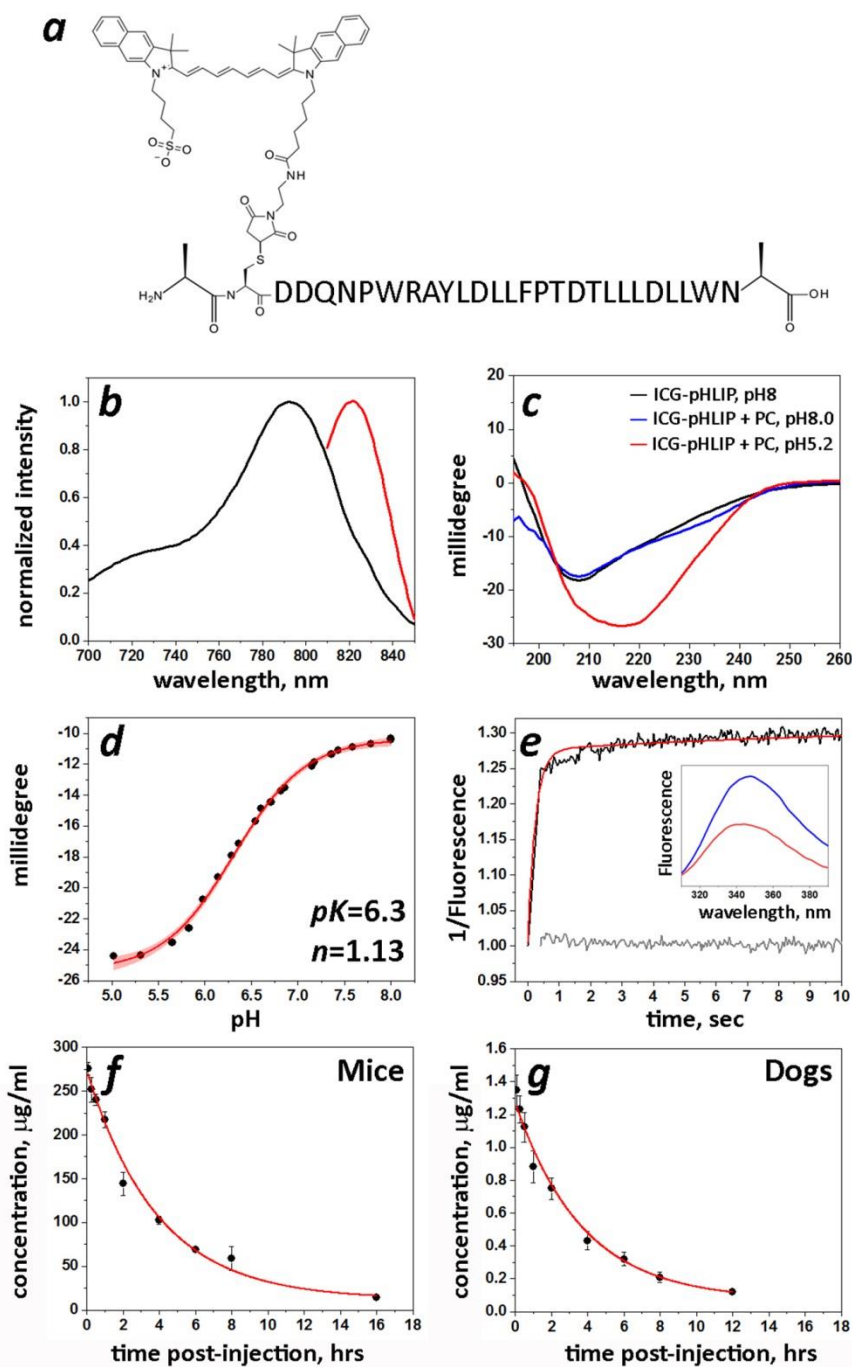


Figure 1

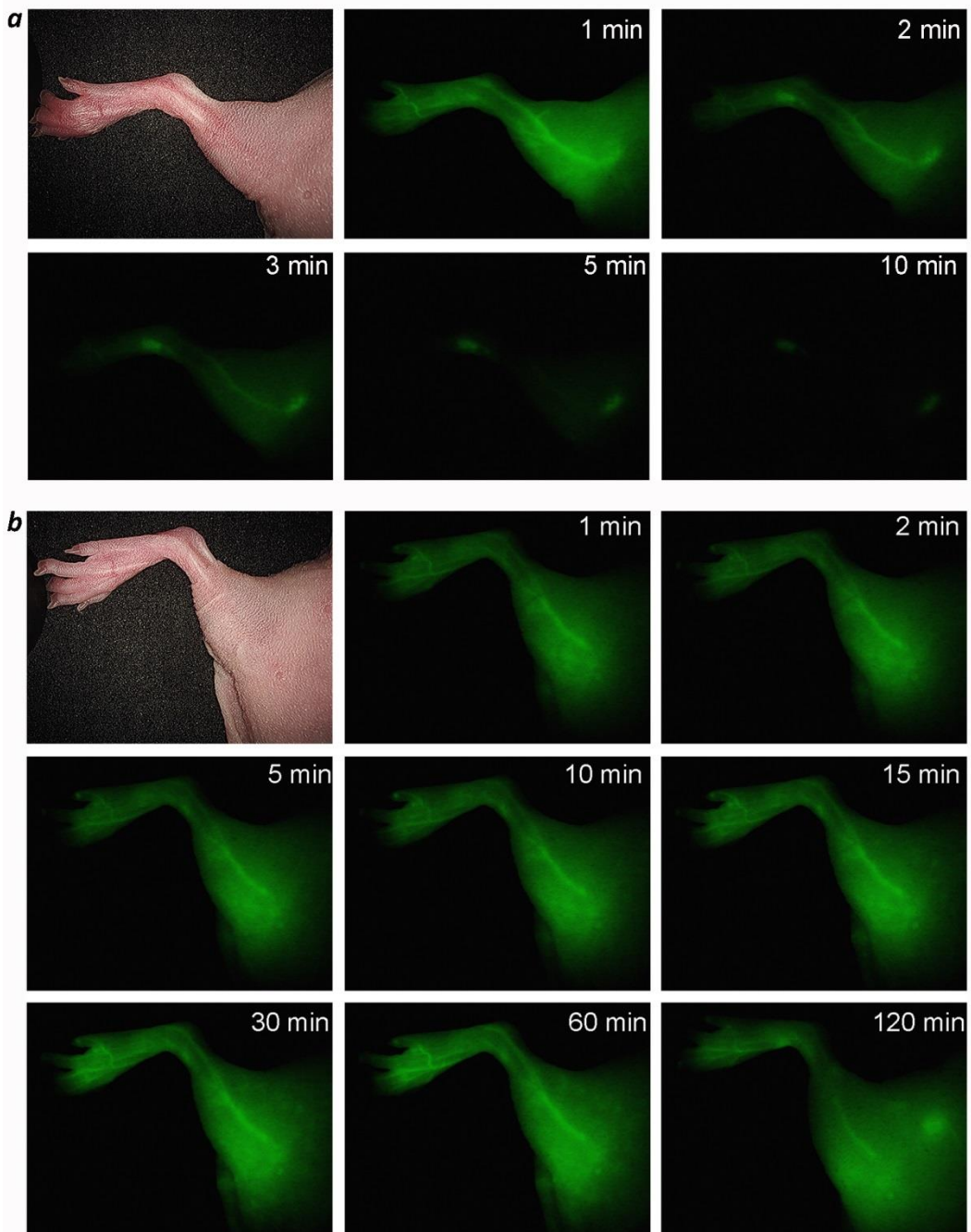


Figure 2

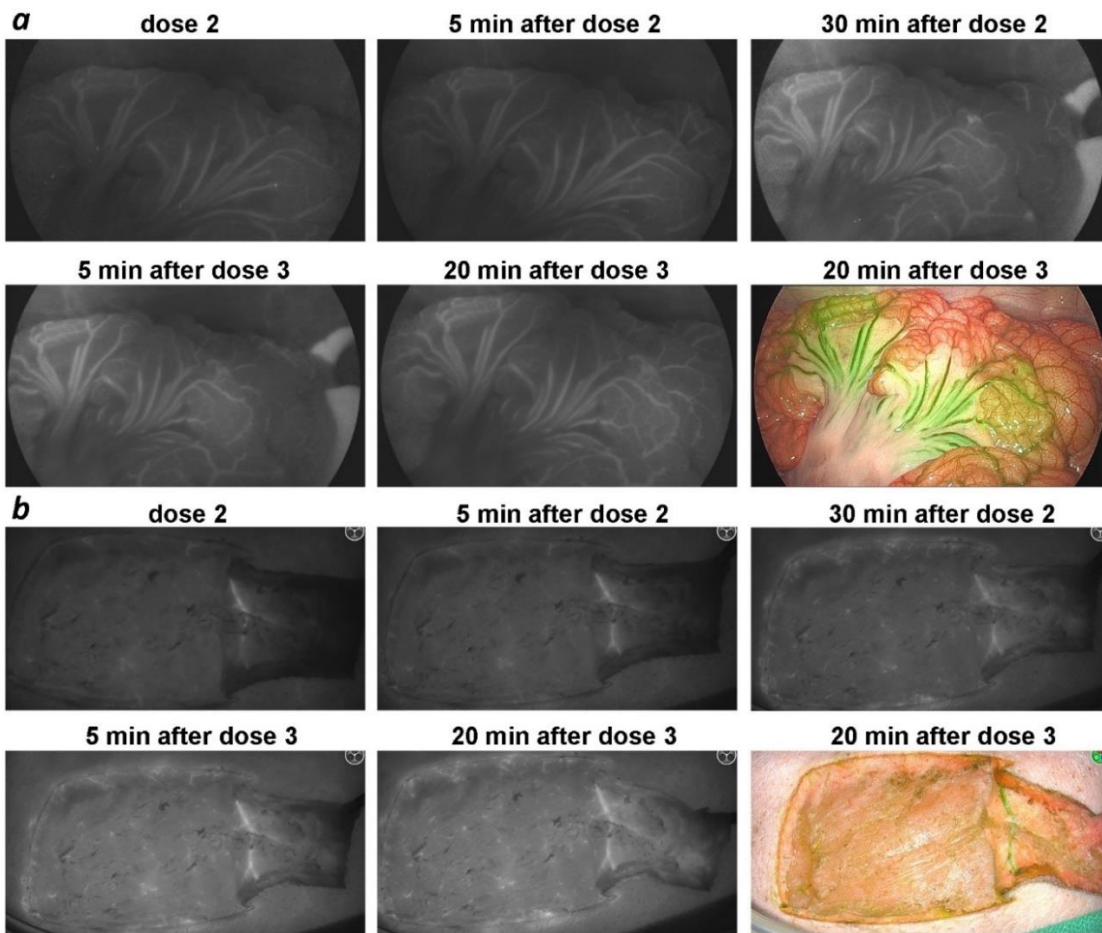


Figure 3

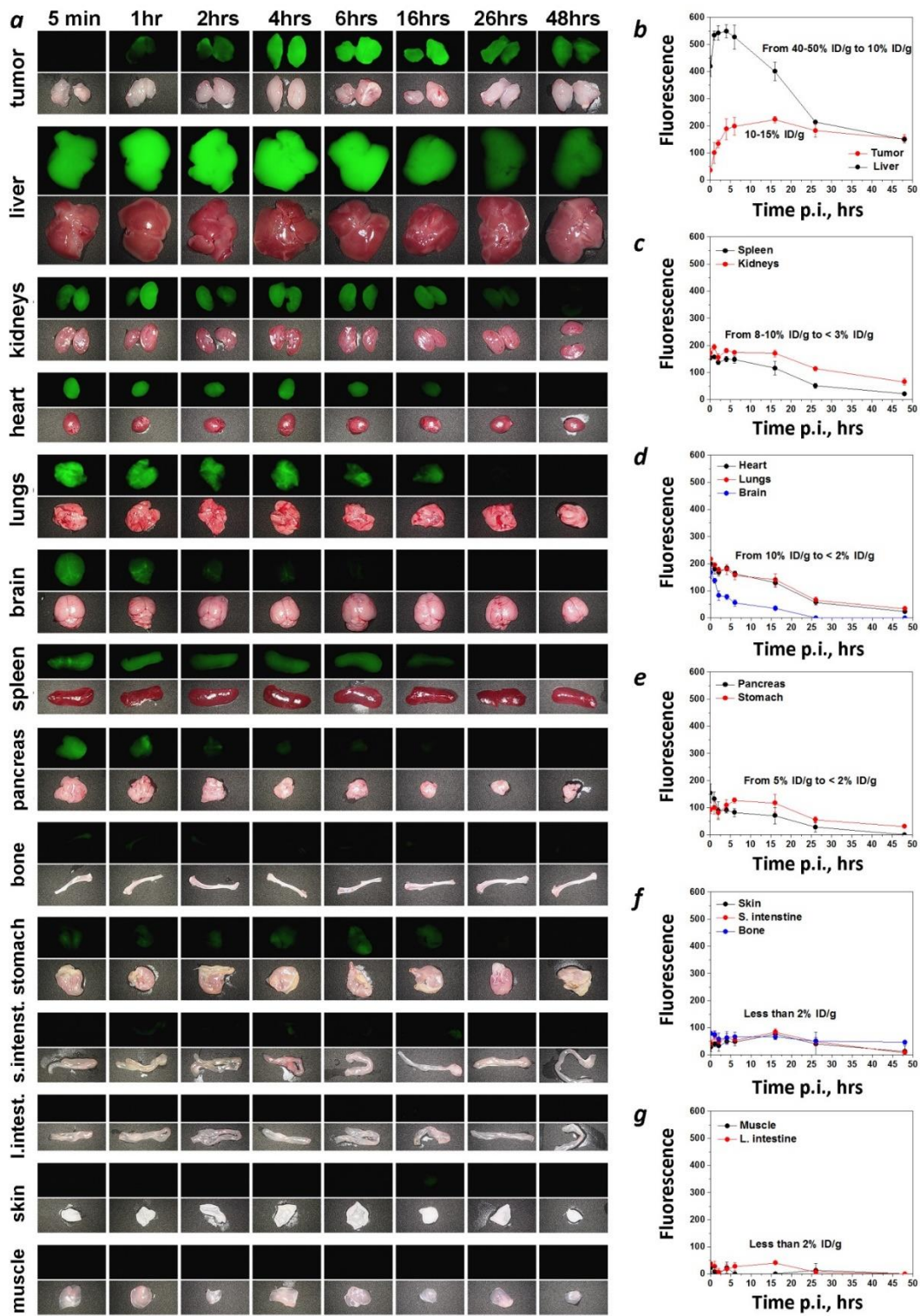


Figure 4

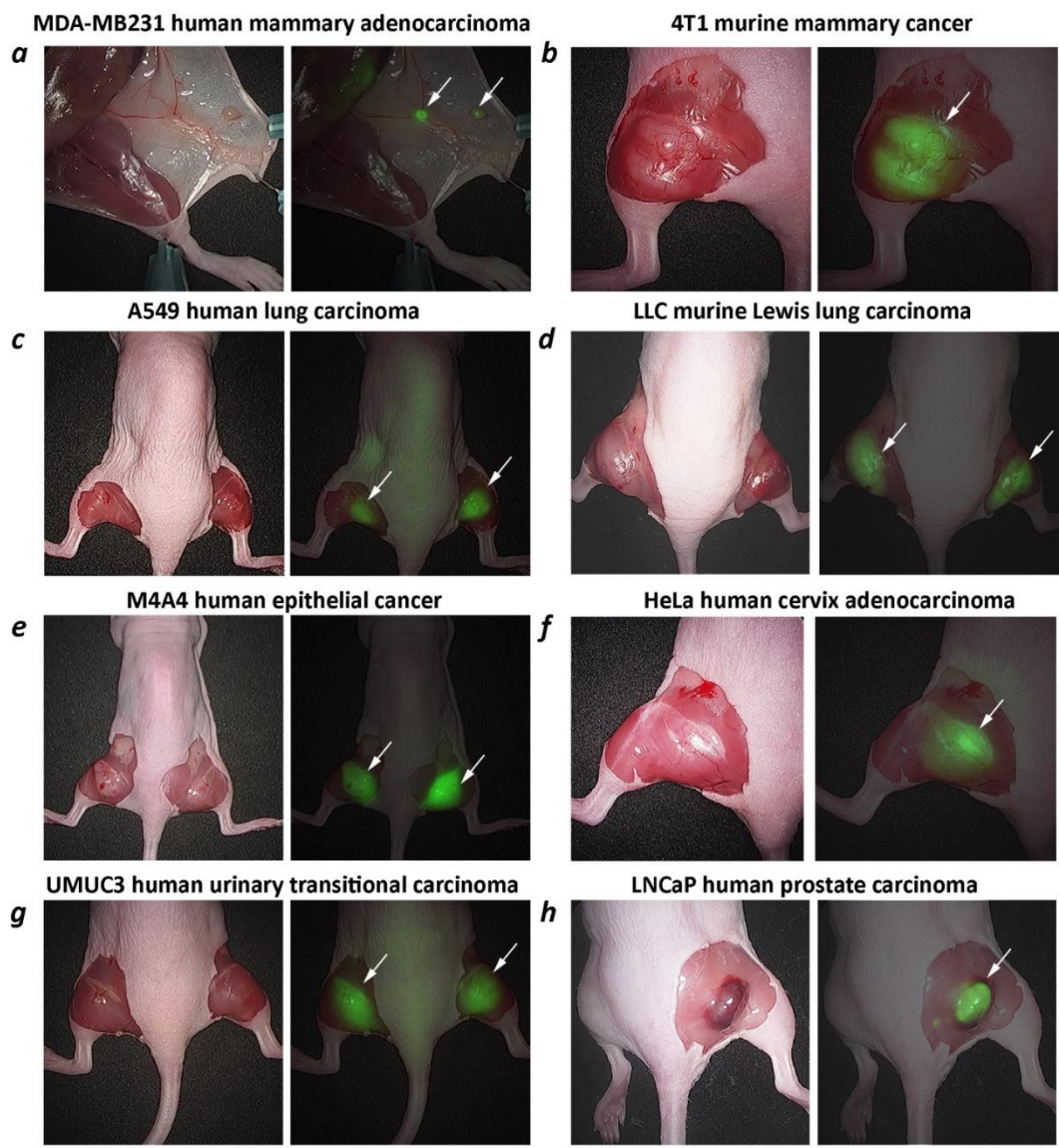


Figure 5

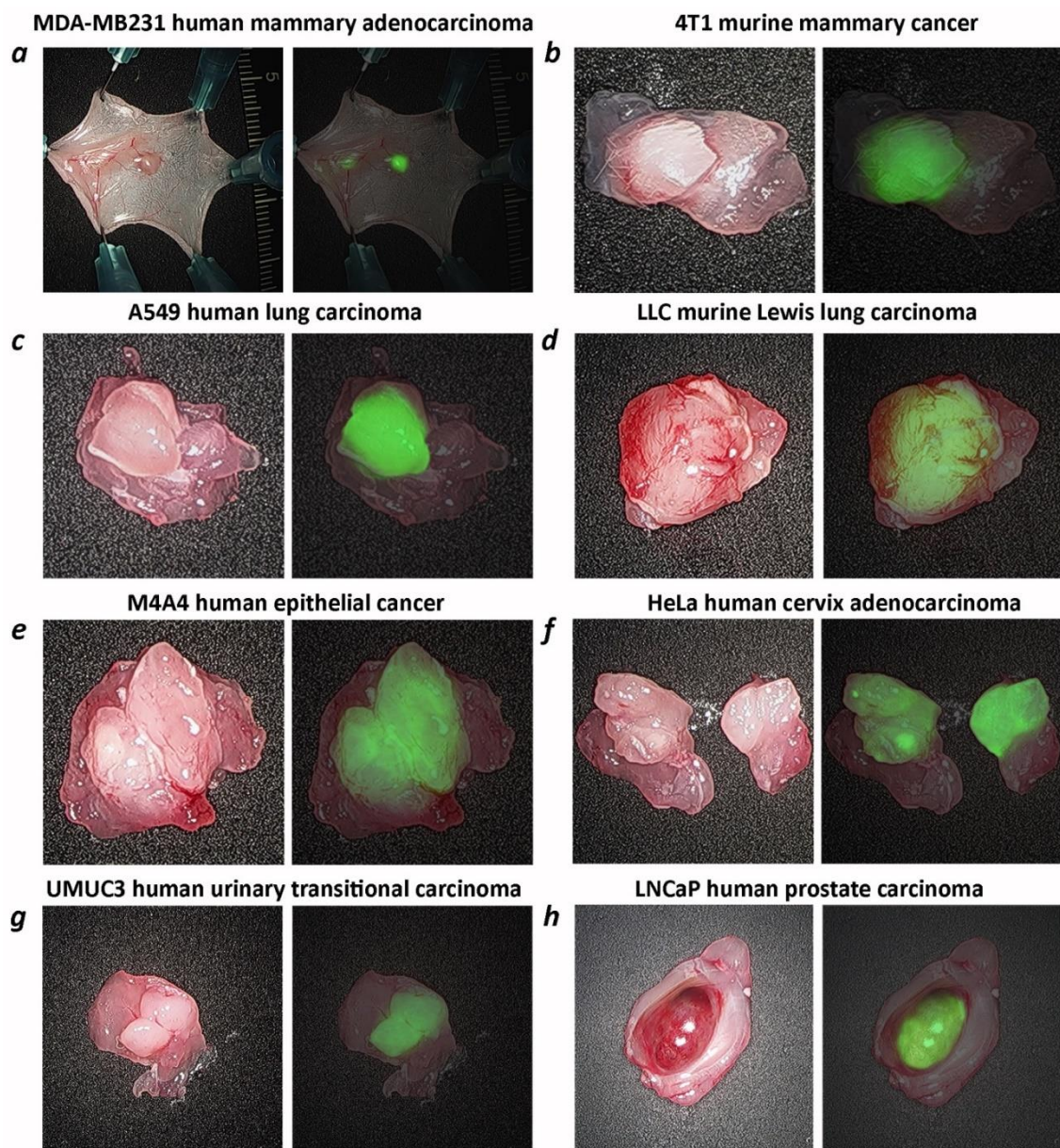


Figure 6

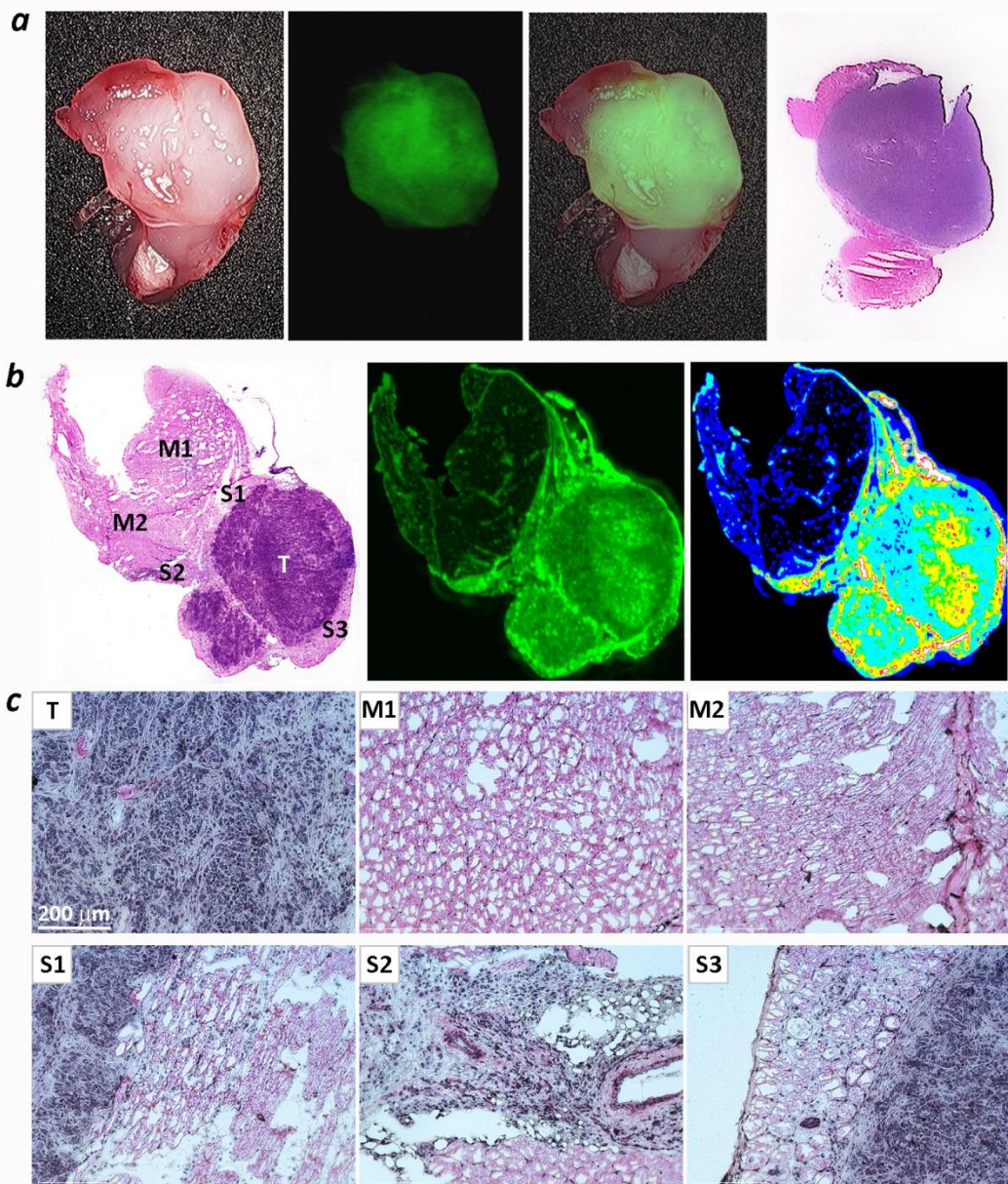


Figure 7

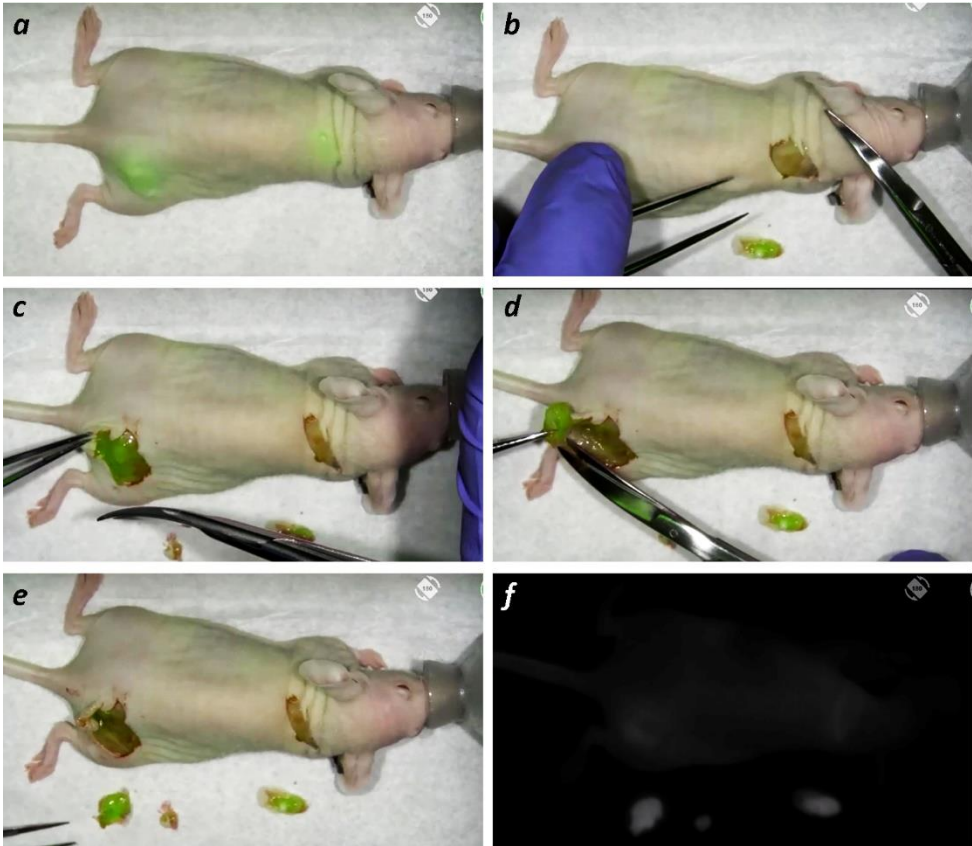


Figure 8

Supplementary Information

ICG-pHLIP for delineation of tumors and blood flow during fluorescence-guided surgery

Troy Crawford, Anna Moshnikova, Sean Roles, Dhammika Weerakkody, Michael DuPont, Lukas M. Carter, John Shen, Donald M. Engelman, Jason S. Lewis, Oleg A. Andreev, Yana K. Reshetnyak

METHODS

Manufacturing of ICG-pHLIP

All manufacturing procedures were completed in accordance with good laboratory practice (GLP) quality control specification. Synthesis of ICG-pHLIP (NH₂-Ala-Cys-Asp-Asp-Gln-Asn-Pro-Trp-Arg-Ala-Tyr-Leu-Asp-Leu-Leu-Phe-Pro-Thr-Asp-Thr-Leu-Leu-Leu-Asp-Leu-Leu-Trp-Ala-COOH) acetate salt (C₂₀₄H₂₈₃N₃₉O₅₀S₂, M.W. 4,145.8 g/mol) was developed and the agent was produced by Iris Biotech, GmbH (Germany) in partnership with Chemical and Biopharmaceutical Laboratories (CBL) (Greece). The pHLIP peptide was synthesized on a solid support, followed by purification using HPLC. ICG-maleimide was synthesized in solution, followed by column purification. ICG-maleimide was conjugated with the pHLIP peptide in solution followed by purification of the final product (ICG-pHLIP) using HPLC. Seven grams (7 g) of ICG-pHLIP were produced with a purity of 98.7% established by HPLC (Figures S1a) and identity established by mass-spectrometry (m/z-ratio of

the synthesized ICG-pHLIP was 1383.0 Da $[M+3H]^{3+}/3 \pm 1$ and the expected theoretical mass is 1382.9 Da $[M+3H]^{3+}/3$ was used in proof of concept (PoC), toxicology and pharmacokinetics studies. Manufacturing of ICG-pHLIP and analytical characterization were further optimized by CordenPharma, GmbH (Germany). The HPLC analytical method developed for the detection of ICG-pHLIP is the following: HPLC column is Waters, BEH C8, 150 x 2.1 mm, 1.7 μ m particle size; temperature is 33°C; injection volume is 1.2 μ L; eluent A is water + 0.04% TFA; eluent B is CH₃CN + 0.04% TFA; flow rate is 0.4 mL/min; detection wavelength is 220 nm; and the following gradient:

Time, min	Eluent B, %
0	30
0.63	30
3.63	50
14.88	73
15.03	95
20.13	95
20.14	30
27.63	30

A spiking experiment was used to compare the ICG-pHLIP product obtained after optimization of the manufacturing process with previously produced material. Both ICG-pHLIP products were mixed in a ratio of 1:1 and analyzed by HPLC (Figure S1b). The presence of a single signal on the HPLC chromatogram confirms the identity of ICG-pHLIP products. An m/z-determination of the material produced was performed

by UHPLC-MS. The analysis provided a m/z-ratio of 1381.96 Da $[M+3H]^{3+}/3$ (Figure S1c). GLP ICG-pHLIP verification batch #1912127 was manufactured in Frankfurt by CordenPharma, the acceptance criteria are presented in Supplementary Table S1.

Stability Study

Stability studies were performed with ICG-pHLIP formulations in PBS and PBS containing 5% DMSO or 5% Ethanol (vol/vol). The tumor targeting capability in mice is independent of formulation. Formulation of ICG-pHLIP in PBS/5% Ethanol was used in PoC animal studies, and in toxicity studies on mice, rats and dogs. For the PBS/5%DMSO formulation 1 mg of the lyophilized powder of ICG-pHLIP was dissolved in 75 μ l of DMSO (to make 3.2 mM solution), then 10 μ l of 3.2 mM stock was mixed with 190 μ l PBS to make a 0.16 mM solution of ICG-pHLIP (5% DMSO). For the PBS/5%Ethanol formulation, the lyophilized powder of ICG-pHLIP was dissolved at concentration of 1.6 mg/ml in PBS/5% Ethanol solution. Finally, the formulation selected for human use the was prepared by dissolving the lyophilized powder of ICG-pHLIP at a concentration of 0.8 mg/ml in PBS. All formulations were kept at room temperature and protected from light. The aliquots were taken at 0.5 or 1, 3, 6, 24, 48 and 72 hours (102 hrs for ICG-pHLIP dissolved in PBS) for analytical HPLC analysis using a Zorbax SB-C18 column (4.6 x 250 mm, 5 μ m) with a binary solvent system using a 15-85% water and acetonitrile gradient with 0.05% TFA over 25 min. All formulations demonstrated stability (>95% purity) up to 72 hours when kept at room temperature. Formulation of ICG-pHLIP in PBS was stable in solution for 4 days kept at RT.

Liposome Preparation

POPC (1-palmitoyl-2-oleoyl-sn-glycero-3-phosphocholine, Avanti Polar Lipids, Inc.) liposomes were used in biophysical measurements to mimic cells, and to investigate ICG-pHLIP interaction with lipid bilayers. Large unilamellar vesicles (LUVs) were prepared by extrusion. POPC dissolved in chloroform was desolvated in a rotary evaporator and placed under high vacuum for 2 hours to create a phospholipid film. Lipids were then rehydrated in phosphate buffer (pH8) and repeatedly extruded through membranes with a pore size of 100 nm to make LUVs.

Absorbtion and Emission Measurements

Absorbtion spectra of ICG-pHLIP, Methylene Blue (MB) and Isosulfan Blue (IB) in PBS, methanol, DMSO or DMF were measured in a cuvette with 1 cm path length using a Genesys 10S UV-Vis (Thermo Scientific) spectrophotometer. Fluorescence spectra of ICG-pHLIP (with an excitation of 295 nm to record tryptophan fluorescence of pHLIP, and 805 nm to record ICG fluorescence), MB (with an excitation of 670 nm) and IB (with an excitation of 630 nm, the fluorescence was insignificant) were measured in aqueous solution (in the presence or absence of POPC liposomes in the case of ICG-pHLIP), methanol, DMSO or DMF using PC1 (ISS, Inc) and SpectraMax M2 (Molecular Devices) spectrofluorometers.

Calculation of Molar Attenuation Coefficient

Different amounts of ICG-pHLIP (1.85, 1.808, 3.90, 4.15, 4.191, 7.16 and 7.19 mg) were weighed and dissolved in 2 ml of methanol followed by 25x or 50x further dilution in methanol for measurements of absorbance spectra (each spectra were recorded several times). The absorbance spectra were recorded from 700 to 900 nm. It

was ensured that the absorbance was zero at 900 nm. All spectra were normalized and adjusted for the peptide content in the sample. The OD reading at 810 nm was used to calculate the molar attenuation coefficient according to the equation:

$$\varepsilon_{810} = \frac{OD_{810}}{c \cdot l}$$

where c is the concentration of ICG-pHLIP calculated by weight and l is the optical path of the cuvette (1 cm). The mean molar attenuation coefficient for ICG-pHLIP in methanol at 810 nm was established to be $152,533 \pm 5,225 \text{ M}^{-1} \text{ cm}^{-1}$.

Circular Dichroism and pH-Dependence

Circular dichroism (CD) measurements were employed to monitor the pH-dependent insertion of ICG-pHLIP into the membrane of POPC liposomes and the formation of helical structure. CD measurements were performed using a MOS-450 spectrometer (Biologic, Inc) with its temperature control set to 25.0°C. CD spectra were recorded from 200 to 260 nm with steps of 1 nm. The pH-dependent insertion of ICG-pHLIP into the lipid bilayer of POPC liposomes was studied by monitoring the changes in the molar ellipticity (measured in millidegrees) at 222 nm as a function of pH. After the addition of aliquots of citric acid, the pHs of solutions containing 5 μM ICG-pHLIP and 750 μM POPC liposomes were measured using an Orion PerHecT ROSS Combination pH Micro Electrode and an Orion Dual Star pH and ISE Benchtop Meter before and after each spectrum measurement to ensure that equilibrium is achieved. The ellipticity millidegrees were plotted as a function of pH. The pH-dependence was fit with the Henderson-Hasselbalch equation (using OriginLab software) to determine the cooperativity (n) and the mid-point (pK) of a transition:

$$\text{Normalized pH dependence} = \frac{1}{1 + 10^{n(pH-pK)}}$$

Kinetics Measurements

To follow ICG-pHLIP insertion into the lipid bilayer of POPC liposomes in real-time, kinetics measurements were performed using a SFM-300 mixing system (Bio-Logic Science Instruments) in combination with a MOS-450 spectrometer with its temperature control set to 25.0°C. ICG-pHLIP pre-mixed with POPC liposomes at phosphate buffer at pH8 were mixed (dead time is 5 ms) with acid to drop the pH from pH8 to pH5 and promote pHLIP insertion into the bilayers. The insertion process was monitored by recording changes of the tryptophan fluorescence of pHLIP excited at 295 nm and using a cut off filter at 320 nm.

Cytotoxicity

Human mammary epithelial cells (HMEpC) acquired from Cell Applications, Inc. were authenticated and stored according to supplier's instructions. Cells were cultured in mammary epithelial cell growth medium provided by manufacturer. HMEpC cells were loaded in the wells of 96-well plates (~6,000 cells per well) and incubated overnight. Increasing amounts of ICG-pHLIP dissolved in cell growth medium were added to cells to give the following final concentrations of ICG-pHLIP with cells: 0.125, 0.25, 0.5, 1, 2, 4, 8 and 16 μM . After 48 and 72 hours of incubation, a colorimetric reagent (CellTiter 96 AQueous One Solution Assay, Promega) was added for 2 hours followed by measuring absorbance at 490 nm to assess cell viability. All samples were prepared in triplicate and each experiment was repeated several times.

Whole Blood and Plasma Binding Assays

Whole blood and plasma binding assays were performed by Cypotex US, LLC using human, mouse, rat, minipig, dog and cynomolgus monkey blood samples. ICG-pHLIP or ICG (5 μ M) was added to whole blood or plasma or PBS and dialyzed in a rapid equilibrium dialysis device (with 8 kDa cut off) against PBS. Both fractions were processed and analyzed. Solution of water/NaCl/ascorbic acid (100/37/0.5 v/w/w) and ACN/MeOH (50/50 v/v) were used to precipitate proteins, followed by evaporation of the eluent, dry and reconstitution of samples for LC-MS/MS analysis on SCIEX 6500 QTRAP mass spectrometer. The data are presented in Table S2.

pHLIP_{IS}: NH₂-A^(Cam)DDQNPWR^AYLDL^LFPTDTLLLDLL^{WA}-COOH

where A[^] is Alanine(¹³C3, ¹⁵N); L[^] is Leucine(¹³C6, ¹⁵N); R[^] is Arginine(¹³C6, ¹⁵N4); Cam is Cysteine-carbamidomethylation, synthesized and purified by New England Peptides, Inc was used as internal standard (IS).

Hepatocyte Stability Assay

Hepatocyte stability (clearance) assays were performed by Cypotex US, LLC using human, mouse, rat, minipig, dog and cynomolgus monkey pooled cryopreserved hepatocytes. ICG-pHLIP was incubated with hepatocytes at 37°C for different period of times: 0, 10, 20, 40 and 60 min (for mouse hepatocytes) and at 0, 15, 30, 60 and 120 min (for human, mini pig, rat, dog and cynomolgus monkey hepatocytes). Hepatocytes (100 μ L of concentration 0.5x10⁶ cells cells/mL) and stock solvent (PBS/EtOH, 95/5 v/v) spiked with 1 μ M ICG-pHLIP along with unspiked hepatocytes and stock solvent were placed in 0.5 mL plate. Solution of water/NaCl/ascorbic acid (100/37/0.5 v/w/w)

and ACN/MeOH (50/50 v/v) were used to precipitate proteins, followed by evaporation of the eluent, dry and reconstitution of samples for LC-MS/MS analysis. The data were calculated as % parent remaining by assuming zero minute time point peak area ratio (analyte/ pHLIP_{IS}) as 100% and dividing the remaining time point peak area ratios by zero minute time point peak area ratio. Data were fitted to a first-order decay model to determine the half-life. From the logarithmic plot of peak area against time, the slope was determined, where the (-slope) equals the elimination rate constant (k). The half-life ($t_{1/2}$) equals $0.693/k$ and the intrinsic clearance (Cl_{int}) (ml/min/ 10^6 cells) was calculated using the equation:

$$Cl_{int} = \frac{0.693V}{t_{1/2}}$$

where V equals the ratio of the incubation volume (ml) to the number of cells.

Hemolysis assay

Single donor human whole blood was purchased from Innovative Research, Inc. Red blood cells (RBCs) were collected by centrifugation of whole blood at 2000 rpm for 10 minutes followed by washing three times with Dulbecco's PBS (DPBS) and re-suspended in DPBS at a concentration of 7.5% (vol:vol). Varying concentrations of ICG-pHLIP (0.075, 0.15, 0.3, 0.6, 1.2 nmol) in DPBS were added to RBCs to give a 5% RBC suspension (the total volume of the solution with RBC was 150 μ L). The resultant mixtures were incubated at 37°C for 2 hours and then centrifuged at 1500 RCF (~3000 RMP) for 10 min. Hemolysis was assessed by the release of hemoglobin, which was monitored by measuring absorbance at 450 nm of the supernatant

hemoglobin. DPBS was used as a negative control. As positive controls, which result in 100% lysis of RBCs, we used i) water and ii) 10% of Triton X-100. The percentage of hemolysis was calculated as follows:

$$\% \text{ Hemolysis} = 100 \cdot \frac{OD_{Test} - OD_{NC}}{OD_{PC} - OD_{NC}}$$

where, OD_{Test} , OD_{NC} , and OD_{PC} are the optical density reading (absorbance) values of the test sample, negative control and positive control, respectively. The assay was performed in triplicate. The amount of RBC lysis was less than 2% in all samples. For reference, in a mouse study 2.5 nmol of ICG-pHLIP is injected per mouse (a 20-25 g mouse has about 1.2 mL of blood), or 2.08 nmol/ml (the dose in humans is much lower), while in a hemolysis assay the maximum tested concentration was 8 nmol/ml.

Enzyme Binding Assay

The ICG-pHLIP enzyme binding assays were performed by Eurofins Panlabs, Inc. according to standard assay protocols. The following enzymes were used in the binding assay with 2 μ M of ICG-pHLIP: acetyl cholinesterase; peptidase (angiotensin converting enzyme); ATPase (Na^+/K^+ , pig heart); CTSG peptidase (cathepsin G); cyclooxygenases COX-1 and COX-2; monoamine oxidases MAO-A and MAO-B; phosphodiesterases PDE3 and PDE4D2; protein tyrosine kinase (insulin receptor); protein tyrosine kinase (LCK); protein serine/threonine kinase (PKC, non-selective); adenosine A1 and A2A; adenosine transporter; adrenergic α 1A, α 1B, α 1D, α 2A, α 2B, β 1 and β 2; norepinephrine transporter (NET); androgen (testosterone); angiotensin AT1; bradykinin B2; calcium channels L-type (benzothiazepine, dihydropyridine, phenylalkylamine); calcium channel N-type; cannabinoid CB1 and CB2; chemokine CCR1; cholecystokinin CCK1 (CCKA) and CCK2 (CCKB); dopamine D1, D2L and D2S; dopamine transporter (DAT); endothelin ETA; estrogen ER α ; GABA

transporter; GABAAs (flunitrazepam, central; Ro-15-1788, hippocampus and chloride channel, TBOB); glucocorticoid; glutamate (AMPA, kainate, agonism NMDA, glycine NMDA, phencyclidine NMDA, polyamine NMDA, and mGlu5 metabotropic); glycine (strychnine-sensitive); histamine H1 and H2; chemokine CXCR2 (IL-8RB); cysteinyl leukotriene (CysLT1); melanocortin MC1 and MC4; muscarinic M1, M2, M3, and M4; tachykinin NK1; neuropeptide Y Y1; nicotinic acetylcholine $\alpha 1$ (bungarotoxin) and $\alpha 3\beta 4$; opiate $\delta 1$ (OP1, DOP), κ (OP2, KOP), and μ (OP3, MOP); platelet activating factor (PAF); potassium channels (KATP and hERG); PPAR γ ; serotonin (5-hydroxytryptamine) 5-HT1A, 5-HT1B, 5-HT2A, 5-HT2B, 5-HT2C, and 5-HT3; serotonin transporter (SERT); sodium channel (site 2); vasopressin V1A; progesterone (PR-B). The most significant inhibitory effect of ICG-pHLIP was observed on progesterone B and was followed by an additional study to identify IC_{50} values, which were determined by a non-linear least square regression analysis using MathIQT^M (ID Business Solutions Ltd., UK). The K_i values were calculated by the equation from Cheng and Prusoff [Cheng, Y., Prusoff, W.H., *Biochem. Pharmacol.* 22:3099-3108, 1973] using the observed IC_{50} of ICG-pHLIP, the concentration of radioligand employed in the assay, and the historical values for the K_D of the ligand (Eurofins Panlabs data). The Hill coefficient (n_H), defining the slope of the competitive binding curve, was calculated using MathIQT^M. The IC_{50} , K_i , and n_H values were established for ICG-pHLIP and compared to the known progesterone agonist, R-2050 (Figure S3).

Pharmacology and Toxicology Studies

Pharmacology and toxicology studies were performed at the Memorial Sloan Kettering Cancer Center (MSKCC) Antitumor Assessment Core Facility and at Charles River

Labs (CRL) under approved animal protocols. The minimum human dose (h.d.) of ICG-pHLIP is 0.04 mg/kg. All doses of ICG-pHLIP used in pharmacology and toxicology studies were calculated based on the minimum h.d.

Pharmacokinetics of ICG-pHLIP in the Beagle dogs following a single i.v. bolus injection

The objective of this study performed at CRL was to characterize the pharmacokinetic profile of ICG-pHLIP in the Beagle dogs following a single i.v. injection.

The study design was as follows:

Group No.	Test Material	Targeted Dose Level (mg/kg)	Achieved Dose Level ^a (mg/kg)	Dose Volume (mL/kg)	Achieved Dose Concentration (mg/mL)	No. of Males
1	ICG pHLIP	0.072	0.064	2.5	0.025	3

^a achieved dose levels calculated based on 87.7% mean recovery results from formulation analysis.

Blood samples were collected at 5, 15, and 30 minutes, and 1, 2, 4, 6, 8, 12, 24, and 48 hours post-dose for pharmacokinetic evaluation. Samples were placed on crushed wet ice until centrifugation, which was carried immediately. The samples were centrifuged as per standard procedures. An aliquot of 250 µL of the resultant plasma was separated, transferred to 2.0 mL low-bind tubes containing 1.25 mL of methanol, mixed and frozen immediately over dry ice and transferred to a freezer at -80°C. At the time of analysis, samples were thawed, extracted, and analyzed via LC-MS/MS according to the validated protocol using pHLIP_{IS}.

In conclusion, the administration of a single dose of ICG-pHLIP by i.v. bolus injection was well-tolerated in dogs at a dose level of 0.064 mg/kg. Evidence of systemic

exposure to ICG-pHLIP was observed in all animals and was quantifiable up to 8 or 12 hours post-dose. The mean C_0 (theoretical concentration at time zero following a bolus dose administration), AUC_{0-48hr} (area under the concentration-time curve from time zero to 48hrs) and AUC_{INF} (area under the concentration-time curve from time zero extrapolated to infinity) values were 1410 ng/mL, 5450 hr*ng/mL, and 5550 hr*ng/mL, respectively.

Pharmacokinetic testing of ICG-pHLIP in mice

The purpose of this study, performed at MSKCC, was to determine the pharmacokinetic parameters of ICG-pHLIP in 3 female B6D2F1 mice following a single i.v. injection of ICG-pHLIP at a dose of 12.3 mg/kg. Blood was collected in EDTA tubes at 5, 15, 30 minutes, and 1, 2, 4, 6, 8, 16, and 24 hours post-injection, followed by centrifugation to separate the plasma, and flash frozen. At time of analysis, samples were thawed, extracted, and analyzed via LC-MS as per the validated protocol using pHLIP_{IS}.

In conclusion, administration of a single dose of ICG-pHLIP by i.v. bolus injection was well tolerated in mice at a dose level of 12.3 mg/kg. Evidence of systemic exposure to ICG-pHLIP was observed in all animals and was quantifiable up to 16 hours post-dose.

Single i.v. toxicity with acute (24 hrs) and delayed (14 days) necropsy and TK in Beagle dogs;

7-days repeat i.v. toxicity in dog with acute (24h after last injection) and TK on days 1 and 7 in Beagle dogs

The objectives of this GLP study, performed at CRL, were to determine the potential toxicity of ICG-pHLIP, when given by single dose i.v. injection or once daily (i.v. injections) for 7 days in dogs, and to evaluate the potential reversibility of any findings following the single dose injection. In addition, toxicokinetic characteristics of ICG-pHLIP were examined.

The study design was as follows (40 Beagle dogs: 20 male and 20 female):

Group No.	Test Material	Dose Level (mg/kg/day)	Dose Volume (mL/kg)	Dose Concentration (mg/mL)	No. of Animals			
					Main Study		Recovery Study	
					Males	Females	Males	Females
1	Vehicle*	0	2.5	0	3	3	2	2
2	ICG-pHLIP	0.072**	2.5	0.029	3	3	-	-
3	ICG-pHLIP	1.08***	2.5	0.432	3	3	-	-
4	ICG-pHLIP	2.16****	2.5	0.864	3	3	2	2
5	Vehicle	0	2.5	0	2	2	-	-
6	ICG-pHLIP	2.16	2.5	0.864	2	2	-	-

* 5% (vol/vol) EtOH in PBS, pH 7.4

** based on dose formulation analytical results, animals from Group 2 received a dose level of 0.063 mg/kg, which is equivalent to 0.875x h.d.

*** equivalent to 15x h.d.

**** equivalent to 30x h.d.

The following parameters and end points were evaluated in the study: mortality, clinical observations, body weights, food consumption, ophthalmology and electrocardiology assessments, clinical pathology parameters (hematology, coagulation, clinical chemistry, and urinalysis), toxicokinetic parameters, gross necropsy findings, organ weights, and histopathological examinations.

There were no unscheduled deaths. There were no ICG-pHLIP-related clinical observations, and no ICG-pHLIP-related effects on the assessment of body weights, food consumption, ophthalmology and electrocardiology changes, hematology, coagulation, and urinalysis parameters, organ weights, or macroscopic and microscopic evaluations at any dose level tested following a single dose or a daily 7-day repeat dose administration.

Administration of ICG-pHLIP to dogs when given by repeated i.v. injection at 2.16 mg/kg/day for 7 days resulted in non-adverse clinical chemistry changes limited to minimal decreases in cholesterol in both males and females.

Systemic exposure to ICG pHLIP appeared to be independent of sex. Following a single i.v. bolus administration of ICG-pHLIP, mean C_0 and $AUC_{T_{last}}$ values increased with increasing dose in an approximately dose proportional manner from 1.08 to 2.16 mg/kg. Following daily i.v. bolus administration of 2.16 mg/kg ICG-pHLIP, mean C_0 and $AUC_{T_{last}}$ values were 38,400 ng/mL and 65,400 hr*ng/mL, respectively, on Day 1 and were 42,700 ng/mL and 72,300 hr*ng/mL, respectively, on Day 7. Systemic

exposure ($AUC_{T_{last}}$) to ICG-pHLIP did not appear to increase following repeated IV bolus administration of 2.16 mg/kg ICG-pHLIP.

In conclusion, ICG-pHLIP administered by a single i.v. bolus injection at 0.063, 1.08, or 2.16 mg/kg or once daily for 7 days at 2.16 mg/kg/day to dogs did not adversely affect overall health or condition of the animals, and had no impact on clinical pathology parameters, organ weights, macroscopic or microscopic pathology. Decreases in cholesterol levels were noted in ICG-pHLIP-treated animals at 2.16 mg/kg/day after repeated dosing but were considered non-adverse. Based on these results, the no-observed-adverse-effect level (NOAEL) was considered to be 2.16 mg/kg/day, with a Day 1 mean C_{max} of 40,300 ng/ml and AUC_{0-24} of 322,000 hr*ng/ml in males and females combined.

7-day repeat i.v. toxicity in mice with acute (24 hrs after last injection) and delayed (14 days) necropsy and TK on days 1 and 7 in B6D2F1 mice

The purpose of this GLP study performed at MSKCC was to assess the acute and delayed toxicity of a repeat administration of ICG-pHLIP in mice. The ICG-pHLIP was administered for 7 consecutive days.

The study design was as follows (82 B6D2F1 mice: 41 male and 41 female):

Group No.	Test Material	Dose Level (mg/kg/day)	No. mice/group	Sex	Sacrifice	Necropsy
Interim sacrifice on Days 8 and 9						
1	Vehicle*	0	10	Male	Day 8	Yes
2	ICG-pHLIP	13.6**	10	Female		

3	Vehicle	0	10	Male	Day 9	
4	ICG- pHLIP	13.6	10	Female		
Final sacrifice on Days 21 and 22						
5	Vehicle	0	5	Male	Day 21	Yes
6	ICG- pHLIP	13.6	5	Female		
7	Vehicle	0	5	Male	Day 22	
8	ICG- pHLIP	13.6	5	Female		
TK samples						
9	Vehicle	0	3	Male	Day 7	No
10	ICG- pHLIP	13.6	3	Female		
11	Vehicle	0	3	Male	Day 8	
12	ICG- pHLIP	13.6	3	Female		

* 5% (vol/vol) EtOH in PBS, pH 7.4

** equivalent to 27.6x h.d.

Throughout the study, body weights, clinical signs, clinical pathology (hematology and clinical chemistry), and histopathology were collected.

In conclusion, the repeat administration of ICG-pHLIP may be associated with germ cell degeneration in males with incidence and severity decreasing over time. No other signs of systemic or delayed toxicity were observed.

Follow up 7-days repeat i.v. toxicity in male mice with acute (24 hrs after last injection) and delayed (14 days) necropsy and TK on days 1 and 7 in B6D2F1 mice

The purpose of this GLP study performed at MSKCC was to assess the acute and delayed toxicity on the male reproductive system of mice of a repeat administration of ICG-pHLIP at different concentrations. The ICG-pHLIP was administered once/day for 7 consecutive days.

The study design was as follows (77 male B6D2F1 mice):

Group No.	Test Material	Dose Level (mg/kg/day)	No. of Male mice/group	Sacrifice	Necropsy
Interim sacrifice on Day 8					
1	Vehicle*	0	10	Day 8	Yes
2	ICG-pHLIP	4.92**	10		
3	ICG-pHLIP	7.38***	10		
4	ICG-pHLIP	12.3****	10		
Final sacrifice on Day 21					
5	Vehicle	0	5	Day 21	Yes
6	ICG-pHLIP	4.92	5		

7	ICG- pHLIP	7.38	5		
8	ICG- pHLIP	12.3	5		
TK samples					
9	Vehicle	0	3	Day 7	No
10	ICG- pHLIP	4.92	3		
11	ICG- pHLIP	7.38	3		
12	ICG- pHLIP	12.3	3		

* 5% (vol/vol) EtOH in PBS, pH 7.4

** equivalent to 10x h.d.

*** equivalent to 15x h.d.

**** equivalent to 25x h.d.

Throughout the study, body weights, clinical signs, and histopathology were collected.

In conclusion, the repeat administration of ICG-pHLIP at all dose levels is well tolerated, with no indication of germ cell degeneration or other toxicity to the male reproductive system.

Local tolerance/irritancy in New Zealand white rabbits

The objective of this GLP study performed at CRL was to compare the i.v., intra-arterial, perivascular and subcutaneous routes for potential irritation following a single injection of ICG-pHLIP in the rabbits.

The study design was as follows (18 male New Zealand white rabbits):

Group No.	Test Material	Targeted Dose Level (mg/kg)	Dose per 3kg Rabbit (mg)	Dose Volume (mL/kg)	Dose Conc. (mg/mL)	Total injected Dose Based on 3kg Rabbit (mg)	No. of Males
				i.v. right ear vein			
1	Vehicle*	0	0	3	0	0	3
2	ICG-pHLIP	0.124**	0.372	3	0.041	0.372	3
3	ICG-pHLIP	1.86***	5.58	3	0.62	5.58	3
				i.a. left ear artery/ Subc.lumbar			

Group No.	Test Material	Targeted Dose Level (mg/kg)	Dose per 3kg Rabbit (mg)	Dose Volume (mL/kg)	Dose Conc. (mg/mL)	Total injected Dose Based on 3kg Rabbit (mg)	No. of Males
				i.v. right ear vein			
4	Vehicle	0	0	1.5/1.5	0	0	3
5	ICG-pHLIP	0.124	0.372	1.5/1.5	0.041	0.379	3

Group No.	Test Material	Targeted Dose Level (mg/kg)	Dose per 3kg Rabbit (mg)	Dose Volume (mL/kg)		Dose Conc. (mg/mL)	Total injected Dose Based on 3kg Rabbit (mg)	No. of Males
				i.v.	right ear vein			
6	ICG-pHLIP	1.86	5.58	1.5/1.5		0.62	5.735	3

i.a. = intra-arterial; i.v. = intravenous; subc. = subcutaneous.

* 5% (vol/vol) EtOH in PBS, pH 7.4

** equivalent to 1x h.d.; based on dose formulation analytical results, animals from Group 2 and 5 received a dose level of 0.109 mg/kg for i.v., i.a. and/or subc. injection and 0.009 mg for perivenous space injection.

*** equivalent to 15x h.d.

The following parameters and end points were evaluated in this study: clinical signs, local irritation assessment, body weights (for dose calculation only), and histopathology of the injection sites. There were no clinical signs, local irritation or any microscopic changes associated with ICG-pHLIP during the study.

In conclusion, a single administration of ICG-pHLIP via i.v., intra-arterial, perivenous and subcutaneous injection was well tolerated in rabbits at total dose levels of 0.124 and 1.86 mg/kg. Administration did not result in any ICG-pHLIP-related changes.

A pharmacological safety assessment on the central nervous system of the Sprague Dawley rats

The objective of this GLP study performed at CRL was to evaluate the pharmacological effects of ICG-pHLIP on the central nervous system following a single i.v. bolus injection in rats.

The study design was as follows (32 male Sprague Dawley rats):

Group No.	Test Material	Dose Level (mg/kg)	Dose Volume (mL/kg)	Dose Concentration (mg/mL)	No. of Males
1	Vehicle*	0	5	0	8
2a	ICG-pHLIP	0.218**	5	0.0436	4
2b	ICG-pHLIP	0.248***	5	0.0496	4
3	ICG-pHLIP	3.72****	5	0.744	8
4	ICG-pHLIP	7.44*****	5	1.488	8

* 5% (vol/vol) EtOH in PBS, pH 7.4

** equivalent to 0.88x h.d.

*** equivalent to 1x h.d.

**** equivalent to 15x h.d.

***** equivalent to 30x h.d.

Functional observation battery (FOB) tests were performed once prior to dosing and again at 5 minutes, 3 and 24 hours post-dose and included the following assessments:

palpebral closure, eye prominence, pupil size, pupillary response, lacrimation, salivation, body tone, extensor thrust, pinna reflex, tactile reflex, overall animal reactivity, auricular startle, air righting reflex, body temperature (rectal). Additional evaluations consisted of mortality and clinical observations.

There were no ICG-pHLIP -related changes on any qualitative or quantitative FOB parameters at 0.218, 0.248, 3.72 and 7.44 mg/kg up to 24 hours post-dose.

In conclusion, a single i.v. bolus administration of ICG-pHLIP at dose levels of 0.218, 0.248, 3.72 and 7.44 mg/kg to rats had no effect on the central nervous system up to 24 hours post-dose.

A cardiovascular telemetry study in unrestrained conscious non-naïve Beagle dogs

The objective of this GLP study performed at CRL was to evaluate the potential cardiovascular effects of ICG-pHLIP in instrumented dogs when administered by i.v. bolus injection using a Latin square design.

Each of the four male dogs received a dose of Reference Item (5 % Ethanol in Phosphate buffered saline (PBS), pH of 7.4 ± 0.2) and three dose levels of ICG-pHLIP (0.072, 0.36, and 1.44 mg/kg), with a 7-day washout period between each dose. The dose was administered by i.v. bolus injection at a dose volume of 2.5 mL/kg.

The study design was as follows (16 male Beagle dogs):

Dosing Schedule (mg/kg)				
Animal No.	Dose 1	Dose 2	Dose 3	Dose 4
1	0	0.072	1.44	0.36
2	0.072*	0.36	0	1.44
3	0.36**	1.44	0.072	0

4	1.44***	0	0.36	0.072
Dose Level (mg/kg)	Concentration (mg/mL)	Dose Volume (mL/kg)	No. of Males	
0	0	2.5	4	
0.072	0.029	2.5	4	
0.36	0.144	2.5	4	
1.44	0.576	2.5	4	

* equivalent to 1x h.d.

** equivalent to 5x h.d.

*** equivalent to 20x h.d.

The following cardiovascular parameters were evaluated for all animals from 2 hours prior and up to 24 hours post each dose: systemic blood pressures (systolic, diastolic, mean arterial, and pulse pressure), heart rate, body temperature, and electrocardiographic duration/intervals (PR, QRS, QT, and QTc). Qualitative evaluation of the electrocardiographic waveforms was performed twice prior to each dose (at least 30 minutes apart) and at 5, 15, and 30 minutes, 1, 2, 3, 4, 6, 12, and 24 hours post-dose. Additional evaluations consisted of mortality and clinical observations. There were no mortalities or ICG-pHLIP-related clinical signs throughout the course of the study.

In conclusion, a single i.v. bolus injection of ICG-pHLIP at 0.072, 0.36, and 1.44 mg/kg to male dogs resulted in no effect on systemic blood pressures, heart rate, body temperature, electrocardiographic intervals (PR, QRS, QT or heart rate corrected QT [QTc]), or qualitative ECG parameters up to 24 hours post-dose.

Micronucleus test in Sprague Dawley rats

The objective of this GLP study performed at CRL was to determine the potential genotoxicity of ICG-pHLIP when given by i.v. bolus injection to rats using the peripheral blood micronucleus test.

In order to determine the maximum tolerated dose, a dose-range finding test was performed prior to the main test, where male and female rats (3 animals/sex) were administered a single dose of ICG-pHLIP by i.v. injection. The doses evaluated were 14 mg/kg and 25 mg/kg using 5% EtOH in PBS, pH 7.4 as the vehicle. Animals were observed for signs of toxicity and/or mortality. As no adverse clinical signs were noted during the dose-range finding test, the maximum practical dose of 25 mg/kg was set as the high dose to be evaluated in the main test using a single sex (males).

The main phase study design was as follows (37 rats: 31 males and 6 females):

Group No.	Test Material	Dose Level (mg/kg)	Dose Volume (mL/kg)	Dose Concentration (mg/mL)	No. of Animals	
					Male	Female
1	ICG-pHLIP	14***	10	1.4	3	3
2	ICG-pHLIP	25****	10	2.5	3	3
3	NP*****	-	10	0	5	-
4	ICG-pHLIP	6.25*	10	0.625	5	-
5	ICG-pHLIP	12.5**	10	1.25	5	-
6	ICG-pHLIP	25	10	2.5	5	-
7	CP*****	10	10	1	5	-

* equivalent to 25x h.d.

** equivalent to 50x h.d.

*** equivalent to 56x h.d.

**** equivalent to 100x h.d. – the maximum practical dose of ICG-pHLIP

***** NC is the negative control, 5% EtOH in PBS, pH 7.4.

***** PC is the positive control, cyclophosphamide monohydrate. Animals were dosed twice with CP by oral gavage with an interval of 24 hours (\pm 15 minutes).

Analysis of ICG-pHLIP dosing formulations conducted during the study confirmed that all formulations were acceptable for use.

No mortalities occurred during the main test and no ICG-pHLIP-related adverse clinical signs were observed. Additionally, no ICG-pHLIP-related body weight loss or depression in body weight gains were observed.

Blood was collected for micronuclei evaluation at 45 hours post-dose (Groups 3 to 7), and 69 hours post-dose (Groups 3 and 7). The proportion of immature erythrocytes among total erythrocytes in the peripheral blood (%RETs) and the percentage of micronucleated reticulocytes (%MN-RETs) in the NC group were within the laboratory historical negative control range. A clear, unequivocal and statistically significant increase in micronuclei was observed in the PC group. The results from both NC and PC groups confirmed the validity of the assay.

No substantial reduction (*i.e.* less than 50% the value of the concurrent NC) in the %RETs was observed for any of the ICG-pHLIP dosed groups, indicating that no substantial cytotoxicity was observed. Animals dosed with ICG-pHLIP did not show any statistically significant increases in the %MN-RETs when compared to the concurrent NC group. Therefore, ICG-pHLIP did not induce cytogenetic damage in peripheral blood immature erythrocytes in this micronucleus test, when administered once, by i.v. injection to male rats, up to the maximum practical dose of 25 mg/kg.

In conclusion, ICG-pHLIP showed no evidence of genotoxic activity in this *in vivo* study, when tested in accordance with regulatory guidelines.

In vitro bacterial reverse mutation test

The objective of this study performed at CRL was to determine the potential genotoxicity of ICG-pHLIP using the bacterial reverse mutation test.

The experimental design was as follows:

Dose No.	Formulation Conc. ($\mu\text{g/mL}$)	Dose Volume (μL)	Final Conc. ($\mu\text{g/plate}$)	No. of Replicates		No. of Strains
				0S9	+S9	
Negative Control*	-	100	-	3	3	5
1/ ICG-pHLIP	500	3.16	1.58	3	3	5
1/ ICG-pHLIP	500	10	5.0	3	3	5
1/ ICG-pHLIP	500	31.6	15.8	3	3	5
1/ ICG-pHLIP	500	100	50	3	3	5
2/ ICG-pHLIP	1581	100	158	3	3	5
3/ ICG-pHLIP	5000	100	500	3	3	5
4/ ICG-pHLIP	15811	100	1581	3	3	5
5/ ICG-pHLIP	50000	100	5000**	3	3	5
Positive controls	***	100	***	3	3	5

* vehicle, dimethyl sulfoxide (DMSO), was used as a negative control

** the OECD/ICH S2(R1) standard limit dose (usually 5000 $\mu\text{g/plate}$).

*** dose depended on the test strain, the positive controls and methodology used.

Salmonella typhimurium strains (TA1535, TA1537, TA98, TA100 and TA102) were treated with ICG-pHLIP at a range of concentrations up to 5000 $\mu\text{g/plate}$ (the standard limit dose for this assay), in the presence and absence of a supplemented rat liver

fraction (S9 mix), using the plate incorporation version of the bacterial reverse mutation test.

Bacteria were incubated with standard positive controls, and the response of the various bacterial strains to these agents confirmed the sensitivity of the test system and the activity of the S9 mix.

Incomplete, or absent, background lawns of non-revertant bacteria, or substantial reductions in revertant colony counts, were not obtained following exposure to ICG-pHLIP, indicating that ICG-pHLIP was non-toxic to the bacteria at the levels tested. No precipitation was observed in the assay.

No substantial increases in revertant colony numbers were obtained with any of the tester strains, following exposure to ICG-pHLIP at any dose level, in either the presence or absence of S9 mix. Therefore, ICG-PHLIP was considered to be negative for the induction of mutagenicity in this *in vitro* assay.

In conclusion, ICG-pHLIP did not show any evidence of genotoxic activity in this *in vitro* mutagenicity assay when tested in accordance with regulatory guidelines.

In vitro micronucleus test

The objective of this study performed at CRL was to determine the potential genotoxicity of ICG-pHLIP using an *in vitro* mammalian cell micronucleus test in human peripheral blood lymphocytes.

The experimental design was as follows:

Dose No.	Formulation Conc. ($\mu\text{g/mL}$)	Dose Volume ($\mu\text{L/culture}$)	Final Conc. ($\mu\text{g/mL}$)	No. of Cultures		
				4 Hours (0S9)	4 Hours (+S9)	24 Hours (0S9)
Negative Control*	-	50	-	2	2	2
1/ ICG-pHLIP	500	10	1.00	2	2	2
1/ ICG-pHLIP	500	20	2.00	2	2	2
1/ ICG-pHLIP	500	40	4.00	2	2	2
2/ ICG-pHLIP	800	50	8.00	2	2	2
3/ ICG-pHLIP	1600	50	16.0	2	2	2
4/ ICG-pHLIP	3200	50	32.0	2	2	2
5/ ICG-pHLIP	6400	50	64.0	2	2	2
6/ ICG-pHLIP	12800	50	128	2	2	2
7/ ICG-pHLIP	25600	50	256	2	2	2
8/ ICG-pHLIP	50000	50	500**	2	2	2
Colcemid	10	80	0.16	2	-	-
	10	90	0.18	2	-	-
	10	100	0.20	2	-	-
Nocodazole	20	50	0.20	2	-	-
	25	50	0.25	2	-	-
	30	50	0.30	2	-	-
Cyclophosphamide	1000	50	10	-	2	-
	1500	50	15	-	2	-
Mitomycin C	10	50	0.10	-	-	2

Dose No.	Formulation Conc. (µg/mL)	Dose Volume (µL/culture)	Final Conc. (µg/mL)	No. of Cultures		
				4 Hours (0S9)	4 Hours (+S9)	24 Hours (0S9)
	20	50	0.20	-	-	2

* vehicle, dimethyl sulfoxide (DMSO), was used as a negative control

** where the high level = 0.5 mg/mL.

Human peripheral blood lymphocytes were treated with ICG-pHLIP at levels up to the standard limit of 0.5 mg/mL. The high dose for micronucleus assessment was 0.5 mg/mL as no ICG-pHLIP-related cytotoxicity or precipitation was observed in the assay. The Negative Control results were within the laboratory negative historical control range. Lymphocytes were also incubated with standard Positive Controls, which caused statistically significant increases in the proportion of cells with micronuclei, confirming the sensitivity of the test system and the activity of the S9 mix. All criteria for a valid assay were therefore met.

Cultures treated with ICG-pHLIP did not show any statistically significant increases in the incidence of micronucleated binucleate cells. All results were within the distribution of the laboratory historical negative control data. Therefore, ICG-pHLIP was considered to be negative for the induction of micronuclei in this *in vitro* assay.

In conclusion, ICG-pHLIP did not show any evidence of genotoxic activity in the *in vitro* micronucleus test in human peripheral blood lymphocytes, when tested in accordance with regulatory guidelines.

Animal Imaging Studies

All imaging studies on mice were conducted at University of Rhode Island according to the approved animal protocol AN04-12-011 in compliance with the principles and

procedures outlined by the National Institutes of Health for the care and use of animals. All imaging studies in pigs were conducted at the Porcine Laboratory, Sutter Institute for Medical Research and approved animal protocol STE.10.19 (Stryker Endoscopy Imaging and Instrumentation Studies).

Imaging of Blood Vessels in Mice

ICG-maleimide was conjugated with Cys to form ICG-Cys for use as a control. Single tail vein administrations of 2.5 nmol of ICG-Cys or ICG-pHLIP in sterile PBS or PBS with 5% DMSO or 5% Ethanol (vol:vol) (volume of the injection was 100 μ l) were given to athymic female nude mice (strain Hsd Athymic Nude-Foxn1nu) ranging in age from 5 to 6 weeks (obtained from Envigo RMS Inc). Mice were under gas anesthesia, and imaging of mouse leg and ear was performed immediately and at different time points (from 5 min till 120 min) after administration of ICG-Cys or ICG-pHLIP using the Stryker 1558 AIM clinical imaging system with L10 AIM Light Source, 1588 AIM Camera and a 10 mm scope and a Novadaq imaging system. Five animals per construct were used in the study.

Imaging of Blood Vessels in Pigs

Pigs (50 kg) received ICG-pHLIP dissolved in PBS or PBS containing 5% Ethanol. Three doses of pHLIP-ICG were administered (dose level 1 is 0.052 mg/kg of ICG-pHLIP, dose level 2 is an additional administration of 0.12 mg/kg of ICG-pHLIP and dose level 3 is an additional administration of 0.24 mg/kg of ICG-pHLIP). Each dose was injected intravenously in one bolus followed by a saline flush. Endoscopical and exoscopical imaging was performed at the same time and up to 2 hrs after ICG-pHLIP administration. Imaging endoscopically was carried out using the Stryker 1688 system with the L11 light source (808 nm excitation) and adjustable gain. A 10 mm 30 degree

Stryker AIM laparoscope was used for imaging of animal internal cavities. Open field imaging was performed using the Stryker SPY-PHI system (805 nm excitation) and fixed gain. Images and video were recorded on a Stryker Connected OR Hub device. The 1688 system has three infrared imaging modes: Overlay, Contrast, and ENV. Overlay mode captures an NIR frame and a white light frame and combines the two to allow surgeons to have the best fluorescence reference (green) while still operating. Contrast mode provides the highest signal to noise image for the fluorescence signal and does not contain any data from the white light frame. ENV mode contains the white light frame data in a black/white mode and overlays the fluorescence signal in green to provide a hybrid mode that allows a higher signal to noise ratio view of the fluorescence image while still retaining enough of a view of the surrounding tissue to allow the surgeon to continue to operate. The SPY-PHI system has three infrared imaging modes: Overlay, Contrast, and CSF (color-segmented fluorescence). CSF mode is a type of heat map where the fluorescence signal is mapped to color according to intensity. Contrast mode is noticeably more sensitive to viewers than Overlay or CSF mode for weaker signals.

Biodistribution and Kinetics

BALB/cAcNHsd mice ranging in age from 5 to 6 weeks obtained from Envigo RMS, Inc. were used in the study. Mouse mammary 4T1 cancer cells were subcutaneously implanted in the right flank (8×10^5 cells/0.1 mL/flank) of adult female or male mice. The triple negative 4T1 tumor model closely mimics stage IV of human breast cancer. When tumors reached 5-6 mm in diameter, single tail vein injections of 0.5 mg/kg of ICG-pHLIP in sterile PBS, or PBS with 5% DMSO or 5% Ethanol (vol:vol) (volume of the injection was 100 μ l) were performed. Animals were euthanized at time points: 5 min, 1, 2, 4, 6, 16, 26 and 48 hrs after ICG-pHLIP administration. Several animals

were used for each time point plus seven control animals (no ICG-pHLIP administration). Tumor, muscles, skin, heart, lungs, liver, spleen, kidneys, brain, pancreas, bone, stomach, small and large intestines were collected, imaged immediately after necropsy, weighed, and fast frozen in liquid nitrogen. The *ex vivo* imaging of organs was performed using Stryker 1588 AIM endoscopic system with L10 AIM Light Source, 1588 AIM Camera using a 10 mm scope. The lens was spaced 4.3 cm away from the surface of the organs within an enclosed (light protected) area. The NIR fluorescence imaging of each organ was performed at three different laser intensity settings. The digital images of organs were processed using aour program written in Python to determine the average level of intensity recorded in the green channel. Since organs were imaged in the dark on black mats, the background signal was determined by introducing an intensity threshold. All the pixels with intensity from the green channel above the set threshold were counted and the average green intensity per pixel was calculated. For organs for which the highest laser intensity produced a saturated image, the medium laser intensity images were analyzed, then converted to a theoretical comparison using experimentally found conversion curves. The fluorescence signals in organs and tissue were also measured in the tissue/organ homogenates and compared with the signals from the control tissue/organ homogenates (collected from control mice) mixed with known amounts of ICG-pHLIP. About 100 mg of tissue were homogenized with 2.5x (about 250 μ L) volumes of DMSO using BioMasher II disposable homogenizers (DiagnoCine, LLC). 30 μ l of homogenate was placed into 384 well plate and imaged using an Odyssey IR scanner (Li-Cor Biosciences). Tissue homogenates of control mice mixed with known concentrations of ICG-pHLIP were used to establish the calibration curve.

Imaging Tumors in Different Tumor Models

Targeting of murine and human tumors was shown in 8 different tumor models in athymic female nude mice (strain Hsd Athymic Nude-Foxn1nu) ranging in age from 5 to 6 weeks (obtained from Envigo RMS, Inc). The following tumors were established by subcutaneous injection of 1×10^6 cells/0.1 ml/flank in flanks of athymic nude mice: HeLa (humans cervical adenocarcinoma), M4A4 (human epithelial carcinoma), 4T1 (murine breast tumor), A549 (human lung carcinoma), LLC (murine Lewis Lung carcinoma), UM-UC3 (human urinary bladder cancer), and 4×10^6 cells/0.1 ml/flank of LNCaP tumor (human prostate cancer). Human MDA-MB-231 (breast adenocarcinoma) tumors were established by injections of 1×10^6 cells/0.05 ml in the mammary fat pad. Tumors reached different sizes (from very small (1-2 mm in diameter) to large (8-12 mm in diameter) and 100 μ l of tail vein injections of 0.5 mg/kg of ICG-pHLIP in sterile PBS or PBS containing either 5% of DMSO or 5% of Ethanol were performed. Imaging was carried at 24 hours after ICG-pHLIP administration. White light and NIR whole-body imaging were performed while the animal was under gas (isoflurane) anesthesia using a Stryker 1558 AIM clinical imaging system with L10 AIM Light Source, 1588 AIM Camera and a 10 mm scope. Next, the skin was removed from the tumor side and whole-body imaging of live animals was performed with the skin removed from the tumor side. Finally, surgery was carried out under fluorescence-guidance to remove tumor and image tumor bed using Stryker SPY-PHI handheld clinical imaging system.

Histopathology

Tumors with surrounding muscle were frozen in tissue-tek OCT compound using liquid nitrogen and stored at -80°C until sectioned using a cryostat at -25°C (Thermo

Scientific HM525 NX) at a 5 μm thickness. The tumor slides were fixed in 4% formaldehyde and stained with hematoxylin and eosin (H&E) (Thermo Fisher Scientific and Poly Scientific R & D Corp). Some sections were covered with a drop of mounting medium (Permount[®], Fisher Scientific) and then a cover slide was placed over the medium. Stained and non-stained sections were imaged using an Odyssey IR scanner (Li-Cor Biosciences), Styer imaging system, and inverted microscope "Invitrogen EVOS FL Auto 2" using 4x and 10x objectives. Tiled HE images were made using "Invitrogen EVOS FL Auto 2.0 Imaging System" software.

TABLES

Table S1. Qualification of GLP ICG-pHLIP verification batch #1912127 manufactured by CordenPharma, GmbH.

Characteristic	Test Method	Specification	Results
Appearance	Visual	Green powder	conforms
Identity	LC-MS	1382.9 [M+3H] ³⁺ /3 ± 1 amu	conforms
Identity	HPLC	Elution peak with 5% deviation	conforms
Purity, (<i>p</i>)	HPLC	>98.5%	98.6%
Impurities	HPLC	Total Imp.: NMT 1.5%	1.4%
Acetic Acid Content	IC	≤ 5%	4.4%
TFA Content	IC	Determine and report	0.01%
Photo-Assay	NIR	$0.8 \cdot p \cdot k \leq OD \leq 1.11 \cdot p \cdot k$	0.85
Residual solvents	GC	Determine and report	DMF < 100 ppm ACN < 50 ppm i-hexane < 50 ppm MTBE < 50 ppm DCM < 50 ppm
Water content	KF	Determine and report	1.55%
Peptide Content (<i>k</i>)	CHN	Determine and report	N (total): 12.6%

			Peptide content: 91%
Cation Content, NH₄⁺	IC	Determine and report	0.79% (correlates to 0.6% N)
Cation Content, Na⁺	IC	Determine and report	<0.01%
Peptide Content/Amino Acid Composition	AAA	Conforms to theory	87.6%
Peptide Sequence	MS/MS	Conforms to theory	Conforms to theory, beside AA 1 and 2

LC-MS - liquid chromatography - mass spectrometry; HPLC - high performance liquid chromatography; IC – ion chromatography; GC – gas chromatography; KF - Karl-Fischer titration; CHN – carbon, hydrogen, nitrogen element analysis; AAA – amino acid analysis with St.D. <10%; MS/MS – tandem mass spectrometry.

Table S2. The bound and unbound fractions of ICG-pHLIP treated with whole blood or plasma.

	Whole-blood bound fraction	Plasma bound fraction	Plasma unbound fraction
Human	>99.9%	>99.9%	<0.1%
Mouse	>99.9%	95.3%	4.8%
Rat	>99.9%	96.6%	2.3%
Dog	>99.9%	98.8%	1.2%
Minipig	>99.9%	99.3%	0.7%
Cyno	>99.9%	99.6%	0.4%

Table S3. Concentration of ICG-pHLIP ($\mu\text{g/mL}$) in blood of mice and dogs at different time points after single i.v. administration of 12.3 mg/kg of ICG-pHLIP to mice and 0.064 mg/kg of ICG-pHLIP to dogs.

Time post-dose, hours	Concentration of ICC-pHLIP in mice blood, $\mu\text{g/mL}$	Concentration of ICG-pHLIP in dog blood, $\mu\text{g/mL}$
0.08	1.347 ± 0.092	275.4 ± 7.5
0.25	1.230 ± 0.082	251.5 ± 13.9
0.5	1.123 ± 0.089	239.8 ± 6.3
1	0.882 ± 0.099	217.0 ± 8.9
2	0.749 ± 0.065	144.0 ± 13.1
4	0.432 ± 0.056	102.6 ± 4.8
6	0.319 ± 0.041	68.7 ± 1.3
8	0.207 ± 0.032	58.8 ± 14.0
12	0.118 ± 0.008	-
16	-	14.6 ± 2.6

Table S4. Fluorescence intensity (a.u.) obtained by *ex vivo* imaging of organs collected at different time points after i.v. administration of ICG-pHLIP into female Balb/C mice bearing 4T1 tumors in right flank.

Organ/Time	5 min	1 hr	2 hrs	4 hrs	6 hrs	16 hrs	26 hrs	48 hrs
Tumor	46.3	92.0	119.7	205.3	193.8	208.2	173.3	135.5
	37.2	117.6	145.3	219.5	169.3	226.8	208.2	167.0
	32.4	73.8	151.9	191.8	250.5	233.9	182.1	152.0
	33.4	61.1	121.8	206.4	172.1	214.5	174.8	
	31.7	157.9	131.1	233.0	207.3	230.6	174.4	
				111.6			215.3	
				166.6			197.1	
			174.4			136.3		
Liver	380.8	541.2	560.0	532.7	517.1	382.1	213.8	154.4
	393.6	558.6	568.2	569.4	560.7	386.3	196.9	151.2
	469.0	519.7	555.7	541.0	489.1	455.1	217.1	143.2
	450.4	520.5	523.6	539.5	483.9	368.5	214.9	
	405.4	525.1	505.3	517.6	584.9	410.3	223.0	
				540.6			217.6	
				553.0			209.6	
			593.2			215.9		
Kidneys	145.9	202.1	175.6	191.7	169.6	154.1	121.4	52.0
	180.2	202.8	161.0	188.5	169.3	175.2	100.2	71.4
	165.6	179.8	152.4	175.7	173.3	183.1	108.4	73.9
	195.7	199.0	154.4	183.6	180.9	160.3	115.2	
	171.2	184.9	136.8	188.0	176.9	180.4	113.8	
				178.3			117.7	
				171.0			117.0	
			172.9			118.7		
Heart	174.5	188.4	164.5	191.7	153.6	128.2	67.8	23.3

	213.0	194.5	154.9	191.6	166.7	115.2	50.1	23.3
	211.8	170.2	183.9	174.5	155.5	146.4	63.4	23.0
	191.5	155.5	176.2	182.8	166.5	112.3	61.5	
	199.6	189.6	158.3	187.5	173.0	143.6	63.6	
				179.0			42.8	
				181.5			52.1	
				175.9			57.9	
Lungs	214.0	194.4	176.4	187.1	150.6	132.0	54.4	31.5
	218.3	202.2	163.5	209.3	165.3	115.2	54.5	35.8
	220.4	192.7	172.4	163.7	141.9	169.5	81.1	35.2
	215.4	185.8	180.7	196.1	180.4	133.2	53.2	
	214.8	198.5	191.7	179.0	145.7	156.4	77.6	
				171.3			76.0	
				159.0			69.3	
			161.4			57.9		
Brain	137.0	126.7	95.4	73.2	50.6	36.1	0	0
	153.9	151.5	79.9	78.5	48.7	37.9	0	0
	196.2	138.1	96.9	60.0	47.9	35.6	0	0
	172.2	136.8	53.8	76.5	55.2	33.7	0	
	175.6	135.4	84.8	81.0	74.3	33.3	0	
				78.8			0	
				84.6			0	
			92.5			0		
Spleen	146.1	158.7	134.3	158.3	133.6	102.2	39.9	21.9
	154.8	162.3	144.2	167.2	160.9	101.4	40.6	22.0
	168.9	161.1	135.4	143.8	152.7	150.1	50.7	21.9
	147.9	151.4	144.6	140.0	134.0	92.5	50.8	
	155.5	155.5	126.2	145.2	159.3	135.3	58.1	
				144.4			60.1	
				138.4			65.4	
			155.3			43.6		
Pancreas	169.1	163.4	121.6	101.6	70.7	72.6	46.5	0

	176.4	-	96.2	80.2	62.0	49.6	38.4	0
	186.6	140.5	41.3	96.3	87.1	121.2	34.2	0
	129.0	119.1	111.3	77.4	96.3	49.5	35.4	
	104.9	107.9	74.8	104.7	95.1	58.6	0	
				93.5			0	
				89.1			42.6	
				81.9			28.3	
Bone	73.8	67.3	40.3	90.1	58.7	76.7	43.1	44.3
	73.1	92.8	62.5	35.6	73.6	73.4	45.4	55.2
	88.8	77.0	48.3	55.3	61.2	58.3	42.3	40.5
	73.4	75.5	96.1	57.5	49.2	64.5	50.2	
	87.8	57.5	40.4	76.9	90.8	58.2	32.8	
				80.1			68.2	
				31.2			60.2	
				78.8			63.8	
Stomach	72.8	125.1	49.9	98.5	126.8	103.5	42.2	25.6
	82.5	81.7	91.1	107.6	129.7	86.3	48.3	36.9
	104.2	71.8	79.9	109.5	141.6	161.0	71.0	30.7
	99.6	98.0	98.4	116.4	119.8	92.1	62.2	
	99.3	118.8	84.3	110.3	116.1	143.6	72.0	
				136.5			52.3	
				126.1			47.9	
				66.8			49.6	
Small intestine	62.2	78.3	64.3	83.5	40.4	77.6	34.3	0
	45.5	97.2	57.8	54.9	58.8	107.8	43.8	0
	38.4	68.8	31.5	42.1	44.2	78.6	35.8	22.7
	33.0	62.1	45.4	73.1	68.2	80.9	41.6	
	33.0	53.0	36.3	70.8	59.5	74.2	33.2	
				67.0			73.0	
				71.1			64.6	
				44.8			61.5	

Large intestine	42.4	49.1	0	0	32.3	37.1	0	0
	35.4	32.5	32.2	39.4	33.4	42.6	0	0
	30.0	33.3	0	0	30.0	37.8	0	0
	47.8	27.0	0	0	39.8	36.6	0	
	29.8	0	0	0	0	45.2	0	
					44.0		24.9	
Skin	40.6	32.0	40.9	66.9	34.5	91.1	0	37.7
	1.0	39.4	43.4	51.0	66.1	60.5	31.9	0
	38.0	54.1	0	38.5	56.3	82.5	0	0
	33.4	38.2	36.8	39.6	37.3	50.7	57.0	
	27.6	32.1	39.0	45.1	41.2	98.9	36.4	
				51.7			137.2	
Muscle	36.5	0	0	36.2	0	0	0	0
	1.0	40.8	0	0	0	0	0	0
	1.0	0	0	41.7	0	0	42.9	0
	38.6	0	0	0	0	0	0	
	35.9	0	0	53.0	0	0	0	
				27.2			64.9	
			25.5			0		
			0			0		

Table S5. Mean (and St. D.) of fluorescence intensity values presented in Table S4.

Organ/ Time	5 min	1 hr	2 hrs	4 hrs	6 hrs	16 hrs	26 hrs	48 hrs
Tumor	36.2± 6.0	100.5 ±38.5	133.9± 14.2	188.6 ±38.1	198.6 ±33.0	222.8 ±11.0	182.7 ±24.8	151.5 ±15.7
Liver	419.8 ±37.9	533.0 ±16.7	542.6± 26.8	548.4 ±23.5	527.1 ±44.4	400.5 ±34.1	213.6 ±7.7	149.6 ±5.8
Kidney s	171.7 ±18.4	193.7 ±10.6	156.0± 14.1	181.2 ±7.8	174.0 ±5.0	170.6 ±12.8	114.0 ±6.8	65.8± 12.0
Heart	198.1 ±15.9	179.6 ±16.4	167.6± 12.2	183.1 ±6.7	163.0 ±8.2	129.2 ±15.7	57.4± 8.4	23.2± 0.2
Lungs	216.6 ±2.7	194.7 ±6.2	177.0± 10.4	178.4 ±18.0	156.8 ±15.9	141.3 ±21.5	65.5± 11.7	34.1± 2.3
Brain	167.0 ±22.5	137.7 ±8.9	82.2±1 7.4	78.1± 9.4	55.3± 11.0	35.3± 1.8	0.0±0. 0	0.0±0. 0
Spleen	154.6 ±9.0	157.8 ±4.4	136.9± 7.7	149.1 ±10.1	148.1 ±13.4	116.3 ±25.0	51.1± 9.5	21.9± 0.0
Pancre as	153.2 ±34.7	132.7 ±24.5	89.0±3 2.0	90.6± 10.1	82.2± 15.3	70.3± 30.0	28.2± 18.2	0.0±0. 0
Bone	79.4± 8.1	74.0± 13.1	57.5±2 3.4	63.2± 21.8	66.7± 16.0	66.2± 8.5	50.8± 12.2	46.7± 7.6
Stomac h	91.7± 13.4	99.1± 23.0	80.7±1 8.6	108.9 ±20.7	126.8 ±9.9	117.3 ±33.1	55.7± 11.3	31.0± 5.7
S. Intest.	42.4± 12.2	71.9± 16.9	47.1±1 3.9	63.4± 14.6	54.2± 11.6	83.8± 13.6	48.5± 15.6	7.6±1 3.1
L. Intest.	37.1± 7.9	28.4± 17.9	6.4±14. 4	17.5± 19.6	27.1± 15.6	40.5± 4.0	6.6±1 2.2	0.0±0. 0
Skin	27.9± 16.4	39.1± 9.0	32.0±1 8.1	49.2± 10.1	47.1± 13.6	76.7± 20.4	39.5± 43.7	12.6± 21.8
Muscle	22.2± 20.3	8.2±1 8.2	0.0±0.0	22.9± 20.8	0.0±0. 0	0.0±0. 0	13.5± 25.6	0.0±0. 0

Figures

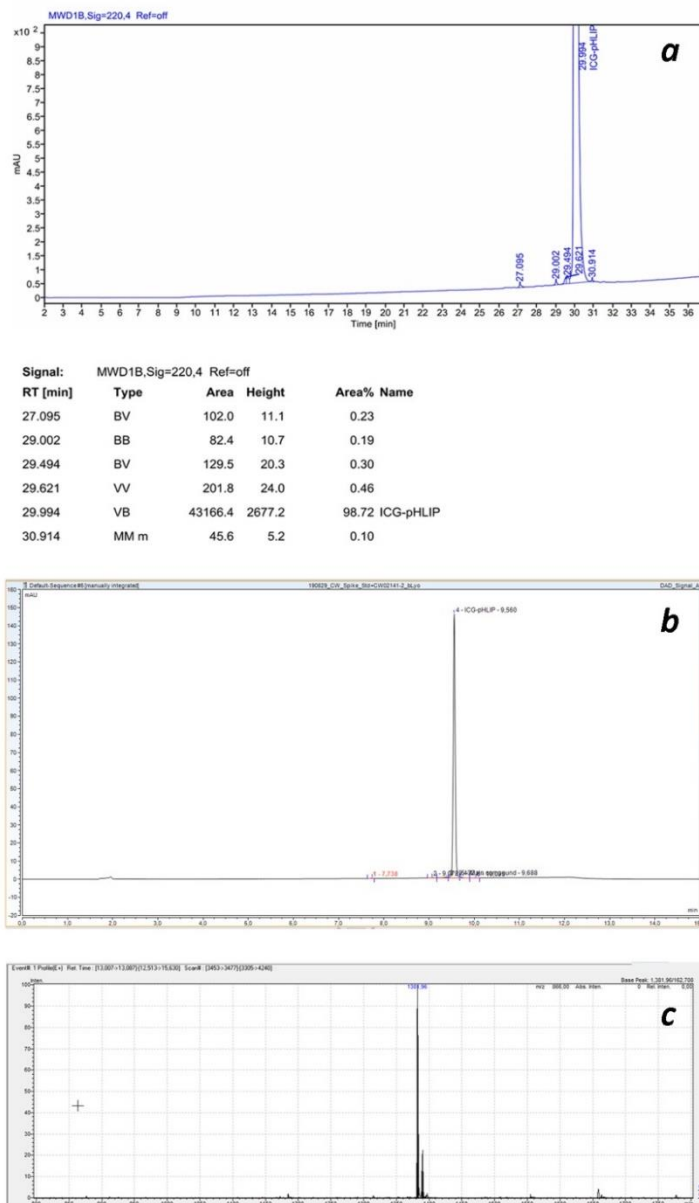


Figure S1. (a) HPLC chromatogram of ICG-pHLIP used in PoC and toxicology studies. (b) The spiking experiment: ICG-pHLIP synthesized by CordenPharma according to the optimized protocol was spiked with ICG-pHLIP shown on panel a in ratio of 1:1, dissolved in ACN/water/Tween20 in a ratio of 50:50:0.02 containing 5 mM tri potassium-EDTA and analyzed using the standard analytical method. The HPLC chromatogram provides a single signal, consistent with the compliance of both substances. (c) The mass spectrum of ICG-pHLIP synthesized by CordenPharma is shown.

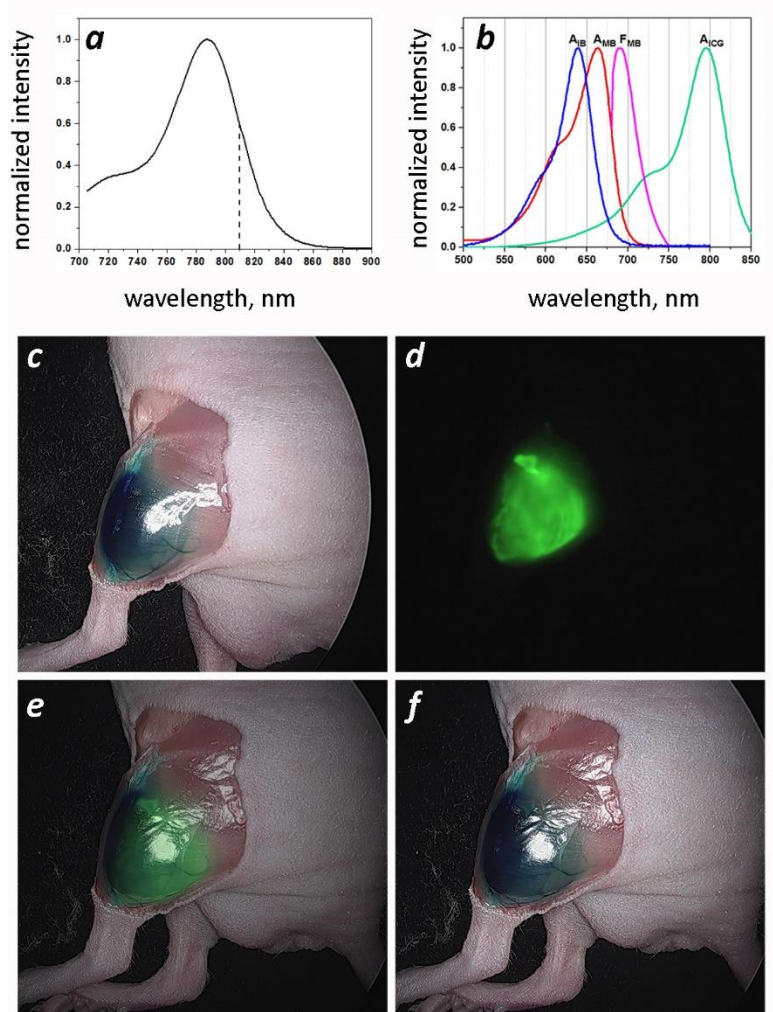


Figure S2. Normalized absorbance spectrum of ICG-pHLIP in methanol (*a*), absorbance and fluorescence spectra of Isosulfan Blue (IB) in water, Methylene Blue (MB) in PBS, and absorbance spectra of ICG-pHLIP (ICG) in DMSO (*b*). Color image of mouse received intra-tumoral injection of Isosulfan Blue (*c*). NIRF image of the same mouse followed by intra-tumoral injection of ICG-pHLIP (*d*). Overlay of color and NIRF ICG-pHLIP images (*e*) and color image of the same mouse after administration of both IB and ICG-pHLIP (*f*). The data clearly demonstrate that the administration of ICG-pHLIP does not obstruct IB or MB visualization.

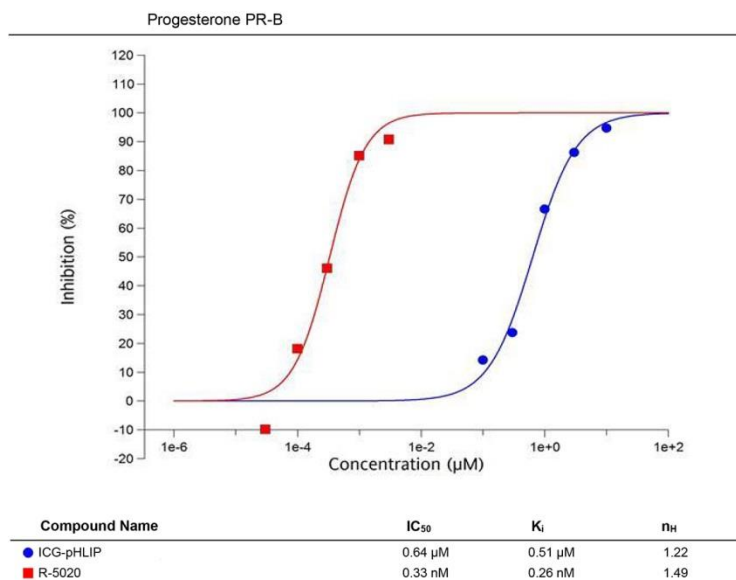


Figure S3. Inhibition response curves obtained in a radio ligand binding assay after treatment of progesterone B with increasing concentrations of ICG-pHLIP and R-5020 (a known progesterone B agonist) for 20 hrs. The experiments were performed by Eurofins Panlabs, Inc.

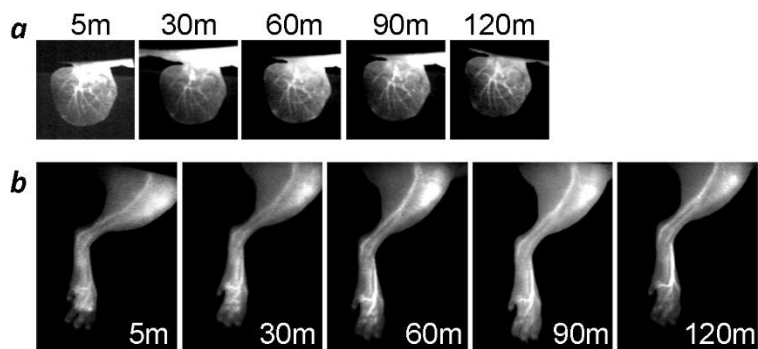


Figure S4. Fluorescence angiography with ICG-pHLIP. Mice under gas anesthesia received a single tail vein injection of 0.5 mg/kg of ICG-pHLIP followed by imaging within 2 hrs using a Novadaq imaging system. The signal was recorded from the mouse ear (*a*) and leg (*b*).

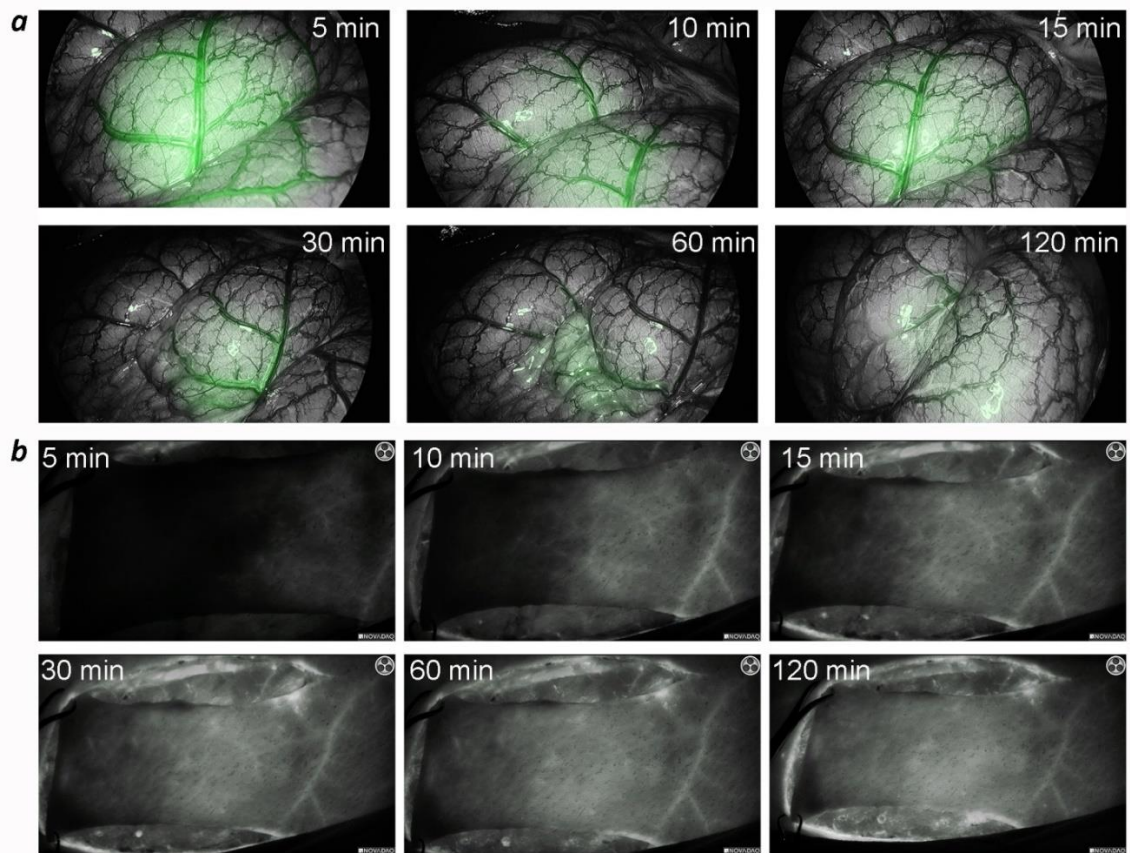


Figure S5. Imaging of blood vessels in pigs. NIR ICG-pHLIP fluorescent images of blood vessels at different time points after a single i.v. injection of ICG-pHLIP are shown. Imaging inside the pig body cavity was performed using a Stryker system for endoscopic/laparoscopic imaging (*a*). Imaging of a pedicle flap was performed using a Stryker for open field imaging (*b*).

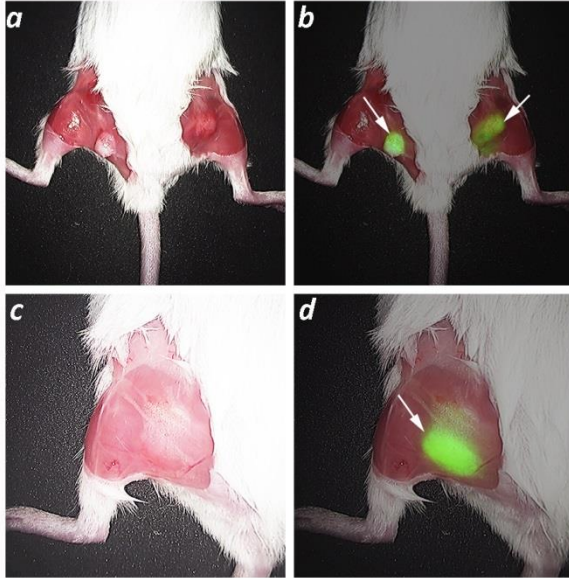


Figure S6. Photo image of Balb/C mouse bearing 4T1 tumors in both flanks (*a-b*) or in a single flank (*c-d*) with skin removed from the tumor site (*a, c*). Overlays of photo and NIR ICG-pHLIP fluorescent images are shown (*b, d*) (tumors are indicated by arrows). ICG-pHLIP was administered as a single i.v. injection (0.5 mg/kg), imaging was performed 24 hrs post-dose while animal was under gas anesthesia and was euthanized immediately after imaging.

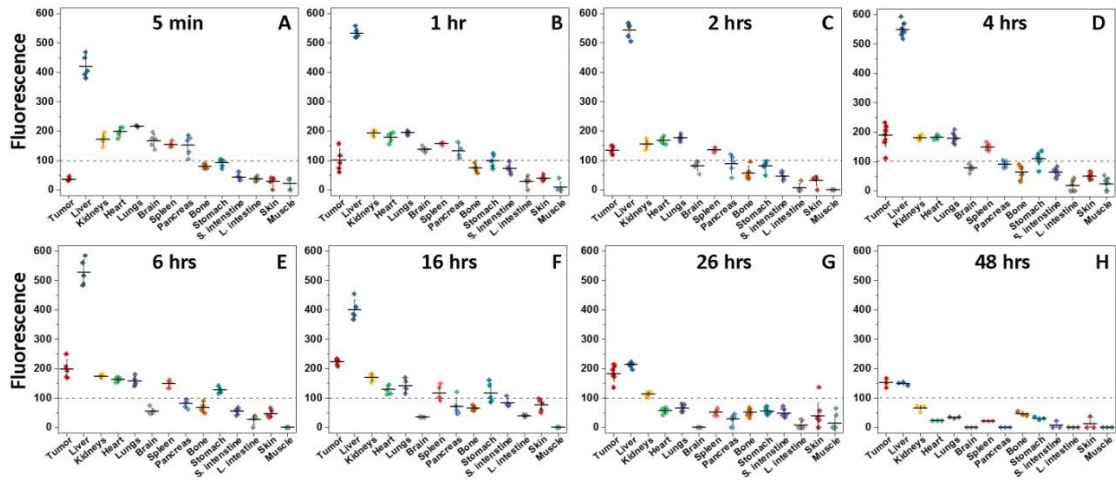


Figure S7. Tissue/organ mean surface fluorescence calculated from NIR ICG-pHLIP fluorescent images for each mouse (the representative images are shown on Figure 4 and numbers are given in Table S4) and the calculated mean values of fluorescence (numbers are presented in Table S5) are shown for different time points post-dose of ICG-pHLIP.

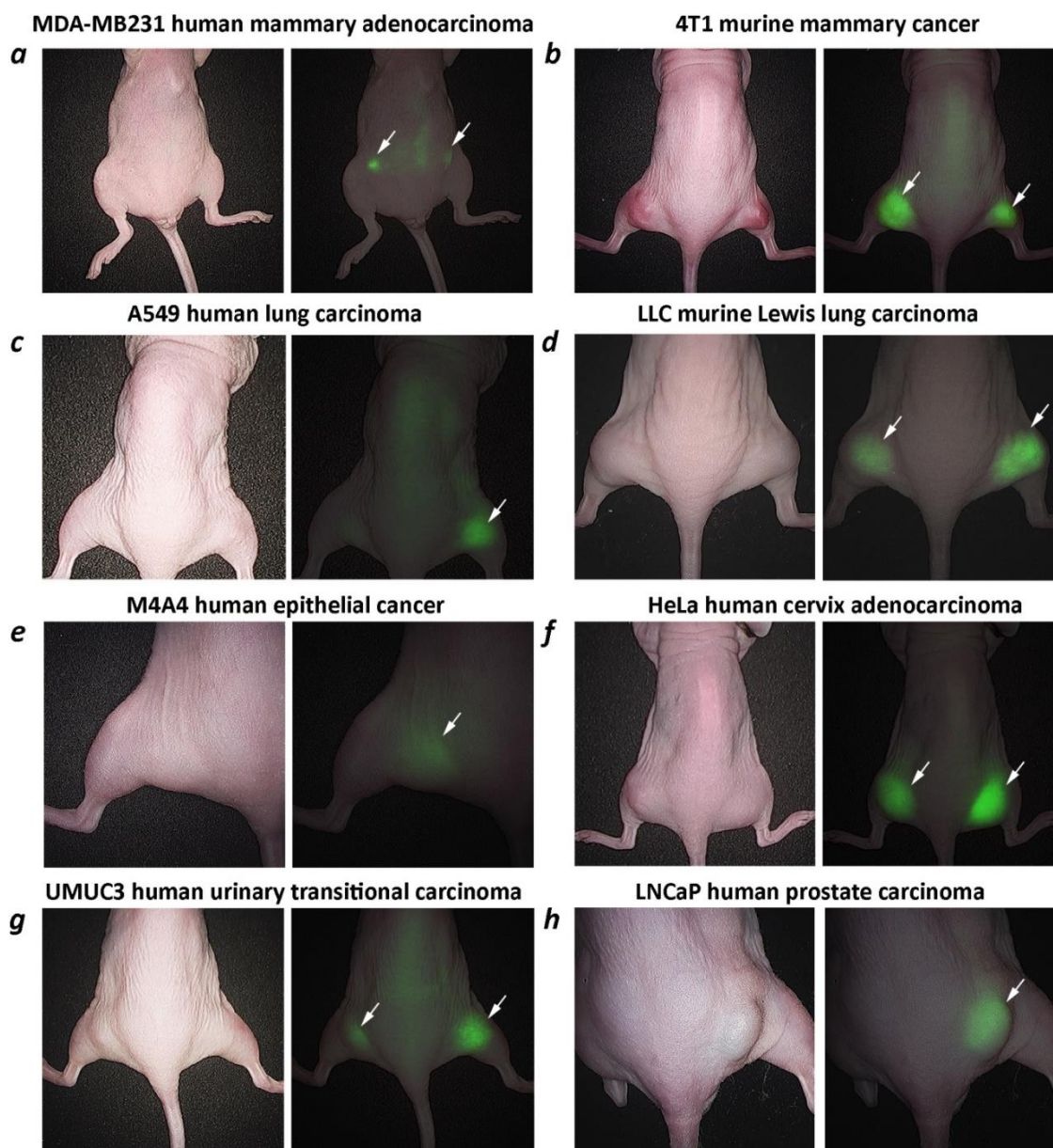


Figure S8. Photo images and overlay of photo and NIR ICG-pHLIP fluorescent images of athymic nude mice bearing human and murine tumors. ICG-pHLIP was administered as a single i.v. injection (0.5 mg/kg), imaging was performed 24 hrs post-dose, while the animal was under gas anesthesia. Tumors are indicated by arrows.

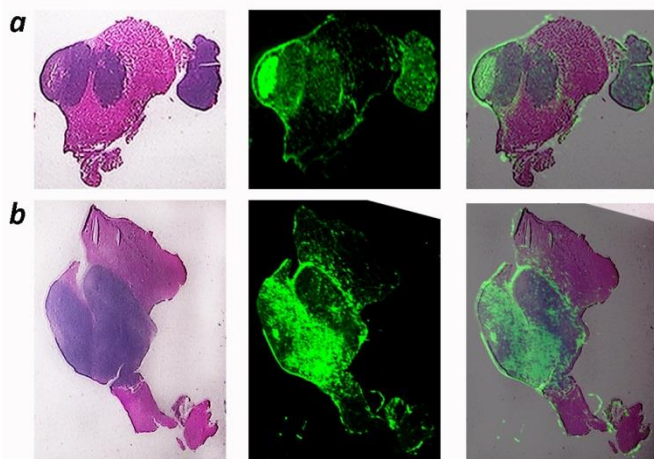


Figure S9. Each row contains an HE image, a NIR ICG-pHLIP fluorescent image, and an overlay of HE and NIR ICG-pHLIP images. UMUC3 human urinary transitional carcinoma (**a**) and 4T1 murine mammary cancer (**b**) tumors were grown in flanks of nude mice. ICG-pHLIP was administered as a single i.v. injection (0.5 mg/kg). Animals were euthanized 24 hrs post-dose, tumors were collected, frozen, and cryo-sectioned. Each second section was stained with HE. HE sections were imaged using a Stryker instrument and NIR imaging was performed using an Odyssey IR scanner. The correlation between tumor location (dark blue) and fluorescent signal is demonstrated.